Condensation of Adhesion Domains in Biological and Bio-Mimetic Membranes

Thesis submitted in partial fulfillment
of the requirements for the degree of
DOCTOR OF PHILOSOPHY

by

Nadiv Dharan

Submitted to the Senate of Ben-Gurion University of the Negev

July 24, 2017

Be'er-Sheva

Condensation of Adhesion Domains in Biological and Bio-Mimetic Membranes

Thesis submitted in partial fulfillment
of the requirements for the degree of
DOCTOR OF PHILOSOPHY

by

Nadiv Dharan

Submitted to the Senate of Ben-Gurion University of the Negev

Approved by the advisor: _____

Approved by the Dean of the Kreitman School of Advanced Graduate Studies: _____

July 24, 2017

Be'er-Sheva

This work was carried out under the supervision of Prof. Oded Farago

In the Department of Biomedical Engineering

Faculty of Engineering

Research-Student's Affidavit when Submitting the Doctoral Thesis for Judgment

I Nadiv Dharan, whose signature appears below, hereby declare that (Please mark the appropriate statements):

✓ I have written this Thesis by myself, except for the help and guidance offered by my Thesis Advisors.

✓ The scientific materials included in this Thesis are products of my own research, culled from the period during which I was a research student.

___ This Thesis incorporates research materials produced in cooperation with others, excluding the technical help commonly received during experimental work. Therefore, I am attaching another affidavit stating the contributions made by myself and the other participants in this research, which has been approved by them and submitted with their approval.

Date: July 24, 2017 Student's name: Nadiv Dharan Signature: Nadiv Dharan

Acknowledgments

First and foremost, I wish to sincerely thank my supervisor Prof. Oded Farago for the invaluable guidance and support over the past years, which enabled me to obtain a deeper appreciation for biophysical phenomena, greatly expanded my theoretical skills, and stimulated me to pursue scientific research.

I thank the Negev-Faran scholarship for providing the necessary financial support for this work.

I would like to thank my colleagues and friends Mr. Noam Weil and Dr. Yotam Yosef Avital for the stimulating discussions we had over the years and the help throughout this project.

I would like to expresses my utmost gratitude to my family for the great support they have provided over the years.

Finally, a special thanks to my beloved wife and best friend Bettina, who never stops expressing her unconditional love and full support, and has continuously encouraged me to follow my passions.

Abstract

Lipid bilayers are ubiquitous in biology, and constitute natural barriers separating the outer environment from the inner content of cells and intracellular organelles. Among numerous other proteins with diverse biological functions, the plasma membrane is equipped with adhesion proteins that bind the membrane to the extracellular matrix and/or neighboring cell membranes. Adhesion bonds often aggregate on the surface of the membrane and form macroscopically large adhesion domains containing hundreds to thousands of bonds, which provide greater mechanical stability to cells and also promotes signaling cues for various biological purposes. The formation of adhesion clusters is, thus, fundamental to life as it regulates numerous important biological processes, such as tissue formation, cell migration and intercellular communication. One important thermodynamic mechanism facilitating adhesion cluster formation is the membrane-mediated potential of mean force (PMF) between adhesion bonds, which originates from the membrane's thermal undulations and elastic curvature energy. The aggregation of adhesion bonds that bind a membrane to another surface enhances the membrane's thermal roughness and reduces its curvature energy; the membrane-mediated PMF is essentially the associated free energy gained. In this work, we employ statistical-mechanical methods, conduct molecular computer simulations, and use novel mean-field calculations to investigate the influence of membrane-mediated interactions on the condensation transition of adhesion bonds in supported biomimetic and biological membranes.

The entropic membrane-mediated mechanism for aggregation of adhesion bonds is investigated by conducting molecular simulations of a solvent-free coarse-grained model for supported lipid bilayers. Our simulation results corroborate the conclusions drawn from previous theoretical studies, and show that the fluctuation-induced PMF is too weak to promote condensation on its own; nevertheless, it greatly facilitates aggregation by partially compensating for the loss of mixing entropy, and effectively reducing the temperature by a factor of 2-3. The influence of thermal fluctuations on the condensation transition is further examined by simulating membranes exhibiting reduced or enhanced thermal undulations, by subjecting them to physical confinement or negative surface tension, respectively. Our results reveal that while the condensation transition is significantly shifted for confined membranes,

the impact of negative tension is negligible. Nevertheless, once adhesion domains form, a negative tension may result in strong membrane buckling and the formation of elongated adhesion domains.

In contrast to the long-range fluctuation-induced interactions, the curvature-induced PMF spans over a correlation length, ξ_γ, which for biological membranes is typically in the range of several tens of nanometers. Our investigation of adhesion domain formation driven by the curvature-mediated mechanism relies on a novel mean-field approach, in which the elastic energy of the membrane is numerically estimated for various random distributions of bonds. We obtain an empirical expression for the system's free energy, from which we derive the phase diagram of the system. Our analysis reveals that the typical membrane deformations caused by adhesion bonds in biological systems may lead to the formation of adhesion domains with semi-dilute densities of the order of $\sim \xi_\gamma^{-2}$. The conclusions drawn from our analysis are further examined in relation to the important biological system of the immunological synapse (IS). This special cellular junction forms between T cells and antigen-presenting cells as part of the immune response, and is established by two types of adhesion bonds, namely TCR-pMHC and LFA1-ICAM1. The IS is characterized by a unique molecular pattern where the TCR-pMHC form a central cluster at the contact area, while LFA1-ICAM1 adhesion bonds accumulate around it. We locate the system in the two-phase region of our mean-field phase diagram, and identify the IS as a semi-dilute domain with roughly 100 bonds per μm^2, in line with experimental observations.

While our investigation finds that passive (thermodynamic) membrane-mediate mechanisms may be crucially important for the aggregation of the IS, the formation of the TCR-pMHC cluster at the center of the contact area can be only explained by a symmetry breaking mechanism. A widely accepted source for this symmetry breaking is the active cytoskeletal processes originating from actin retrograde flow and dynein-mediated directed transport. To further investigate the interplay between passive and active mechanisms in IS formation, we present and simulate an implicit-membrane lattice-gas model, where the curvature-mediated PMF and the active cytoskeletal-based forces are introduced via simple potentials. The spatio-temporal evolution of the lattice simulations is found to be astonishingly similar to the signature features of the IS formation process. Specifically, we observe that small TCR-pMHC microclusters are initially formed at the periphery of the contact region, and then

migrate (while continuing to grow in size) to the center of the contact area, where they accumulate into a quasi-circular domain. Moreover, we find that this process is completed within a biologically relevant timescale of ~ 30 minutes. Our simulation results, thus, reveal the important role played by the membrane-mediated interactions in regulating the rate of the IS formation process. Explicitly, membrane elasticity facilitates the formation of long-lived TCR-pMHC peripheral microclusters, which are important for T cell activation, thereby allowing sustained signaling over tens of minutes prior to the formation of the central domain, where these signals are terminated.

Keywords: membrane elasticity, thermal undulations, cell junctions, adhesion domains, lattice-gas, coarse-grained, Monte Carlo simulations, condensation transition, mean-field theory, immunological synapse, active and passive forces.

Contents

1 Introduction **6**

1.1 Statistical mechanics of fluctuating membranes 7

1.2 Membrane-mediated interactions between adhesion bonds 9

1.2.1 The Helfrich regime 12

1.2.1.1 Entropic attachment penalty of a single adhesion bond 12

1.2.1.2 Two-body fluctuation-induced attraction 14

1.2.1.3 Many-body fluctuation-induced PMF 14

1.2.2 The van der Waals regime 18

1.2.2.1 Deformation energy of membranes with a single adhesion bond 19

1.2.2.2 Pairwise curvature-induced attraction 22

1.2.2.3 Many-body curvature-induced PMF 23

1.3 Outline of the thesis 24

2 Molecular simulations of membranes in the Helfrich regime **26**

2.1 Introduction 26

2.2 Comparison with the Weil-Farago model 27

2.3 Adhesion domain formation in stressed and confined membranes 32

2.3.1 Membranes under physical confinement 33

2.3.2 Membranes under negative surface tension 34

2.4 Summary 40

3 Formation of semi-dilute adhesion domains in the van der Waals regime **43**

3.1 Introdcution 43

3.2 Mean-field theory 44

3.2.1 Energy calculations 45

3.2.2 Phase diagram 49

3.3 Semi-dilute domains 50

3.4 Summary 53

4 Passive and active mechanisms in the formation of the immunological synapse **55**

4.1 Introduction . . . 55

4.2 Model and simulations . . . 58

4.2.1 Nearest-neighbor approximation . . . 58

4.2.2 Lattice-gas model . . . 60

4.2.3 Monte Carlo simulations . . . 62

4.2.4 Active cytoskeleton forces . . . 62

4.3 Results . . . 64

4.4 Summary . . . 69

5 Conclusion **72**

Appendix **77**

A **78**

Chapter 1

Introduction

Lipid membranes serve as a physical barrier that separates the interior of the cell from its outer environment. They are typically arranged as a bilayer of a number of lipids, such as phospholipids, glycolipids and cholesterol [1]. Similar to the plasma membrane that surrounds the cells, several intracellular organelles such as the mitochondria, the nucleus and the endoplasmic reticulum are also compartmentalized by a lipid membrane. One of the most important roles of lipid bilayers is to regulate the bidirectional flow of ions and other molecules into and out of the cell [2]. Biological membranes are also embedded with numerous types of proteins, which exhibit lateral diffusion in the membrane's plane [3, 4]. Cell adhesion molecules constitute a special class of membrane proteins that enable the attachment of the membrane to various elements, such as the extracellular matrix (ECM), the cytoskeleton and neighboring cell membranes. The adhesion process is mediated by the formation of specific receptor-ligand bonds that anchor the membrane to the adhesive element. Cell adhesion is crucial for the proper function of individual cells and the organism as a whole, and plays a vital role in many biological processes, including cell migration [5], tissue morphogenesis [6], intercellular communication [7], and T cell activation as part of the immune response [8].

One common feature of cell adhesion is the ability of the adhesion bonds to aggregate and form large adhesion domains. For instance, connexon protein complexes aggregate into gap junction plaques that bind opposing cell membranes. Gap junctions directly connect the cytoplasms of two neighboring cells and regulate the exchange of ions and small

molecules, thereby regulating intercellular communication [9]. Likewise, proteins of the integrin family aggregate into clusters called focal adhesion, which physically link the ECM to the cell cytoskeleton. This mechanical linkage not only provides strong anchoring of the cell to the ECM, but also enables the cell to generate traction forces necessary for cellular locomotion [10]. In addition, focal adhesions act as mechano-sensors and promote biological signals that regulate cell growth, survival, proliferation and differentiation [11–14]. Finally, cadherin proteins cluster into adherens junctions that bind neighboring cells within tissues. The formation of this type of adhesion domains is vital for proper tissue organization and architecture maintenance in developing and adult organisms [15,16]. Given the enormous importance of adhesion clusters in biological systems, it is essential to acquire a comprehensive understanding of the biophysical principles governing the formation of these structures.

Due to the highly complexed nature of the cell membrane, several experimental studies have developed model systems containing the key components of biological membranes to gain insights into the adhesion process. These models include lipid bilayers deposited onto solid substrates and thin polymer-coated supports [17, 18]. When incorporated with specific adhesion proteins, such supported membranes may serve as targets for the binding of synthetic ligand coated vesicles or liposomes [19, 20]. These biomimetic systems are able to elucidate many aspects of cell adhesion, such as the effect of density and strength of ligand-receptor bonds on adhesion efficiency [21], as well as estimation of adhesion bonds binding affinity [22]. Supported membranes also constitute new potential applications in designing biosensor nano-devices [23].

1.1 Statistical mechanics of fluctuating membranes

The elastic behavior of lipid bilayers is traditionally studied in the framework of the Helfrich effective surface Hamiltonian [24] for two-dimensional manifolds with local principle curvatures c_1 and c_2. The system Hamiltonian is described in terms of the bending energy of the membrane, and is given by

$$\mathcal{H} = \int \mathrm{d}S \left\{ \frac{1}{2}\kappa \left(c_1 + c_2 - c_0\right)^2 + \bar{\kappa} c_1 c_2 \right\}, \tag{1.1}$$

where the integration is taken over the entire surface of the membrane. In eq. (1.1), κ is the bending modulus of the membrane, $\bar{\kappa}$ is the saddle-splay (Gaussian) modulus, and c_0 is the spontaneous curvature. If one assumes that the two leaflets of the bilayer membrane have similar lipid compositions, the spontaneous curvature can be simply set to $c_0 = 0$. For fluctuating membranes that do not change their topology, the surface integral over the Gaussian curvature term would simply result in a constant, which has no effect on the underlying physics of the system and, thus, can be ignored. A useful way to parametrize the membrane surface is the Monge gauge. Within this parametrization, the membrane is represented by a height function $h(\mathbf{r})$ measured relative to a reference plane, where $\mathbf{r} = (x, y)$ is the two-dimensional position vector. Assuming the small gradient approximation, which essentially states that the membrane does not fluctuate considerably (and, in particular, does not develop "overhangs"), one can re-express the membrane curvature $(c_1 + c_2)$ and the area differential element $(\mathrm{d}S)$ in terms of the membrane's height function. Keeping only quadratic terms in h, one obtains the following simplified version of the effective Helfrich Hamiltonian

$$\mathcal{H} = \int_{A_\mathrm{P}} \frac{1}{2}\kappa \left(\nabla^2 h\right)^2 \mathrm{d}^2\mathbf{r}, \tag{1.2}$$

where, in this case, the integration is taken over the projected area of the membrane, A_P. Eq. (1.2) is the most commonly used form of the Helfrich energy in the literature of membrane biophysics.

The quadratic nature of eq. (1.2) gives rise to a harmonic theory, in which membrane undulations can be viewed as a collection of independent harmonic oscillators. This is done by using the Fourier representation of the height profile

$$\begin{aligned} h(\mathbf{r}) &= \left(\frac{l}{L}\right)^2 \sum_{\mathbf{q}} h_{\mathbf{q}} \exp\left(-i\mathbf{q}\cdot\mathbf{r}\right) \\ \mathbf{q} &= \frac{2\pi}{L}(n_1, n_2) \;\; ; \;\; n_{i=1,2} = \frac{-L}{2l}, \ldots, \frac{L}{2l} \end{aligned} \tag{1.3}$$

where $\mathbf{q}$ is the two dimensional wave vector, l is a microscopic cutoff lengthscale of the order of the membrane thickness ($\approx$ 5nm), and L is the linear size of the membrane such that

$L^2 = A_\mathrm{P}$. In Fourier space the Helfrich Hamiltonian (1.2) reads

$$\mathcal{H} = \frac{l^4}{L^2} \sum_{\mathbf{q}} \frac{1}{2} \kappa q^4 \left| h_{\mathbf{q}}^2 \right|, \tag{1.4}$$

where $q = |\mathbf{q}|$. From eq. (1.4) we observe that the different Fourier modes decouple; thus, each mode constitutes an independent fluctuation degree of freedom of the membrane. For quadratic energy functionals, the equipartition theorem implies that each fluctuation mode contributes an average of $k_\mathrm{B}T/2$ to the system energy, where k_B is the Boltzmann constant and T denotes the system temperature. Thus, the fluctuation spectrum of the membrane obeys

$$\langle \left| h_{\mathbf{q}}^2 \right| \rangle = \frac{L^2 k_\mathrm{B} T}{l^4 \kappa q^4}. \tag{1.5}$$

Eq. (1.5) provides an incredibly useful method for estimating the bending modulus κ of the membrane, by measuring the fluctuation spectrum using flicker spectroscopy [25] or computer simulations [26]. Fitting the data to eq. (1.5) results in typical values of the bending rigidity that lie within the range of $\kappa \approx 10 - 50 k_\mathrm{B}T$ [27].

One can also derive an expression for the mean square height fluctuations of the membrane

$$\Delta_0^2 = \langle h(\mathbf{r})^2 \rangle = \left(\frac{l}{L} \right)^4 \sum_{\mathbf{q}} \langle \left| h_{\mathbf{q}}^2 \right| \rangle \approx \frac{k_\mathrm{B}T}{16\pi^3 \kappa} L^2, \tag{1.6}$$

which gives the "thermal roughness" of the membrane. Note that the mean square fluctuations of a free bilayer are proportional to the system temperature as one would expect, but diverge with the system size L.

1.2 Membrane-mediated interactions between adhesion bonds

The clustering process of membrane adhesion bonds at the surface of membranes requires attractive interactions between them to overcome their mixing entropy. These may originate

from direct electrostatic and Van der Waals interactions [28], or effective forces stemming from cytoskeleton remodeling and the action of motor proteins that actively translocate and redistribute the adhesion bonds [29]. Another interesting mechanism that can facilitate adhesion domain formation is related to the thermodynamics of the membrane itself, which can induce effective forces between the adhesion proteins [30]. Membrane-mediated interactions between adhesion bonds originate from two interrelated mechanisms operating in concert. The first mechanism is related to the suppression of membrane thermal fluctuations by the presence of adhesion bonds, which locally fix the membrane's height [31]. The resulting loss in the membrane's fluctuation entropy can be partially mitigated if the adhesion bonds aggregate into a single domain, which allows the membrane to fluctuate more freely. The second mechanism stems from the local membrane deformations that are imposed by the adhesion bonds. These membrane distortions are minimized once the bonds reside in close proximity to each other, which can greatly relieve the mechanical stress of the system [32]. Thus, membrane curvature and thermal fluctuations induce an effective attractive potential of mean force (PMF) between the adhesion bonds, which may trigger their aggregation. The non-specific membrane-mediated interactions have also been studied in relation to condensation of trans-membrane proteins (membrane "inclusions") [33–35], and in the broader context of "Casimir-like" interactions in condensed matter [36].

The main challenge in analyzing and deriving expressions for membrane-mediated interactions arises from their many-body nature [37], i.e., their non-trivial dependence on the spatial distribution of the adhesion bonds. In a system with a large number of bonds, the PMF acting between each pair of bonds depends on the locations of *all* of the other bonds and, therefore, cannot be expressed as a simple sum of pairwise interactions. To illustrate this complexity, consider the two configurations schematically depicted in Fig. 1.1. In the first configuration [Fig. 1.1(a)], the membrane is attached by two adhesion bonds separated by a distance r_0, whereas in the second one [Fig. 1.1(b)] the membrane is attached by a single bond and another small cluster of three bonds, with the same distance r_0 between them. It is readily apparent that the spectrum of thermal undulations, as well as the degree of membrane curvature, is quite similar in both scenarios and, therefore, the membrane-mediated PMFs are expected to be roughly the same in both cases. In other words, the membrane-mediated force exerted on the single bond in Fig. 1.1(a) by the second bond is

similar to that exerted on the single bond in Fig. 1.1(b) by the three bond cluster, and *not* three times smaller.

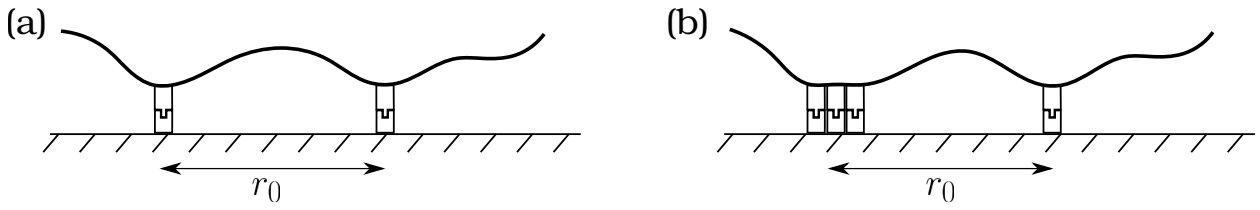

Figure 1.1: Schematics of a membrane bound to a surface by (a) two isolated adhesion bonds, and (b) a single adhesion bond and a small cluster of three bonds. The separation between the two bonds in (a) and between the single bond and the cluster in (b) is identical and equals r_0. The membrane-mediated PMF is similar in both cases, which illustrates its many-body nature.
.

Several theoretical studies have been devoted to characterizing and deriving expressions for the membrane-mediated PMF between adhesion bonds. In a seminal work by Bruinsma, Goulain and Pincus, the aggregation of gap junctions was investigated by considering two opposing tensionless membranes with bending moduli 2κ that are connected to each other at several points [38]. The system Hamiltonian is given by

$$\mathcal{H} = \int_{A_{\mathrm{P}}} \left\{ \frac{1}{2}\kappa \left(\nabla^2 h\right)^2 + V(h) \right\} \mathrm{d}^2\mathbf{r}, \tag{1.7}$$

where the effective potential, $V(h)$, stands for the various interactions between the two membranes, and h is the distance between them. A similar Hamiltonian describes the energy of a single supported membrane with bending rigidity κ and a flat underlying surface. For supported membranes in model systems, a number of factors can contribute to $V(h)$, including short-range van der Waals attraction and excluded volume repulsion, double layer forces, and effective repulsion due to thermal collisions between the membrane and the underlying surface [39]. In the context of the living cell, confinement effects may arise from the ECM, the cytoskeleton and the glycocalyx coating of the cell, which can all be clumped into this effective non-specific potential.

Two important regimes for $V(h)$ have been considered, corresponding to different membrane-surface interactions. The first regime is termed the *Helfrich regime*, and deals with membranes exhibiting large thermal fluctuations. In this regime, $V(h)$ is an effective

repulsive potential (per unit area) arising from thermal collisions between the membrane and the surface. The second regime, termed the *van der Waals regime*, describes membranes with large bending moduli, such that the thermal undulations are small. In this case, the curvature of the membrane dominates the system and, thus, $V(h)$ can be replaced by a Lennard-Jones type of potential. In the following sections, we review results for the thermodynamic behavior of membranes in the Helfrich and the van der Waals regimes, from which insights can be drawn into the fluctuation- and curvature-mediated interactions, respectively.

1.2.1 The Helfrich regime

1.2.1.1 Entropic attachment penalty of a single adhesion bond

An interesting feature of membranes attached to a surface at a single point is that the fluctuation spectrum remains unaffected when compared to a free (unbound) membrane [40]. This rather surprising property can be understood from the fact that the membrane energy is invariant under vertical translations and, thus, one can always position the underlying adhesive surface at the global minimum of the membrane. That the attachment of the membrane to the surface at a single point eliminates its horizontal degrees of freedom with respect to a free membrane implies that the configurational space of the attached membrane occupies a fraction l^2/L^2 of that of the free membrane, where l^2 is roughly the area occupied by the single adhesion bond. Therefore, the ratio between the partition functions of these two systems satisfies $Z/Z_{\text{free}} = l^2/L^2$. Since the free energy of the attached membrane is simply given by $F_1 = -k_{\text{B}}T \ln (Z/Z_{\text{free}})$, the free energy cost associated with attaching a membrane by a single adhesion bond is given by

$$F_1 = 2k_{\text{B}}T \ln \left(\frac{L}{l} \right). \tag{1.8}$$

Eq. (1.8) can also be derived by employing a different approach. Helfrich showed that thermal collisions between the membrane and the underlying surface result in an effective repulsive potential per unit area that scales with the height h of the membrane above the surface

as [41]

$$V_{\mathrm{rep}}(h) \sim \frac{(k_B T)^2}{\kappa h^2}. \tag{1.9}$$

Using this form in eq. (1.7) gives

$$\mathcal{H} = \int_{A_{\mathrm{P}}} \left\{ \frac{1}{2}\kappa \left(\nabla^2 h\right)^2 + C\frac{(k_B T)^2}{\kappa h^2} \right\} \mathrm{d}^2\mathbf{r}, \tag{1.10}$$

where C is an unknown numerical constant. Minimizing eq. (1.10) with respect to h results in the membrane's average height profile that grows linearly with the distance r from the adhesion point (see also Fig. 1.2) according to

$$\langle h(r) \rangle \sim r\sqrt{\frac{k_{\mathrm{B}}T}{\kappa}}. \tag{1.11}$$

Substituting eq. (1.11) in eq. (1.9) results in the effective fluctuation-induced repulsion between the membrane and the surface as a function of r

$$V_{\mathrm{rep}}(r) \sim \frac{k_{\mathrm{B}}T}{r^2}. \tag{1.12}$$

The free energy penalty associated with the attachment of the membrane by the single bond can now be derived by integrating eq. (1.12) over the membrane's projected area (excluding a region of size l around the adhesion point), yielding

$$F_1 = \int_{A_{\mathrm{P}}} V(r)\mathrm{d}\mathbf{r} \simeq \int_l^L 2\pi r \frac{k_{\mathrm{B}}T}{r^2}\mathrm{d}r = 2\pi k_{\mathrm{B}}T \ln\left(\frac{L}{l}\right). \tag{1.13}$$

One readily finds that in order to reconcile eq.(1.13) with eq. (1.8), the scaling behavior of eq. (1.12) can be replaced by the exact form

$$V_{\mathrm{rep}}(r) = \frac{k_B T}{\pi r^2}. \tag{1.14}$$

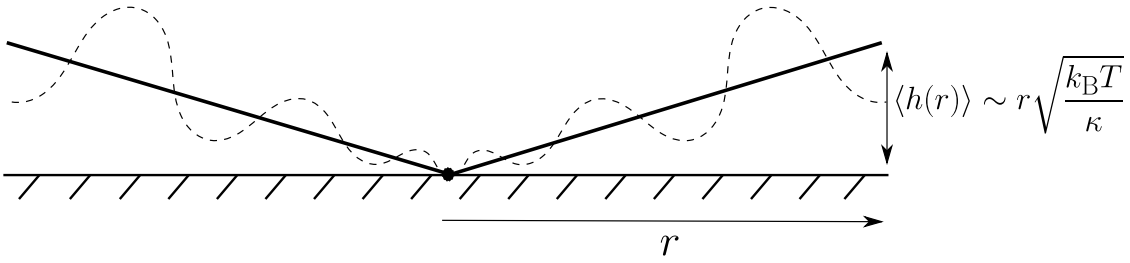

Figure 1.2: Schematics of the mean height profile of a membrane tethered by a single adhesion bond to a surface in the Helfrich regime. The solid line represents the linear growth of the mean height with the distance r from the bond. The dashed curve represents thermal undulations around the average profile.

1.2.1.2 Two-body fluctuation-induced attraction

The effective steric repulsion proposed by Helfrich, which stems from the thermal collisions between the membrane and the surface, may be used to analyze the fluctuation-induced interactions between a pair of membrane adhesion bonds. This is done by considering a membrane attached to the surface at a single adhesion point and the probability density, $p\left[h(\mathbf{r}) = 0\right]$, that the membrane collides with the surface at a distance r away from it [31]. Since this probability density function is directly related to the rate of collision between the membrane and the surface, it should display the same scaling behavior with r as does $V(r)$ (1.14), namely $p\left[h(\mathbf{r}) = 0\right] \sim 1/r^2$. If one thinks of the collision point as the location of the second adhesion bond, then the pair correlation function between the two adhesion bonds should also scales as $g(\mathbf{r}) \sim 1/r^2$, which immediately gives the pair fluctuation-induced PMF

$$\Phi_2(r) \equiv -k_{\mathrm{B}}T \ln\left[g(\mathbf{r})\right] = 2k_{\mathrm{B}}T \ln(r). \tag{1.15}$$

This shows that the fluctuation-induced pair PMF is a long-range (infinitely ranged) attractive potential which, remarkably, is independent of the bending modulus κ. This result has also been verified by computer simulations of coarse-grained bilayer membranes [42].

1.2.1.3 Many-body fluctuation-induced PMF

The study of the clustering process of adhesion bonds traditionally uses a lattice model [43–45], in which the membrane is discretized into patches that may or may not contain adhesion molecules that bind (via receptor-ligand bonds) the membrane to an underlying surface.

Such models constitute discrete versions of the Helfrich continuum surface model of lipid bilayers. Thus, each lattice site is characterized by two variables s_i and h_i. The former parameter characterizes the distribution of adhesion bonds, where $s_i = 1$ corresponds to a membrane segment that is connected to the surface and $s_i = 0$ to a segment which is free to fluctuate. The latter parameter, h_i, represents the local height of the membrane. Analyzing the aggregation behavior of the adhesion bonds by means of computer simulations requires sampling over different distributions of lattice sites, as well as over different height conformations. This may become a computationally expensive task in simulations of large systems. It is, therefore, desirable to develop a model that integrates out the degrees of freedom associated with the height fluctuations and, instead, assigns a potential of mean force between the lattice adhesion sites. Apart from computational simplicity, another advantage of this approach is that it makes possible a direct comparison with the well-investigated two-dimensional (2D) lattice-gas model and, thus, highlights the role played by the membrane-mediated interactions in the aggregation process[1].

Such a lattice model was recently proposed by Weil and Farago (WF) [46], which combines two attractive energy terms:

$$\mathcal{H}_{\mathrm{WF}} = -\epsilon \sum_{\langle i,j \rangle} s_i s_j + \sum_i V_i (1 - s_i). \tag{1.16}$$

The first term constitutes the conventional lattice-gas model, where the sum runs over all pairs of nearest-neighbor lattice sites. The energy $\epsilon > 0$ gained for each pair of nearest-neighbor occupied sites accounts for all the interactions between the adhesion bonds *other than the membrane-mediated PMF*. The latter potential is represented by the second term in eq. (1.16) which, quite unusually, involves summation over the *empty* sites alone. The energy of each empty site measures the amount of free energy lost due to the suppression of the thermal height fluctuations of the corresponding membrane segment. Weil and Farago conjectured that this free energy penalty depends on the distance of the segment from the nearest adhesion bond $d_i^{\min}$, i.e., the distance to the nearest occupied site. This assumption is based on the idea that each of the adhesion bonds restricts the membrane thermal

[1]Note that an opposite approach is taken in refs. [43, 44], where the positional degrees of freedom s_i are integrated out by using the mean-field solution of the 2D lattice-gas model. This introduces an effective membrane-surface interaction energy term in the Helfrich Hamiltonian that depends on the local h_i.

fluctuations mainly in its own vicinity. In other words, the local suppression of thermal undulations is essentially determined by the *nearest* adhesion bond, while the effect of the other more distant bonds is effectively screened out. The energy penalty term, V_i, in eq. (1.16) associated with the (empty) site i is given by

$$V_i = \frac{k_{\mathrm{B}}T}{\pi}\left(\frac{l}{d_i^{\min}}\right)^2, \tag{1.17}$$

which generalizes eq. (1.14) for the free energy density at a distance r from a single isolated adhesion bond. In eq. (1.17), l is the lattice constant (which should be of the order of a few nanometers – comparable to the thickness of the membrane), and $d_i^{\min}$ measures the distance of site i to the nearest occupied site. Note that, in general, $d_i^{\min}$ depends on the distribution of *all* the occupied sites; therefore, the second term in eq. (1.16) represents a many-body PMF between the adhesion bonds. This potential is attractive because most of the entropy is lost at the proximity of the occupied lattice sites, where $d_i^{\min}$ is small. The many-body fluctuation-induced PMF can be evaluated by: (i) constructing a Voronoi diagram for the distribution of adhesion bonds, (ii) calculating the attachment free energy penalty within each Voronoi cell by integrating eq. (1.14) over the area of the given Voronoi cell, and (iii) adding up the free energy contributions of all the Voronoi cells. Thus, the many-body PMF is given by

$$\Phi_N = \sum_{i=1}^{N} \int_{\mathrm{A_i}} \frac{k_B T}{\pi r^2} \mathrm{d}\mathbf{r}, \tag{1.18}$$

where within each Voronoi cell i with area $\mathrm{A_i}$ the distance r is measured from the adhesion bond located inside the cell.

To study the aggregation behavior of adhesion bonds in membranes, Monte Carlo simulations of the WF model were conducted on a triangular lattice and were compared to simulation results of the standard lattice-gas model with only nearest-neighbor interactions, i.e., in the absence of the second term in eq. (1.16). In both sets of simulations, the system exhibited a first order condensation transition at a certain threshold value $\epsilon = \epsilon_c$. The simulation results revealed that the transition value, ϵ_c, of the WF model is smaller than the corresponding value of the standard lattice-gas model at the same density of bonds, typically

by a factor of 2-3. This is depicted in Fig. 1.3, in which the mean number of nearest-neighbor pairs, normalized by the number of occupied sites

$$\langle N_C \rangle = \frac{1}{N} \sum_{\langle i,j \rangle} \langle s_i s_j \rangle, \tag{1.19}$$

is plotted as a function of ϵ. At low values of ϵ, the system is in the "gas" phase and $\langle N_C \rangle$ takes a small value, since the adhesion points are scattered throughout the system. For high values of ϵ, the energy gained from direct interactions overcomes the mixing entropy of the adhesion bonds, which condense and form a large domain. In such configurations, $\langle N_C \rangle$ approaches the value 3, due to the triangular nature of the lattice under inspection[2]. At the onset of the condensation transition, the parameter $\langle N_C \rangle$ exhibits a sharp increase, which is useful for estimating the threshold value ϵ_c required for condensation. In particular, the simulations showed that ϵ_c is smaller than thermal energy $k_{\rm B}T$ in the WF model, and larger than $k_{\rm B}T$ in the standard lattice-gas model. In agreement with previous lattice models that included the membrane explicitly (and not via a potential of mean force) [43–45], the adhesion sites do not form large clusters when $\epsilon = 0$, which implies that the fluctuation-induced interactions alone are not sufficient to allow for the formation of large adhesion domains, but they greatly reduce the strength of the residual interactions required to facilitate cluster formation.

In a subsequent study, Noguchi suggested that the strength of the membrane-mediated interactions can be enhanced by pinning more than one membrane to the surface [47]. He demonstrated this by simulating monolayers of particles that are pinned to each other by gap junctions. In simulations of $N_{\rm lay} = 2$ monolayers, the gap junctions remain dispersed for $\epsilon = 0$, which is consistent with the results of the WF model. However, when the number of monolayers was $N_{\rm lay} > 2$, Noguchi found that the gap junctions exhibited different behavior and condensed into a large stable domain. This behavior can be attributed to the fact that the entropy loss caused by the gap junctions is proportional to the total rate of collisions between the layers in the stack [42], which grows proportionally to the number of *pairs* of colliding surfaces, i.e., to $(N_{\rm lay} - 1)$. Motivated by the results of the molecular

[2]In a cluster composed of N points on a lattice where each occupied site has n nearest-neighbors, the number of nearest-neighbor pair interactions is $\simeq nN/2$ (neglecting finite size effects on the boundaries of the cluster). In a triangular lattice, $n = 6$ and, thus, in a highly packed cluster of adhesion points $\langle N_C \rangle \simeq 3$.

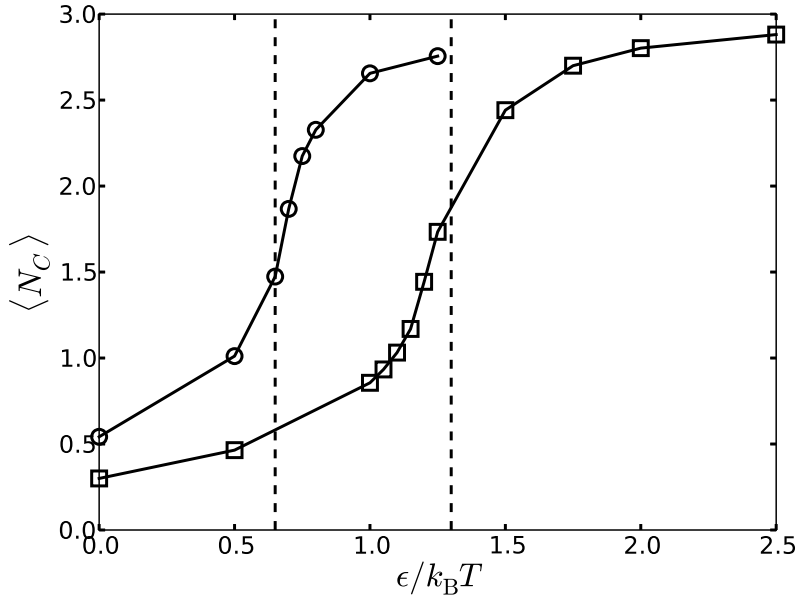

Figure 1.3: Condensation transition curves obtained from Monte Carlo simulations of the Weil-Farago model and the standard lattice-gas model of system with a particle density of $\phi = 0.1$. The average number of nearest-neighbor pairs per occupied site is plotted as a function of the short-range interaction parameter ϵ, for the Weil-Farago model (circles) and for the standard lattice-gas model (squares). The left and right vertical dashed lines are located at $\epsilon_c \simeq 0.65 k_{\mathrm{B}}T$ and $\epsilon_c \simeq 1.3 k_{\mathrm{B}}T$, respectively, and mark the condensation transition. The solid lines serve as a guide to the reader's eyes.

simulations, Noguchi also simulated the WF lattice model with a free energy term which is simply $(N_{\mathrm{lay}} - 1)$ times larger than V_i given by eq. (1.17). The WF model yielded results in very good agreement with the molecular simulations.

1.2.2 The van der Waals regime

In membranes where the thermal undulations are small, the system's free energy is dominated by the bending energy of the membrane. In this case, one may consider the membrane-surface interactions $V(h)$ to take the form of a Lennard-Jones type of potential. For small deviations from the potential's minimum, which for simplicity can be set to $h = 0$, a harmonic approximation for $V(h)$ can be assumed. Hence, the effective Helfrich Hamiltonian of a *tensionless* membrane becomes

$$\mathcal{H} = \frac{1}{2} \int_{A_{\mathrm{P}}} \left\{ \kappa \left(\nabla^2 h \right)^2 + \gamma h^2 \right\} \mathrm{d}^2 \mathbf{r}, \tag{1.20}$$

where $\gamma = \partial^2 V/\partial h^2|_{h=0}$ denotes the strength of the harmonic confining potential, which acts to suppress the thermal fluctuations of the membrane. The influence of the harmonic potential on the membrane can be appreciated by considering the spectrum of thermal fluctuations, which is now given by

$$\langle \left| h_{\mathbf{q}}^2 \right| \rangle = \frac{L^2 k_{\mathrm{B}} T}{l^4 \left(\kappa q^4 + \gamma \right)}. \tag{1.21}$$

Comparing eq. (1.21) with eq. (1.5), it is clear that the harmonic confining potential strongly suppresses the amplitudes of long wavelength (with small q) undulation modes satisfying $\kappa q^4 \ll \gamma$, whereas the fluctuation spectrum is essentially unaffected at much smaller length scales. To put it differently, eq. (1.21) introduces the characteristic length scale

$$\xi_\gamma = \left(\frac{\kappa}{\gamma} \right)^{1/4}, \tag{1.22}$$

which sets the crossover between two regimes. On length scales $r \ll \xi_\gamma$ the membrane's height profile is governed by the bending energy, whereas the $r \gg \xi_\gamma$ regime is dominated by the harmonic confining potential. The parameter ξ_γ also gives the typical length scale over which membrane shape undulations are correlated (see Appendix A). From eq. (1.21), one can also derive the thermal roughness of the membrane in the van der Waals regime

$$\Delta^2 = \langle h(\mathbf{r})^2 \rangle = \left(\frac{l}{L} \right)^4 \sum_{\mathbf{q}} \langle \left| h_{\mathbf{q}}^2 \right| \rangle \approx \frac{k_{\mathrm{B}} T}{8\sqrt{\kappa\gamma}} = \frac{k_{\mathrm{B}} T}{8\kappa} \xi_\gamma^2, \tag{1.23}$$

which can be compared to eq. (1.6) to see that the harmonic confinement eliminates the dependence on the system size. Instead, the mean square fluctuations now depend on the length scale ξ_γ.

1.2.2.1 Deformation energy of membranes with a single adhesion bond

The mechanical equilibrium state of a membrane that is not connected to a surface by adhesion bonds is that of flat bilayer at $h = 0$. This ground state minimizes the confinement energy and, in addition, is characterized by zero curvature energy. What happens when a single adhesion protein locally "pulls" the membrane away from this equilibrium height and

attaches it to an adhesive surface located at $h = h_0 \neq 0$? One way to answer this question is to find the height function $h(\mathbf{r})$ that minimizes the Helfrich Hamiltonian, under the constraint that at the location of the adhesion bond (which can be set to $\mathbf{r} = 0$) the membrane height is fixed at $h(0) = h_0$ where the adhesive surface resides. The equilibrium (mean) height profile is the solution of the corresponding Euler-Lagrange differential equation, which for the Hamiltonian (1.20) is given by the biharmonic equation [38]

$$\nabla^4 h + \frac{h}{\xi_\gamma^4} = 0 \tag{1.24}$$

with the following boundary conditions (BCs)

$$\begin{cases} h(0) & = & h_0 \\ h(r \to \infty) & = & 0 \\ \left.\dfrac{\partial h}{\partial r}\right|_{r=0} & = & 0 \\ \left.\dfrac{\partial h}{\partial r}\right|_{r\to\infty} & = & 0 \end{cases} . \tag{1.25}$$

The solution of eq. (1.24) subject to the BCs (1.25) is

$$h(\mathbf{r}) = -\frac{4}{\pi}\, h_0 \,\mathrm{kei}\left(\frac{r}{\xi_\gamma}\right), \tag{1.26}$$

where $r = |\mathbf{r}|$ and $\mathrm{kei}(x)$ is the Kelvin function [48][3]. The (cross-section) height profile given by eq. (1.26) is sketched in Fig. 1.4, which shows that ξ_γ also acts as a "healing length" over which the deformation caused by the adhesion bond relaxes, and the membrane settles back to the minimum of the harmonic confining potential. Inserting eq. (1.26) into eq. (1.20) yields the average deformation energy caused by a single adhesion bond

$$E_1 = \frac{k_\mathrm{B}T}{2}\left(\frac{h_0}{\Delta}\right)^2 . \tag{1.27}$$

One can straightforwardly verify that the deformation energy E_1 in eq. (1.27) arises from equal contributions of the curvature and interaction energies in eq. (1.20).

[3]The Kelvin is defined as $\mathrm{kei}(x) = \mathrm{Im}K_0\left(xe^{i3\pi/4}\right)$, where $K_0(z)$ is the 0^{th} order modified Bessel function of the second kind.

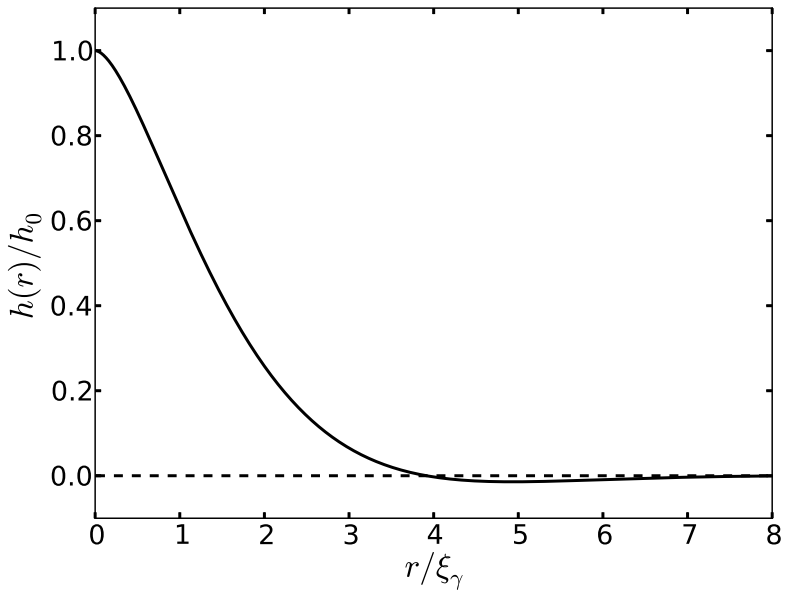

Figure 1.4: The mechanical equilibrium height profile of the membrane in the van der Waals regime as a function of the distance from a single adhesion bond located at the origin and sets the membrane to $h(0) = h_0$. The membrane settles back to $h \simeq 0$ at distances much larger than the characteristic healing length ξ_γ.

A more rigorous way to study the elastic effect of tethering a membrane at a single adhesion point is to consider the partition function associated with the system Hamiltonian (1.20)

$$Z_1 = \int \mathcal{D}\left[h(\mathbf{r})\right] e^{-\beta\mathcal{H}} \cdot \delta\left(h(0) - h_0\right), \tag{1.28}$$

where $\beta = (k_\mathrm{B}T)^{-1}$. Eq. (1.28) involves a statistical average over all possible membrane height configurations under the constraint that at the location of the adhesion bond, $\mathbf{r} = 0$, the membrane is fixed to $h(0) = h_0$. The latter is introduced into the calculation by Dirac's-delta function. The partition function can be analytically derived by using the Fourier representation of the delta function

$$\delta(x - x_0) = \frac{1}{2\pi i} \int_{-i\infty}^{i\infty} e^{-w(x-x_0)} \mathrm{d}w, \tag{1.29}$$

together with the Fourier series of $h(r)$ (1.3), which results in Gaussian integrals that can

be readily evaluated. It follows that Z_1 has the form

$$Z_1 = \frac{Z_0}{\sqrt{2\pi\Delta^2}} \exp\left\{-\frac{k_\mathrm{B}T}{2}\left(\frac{h_0}{\Delta}\right)^2\right\}, \tag{1.30}$$

where Z_0 is the partition function of a membrane in the absence of adhesion bonds. The associated free energy reads[4]

$$F_1 = -k_\mathrm{B}T \ln\left(\frac{Z_1}{Z_0}\right) = \frac{k_\mathrm{B}T}{2}\left(\frac{h_0}{\Delta}\right)^2 + \frac{k_\mathrm{B}T}{2}\ln\left(2\pi\Delta^2\right) \tag{1.31}$$

From eq. (1.31) we identify the ground state energy as the first term on the r.h.s. in line with eq. (1.27), and the second term measures the entropy of thermal fluctuations around the mean profile. Interestingly, the entropic component in eq. (1.31) is found to be independent of the deformation h_0.

1.2.2.2 Pairwise curvature-induced attraction

Pulling the membrane by a second adhesion point, separated by a distance r from the first adhesion bond at $\mathbf{r} = 0$ can be introduced into the statistical mechanical analysis by a second delta function representing the additional height constraint imposed by the second bond. The partition function of a membrane with two adhesion bonds now reads

$$Z_2(r) = \int \mathcal{D}\left[h(\mathbf{r})\right] e^{-\beta\mathcal{H}} \cdot \delta\left(h(0) - h_0\right) \delta\left(h(\mathbf{r}) - h_0\right). \tag{1.32}$$

The associated free energy is given by

$$\begin{aligned}\Phi_2(r) &= -k_\mathrm{B}T \ln\left(\frac{Z_2}{Z_0}\right) \\ &= \frac{2E_1}{1 - \frac{4}{\pi}\mathrm{kei}\left(\frac{r}{\xi_\gamma}\right)} + \frac{k_\mathrm{B}T}{2}\ln\left\{4\pi^2\Delta^4\left[1 - \left(\frac{4}{\pi}\right)^2 \mathrm{kei}^2\left(\frac{r}{\xi_\gamma}\right)\right]\right\},\end{aligned} \tag{1.33}$$

[4] In the second term on the r.h.s. of eq. (1.31), the thermal roughness Δ should be measured in units of the relevant de Broglie wavelength $\Delta \to \Delta/\Lambda_\mathrm{dB}$. The same holds true for the second term on the r.h.s. of eqs. (1.33) and (1.37) below.

where E_1 is given by eq. (1.27). The pair PMF is composed of a deformation energy contribution and an entropic component, which are represented by the first and second terms on the r.h.s. of eq. (1.33), respectively. The former represents the curvature-induced interactions between the pair of adhesion bonds, while the latter gives the fluctuation-induced interactions. Note that both terms describe a short-range pair attraction that spans over a typical range of ξ_γ, unlike the Helfrich regime where the pairwise fluctuation-induced PMF is infinitely long-range. This is a direct result of the harmonic confinement potential introduced in the van der Waals regime which suppresses the long wavelength undulations, whereas in the Helfrich regime, the amplitudes of thermal fluctuations continue to grow with the wavelength.

1.2.2.3 Many-body curvature-induced PMF

For a system with $N \geq 3$ adhesion bonds, the attachment between the surface and the membrane can be incorporated by a set of height constraints satisfying $h\left(\{\mathbf{r}_i\}_{i=1}^N\right) = h_0$, where the bonds are positioned at $\{\mathbf{r}_i\}_{i=1}^N$ and h_0 is the height of the surface. Thus, the partition function of such systems reads

$$Z_N = \int \mathcal{D}\left[h(\mathbf{r})\right] e^{-\beta\mathcal{H}} \cdot \prod_{i=1}^{N} \delta\left(h(\mathbf{r}_i) - h_0\right). \tag{1.34}$$

The partition function Z_N can be evaluated by: (i) using the Fourier representations of the height function and the Dirac-delta functions, (ii) applying N Hubbard-Stratonovich transformations, and (iii) evaluating the resulting Gaussian integrals [45, 49–51]. This leads to the following expression

$$Z_N = \frac{Z_0}{\left(2\pi\Delta^2\right)^{N/2}\sqrt{\det \mathrm{M}}} \exp\left\{-\frac{1}{2}\left(\frac{h_0}{\Delta}\right)^2 \sum_{i,j=1}^{N} \left(\mathrm{M}^{-1}\right)_{ij}\right\}, \tag{1.35}$$

where Z_0 is the partition function corresponding to the Hamiltonian (1.20), with $V(h) = \frac{1}{2}\gamma h^2$ and without adhesion bonds ($N = 0$). The coupling matrix M appearing in eq. (1.35)

is given by,

$$\mathrm{M}_{ij} = \frac{2k_{\mathrm{B}}T}{A_{\mathrm{p}}\Delta^2} \sum_{\mathbf{q}} \frac{\cos\left[\mathbf{q}\cdot(\mathbf{r}_i - \mathbf{r}_j)\right]}{\kappa q^4 + \gamma} \simeq -\frac{4}{\pi}\mathrm{kei}\left(\frac{|\mathbf{r}_i - \mathbf{r}_j|}{\xi_\gamma}\right). \tag{1.36}$$

For a given distribution of adhesion bonds, the PMF is given by the free energy

$$\begin{aligned} \Phi_N\left(\{\mathbf{r}_i\}_{i=1}^N\right) &= -k_{\mathrm{B}}T \ln\left(\frac{Z_N}{Z_0}\right) \\ &= \frac{k_{\mathrm{B}}T}{2}\left[\left(\frac{h_0}{\Delta}\right)^2 \sum_{i,j=1}^{N} \left(\mathrm{M}^{-1}\right)_{ij} + \ln\left(\left(2\pi\Delta^2\right)^N \det \mathrm{M}\right)\right]. \end{aligned} \tag{1.37}$$

The first term on the r.h.s. of eq. (1.37) gives the energy of the height function that minimizes the Hamiltonian (1.20) with the harmonic potential, subject to the height constraints imposed by the bonds. The second term is the entropic contribution due to the thermal undulations around this profile [51]. Note that the energetic and the entropic components in the free energy decouple in this model, which follows from the quadratic nature of the Hamiltonian in q-space. Also note that both terms in eq. (1.37) depend on the elements of the matrix M_{ij} (1.36) in a non-linear manner, which is a mathematical manifestation of the many-body nature of the membrane-mediated PMF.

An interesting observation was made by Speck, Reister and Seifert [50], who argued that the model depicted in eq. (1.37) belongs to the two dimensional Ising universality class (see detailed discussion in Appendix A). Furthermore, if the typical spacing between the adhesion bonds is much larger than the healing length ξ_γ (i.e., for dilute systems), the model can be mapped onto a lattice-gas *with nearest-neighbor interactions*. By estimating the effective interaction parameter between adhesion bonds occupying neighboring sites, the authors of ref. [50] were able to draw the phase diagram of the system and estimate the critical temperature below which clusters appear.

1.3 Outline of the thesis

This thesis is organized as follows. In chapter 2, we analyze the aggregation behavior of adhesion bonds in the Helfrich regime by conducting computer simulations of a coarse-grained model for supported lipid bilayers. We find the conditions under which the condensation

transition occurs and compare our results to the predictions of the WF lattice model. The role of the fluctuation-induced interactions in adhesion cluster formation is further studied by simulating membranes subjected to a physical confinement or to a negative surface tension that, respectively, feature reduced or enhanced thermal undulations. In chapter 3, we investigate adhesion domain formation in the van der Waals regime. We present a novel mean-field theory for the free energy of the system, and determine the condensation transition from the phase diagram of the system. In chapter 4, we study the role of the curvature-induced attraction in a specific biological process, which is the formation of the immunological synapse – a specialized cellular junction that forms between a T cell and an antigen-presenting cell as part of the immune response. This process is driven by both passive (thermodynamic) and active (ATP-driven) forces, and the ideas developed in chapter 3 are used to study their respective roles in the formation of this unique biological pattern. Chapter 5 covers the concluding remarks.

Chapter 2

Molecular simulations of membranes in the Helfrich regime

2.1 Introduction

Various models have been proposed over the years in the attempt to describe and study the behavior and the biophysical properties of lipid bilayers. Typically, different models vary in the resolution by which the describe the system, which directly relates to the time and length scales that can be explored within the framework. For instance, continuum models (such as the Helfrich elasticity model of an infinitely fluctuating manifold – see section 1.1) can be used to study properties of membranes on macroscopic length scales that can reach several micrometers [52]. Such models are applicable to membranes with lateral dimensions that greatly exceed its thickness, but are too crude to describe processes on smaller length scales. On the other hand, high resolution fully-atomistic models display great chemical specificity, but can be used to study small systems of a few tens of nanometers in size over timescales of about a 100-1000 nanoseconds [53,54]. Since many cellular phenomena (including membrane adhesion) occur on larger length- and time-scales, a variety of coarse-grained models have evolved [55–58], which constitute a certain compromise between the fully atomistic and continuum approaches. Within the coarse-grained approach, it is assumed that the detailed atomic nature of the system has a relatively small impact on the mesoscopic behavior under investigation and, hence, a number of atoms are grouped together and treated as

single beads. Depending on the degree of coarsening, coarse-grained models are extremely advantageous in terms of the computation time, allowing one to simulate larger systems and longer processes than those typically explored on atomistic scales. The simulation results can be compared to continuum theoretical models, while retaining a reasonable molecular detail. Notably, several solvent-free models have been presented, in which the water molecules surrounding the membrane are excluded from the simulations. Instead, the hydrophobic effect is introduced via effective interactions between the beads that enable self-assembly and maintain membrane integrity [59,60]. Such implicit-solvent models substantially reduce the CPU time required for equilibrating the system and, concomitantly, allow simulations of substantially larger systems for increasingly larger durations. In this chapter we employ an implicit-solvent coarse-grained membrane model to study the formation of membrane adhesion clusters under several external constraints.

2.2 Comparison with the Weil-Farago model

We begin by testing the validity and accuracy of the WF model for condensation of adhesion bonds. To this end, we use the coarse-grained model proposed by Cooke and Deserno, in which lipids are modeled as trimmers consisting of one hydrophilic (head) and two hydrophobic (tail) beads [61]. This model is less coarse-grained than the one used is ref. [47] and, thus, gives a better representation of lipid membranes which are simulated as bilayers rather than monolayers. A flat plate, which cannot be intersected by the lipids, was placed underneath the lower monolayer at $z = 0$, and the attachment of the membrane to the surface was established by restricting N head beads from the lower monolayer to $z = 0$ and allowing them to move only in-plane. We conducted Monte Carlo (MC) simulations with periodic boundary conditions of a bilayer comprising of $2N_l = 2000$ lipids (where N_l denotes the number of lipids per monolayer) at different densities of adhesive lipids, $\phi = N/N_l$. A slight change in the Cooke-Deserno model was made where, for pairs of adhesive head beads, the pair potential was switched from head-head to tail-tail. While the former pair potential is purely repulsive, the latter also includes a cosine potential well whose depth can be tuned (see eq. (4) in ref. [61]). This attractive part of the pair potential plays the same role played by the standard lattice-gas term in eq. (1.16), with ϵ denoting the interaction energy between

nearest-neighbor occupied sites. By setting the depth of the potential well in the molecular model to ϵ, and by simulating the WF lattice model with same value of ϵ, one can directly compare the two models to each other.

The molecular simulations of the Cooke-Deserno model, which were conducted at zero surface tension, consist of several types of MC moves, including translation of beads, rotation of lipids, and changes in the cross-sectional projected area of the membrane, which are accepted according to the standard Metropolis criterion [62]. To achieve equilibration within a reasonable computing time, two additional move types were also performed. The first move type resolves the problem arising from the slow changes in the amplitudes of the long wavelength bending modes [63]. It involves a collective change in the heights of all the lipids, allowing acceleration and rapid relaxation of these modes. The other process limiting the approach to equilibrium is the slow diffusion of the lipids, especially those pinned to the surface and serve as the adhesion bonds. In order to speed up the aggregation of adhesion domains, one needs to allow the adhesion bonds to "jump" across the membrane. This is accomplished by the second move type, in which two lipids simultaneously experience opposite vertical translations: the free lipid whose head resides closest to the surface is brought down and attached to the surface, while a randomly chosen pinned lipid is lifted and released [42].

We simulated membranes with different concentrations ϕ of adhesion bonds, and for different values of ϵ (measured in units of the thermal energy $k_{\mathrm{B}}T$). Snapshots of equilibrium configurations corresponding to $\epsilon = 0.4k_{\mathrm{B}}T$ and $\epsilon = 1.2k_{\mathrm{B}}T$ are shown, respectively, in Figs. 2.1(A) and Fig. 2.1(B). The concentration in both cases is $\phi = 0.2$. The distinction between the two configurations is clear: In (A) the adhesion bonds are scattered across the membrane in relatively small clusters, while in (B) they are assembled into one big aggregate. The transition between the gas and the condensed phases of adhesion bonds displayed in Figs. 2.1(A) and (B), respectively, occurs at intermediate values of ϵ. In order to characterize the transition value $\epsilon = \epsilon_c$, we compute the non-discrete analogue for $\langle N_C \rangle$ in the WF model. In the molecular simulations, this is achieved by measuring the interaction energy between the adhesive beads, and normalizing it by $N\epsilon$. The condensation transition value ϵ_c is empirically defined via the equality $\langle N_C \rangle = 1.5$. In Fig. 2.2 we plot $\langle N_C \rangle$ as a function of ϵ, the (maximum) strength of the pair interaction, for $\phi = 0.05$ (A) and

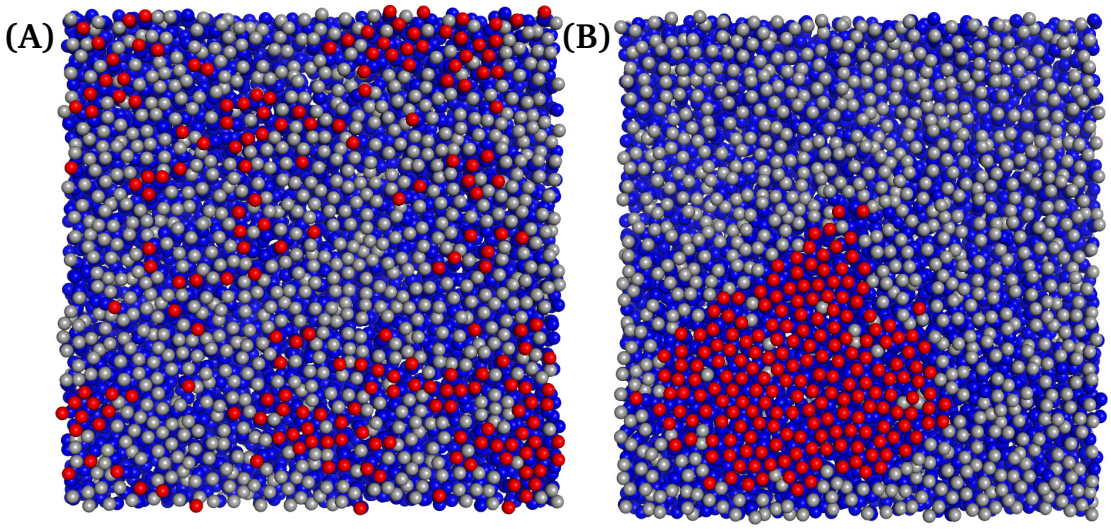

Figure 2.1: Bottom view of a membrane with concentration of adhesion bonds $\phi = 0.2$ for (A) $\epsilon = 0.4k_{\mathrm{B}}T$ and (B) $\epsilon = 1.2k_{\mathrm{B}}T$. The head and tail beads of the lipids are colored in grey and blue, respectively, while the adhesive beads are colored in red. In (A), $\epsilon < \epsilon_c$ and the adhesion bonds are in the gas phase. In (B), $\epsilon > \epsilon_c$ and the adhesion bonds condense and form a single cluster.
.

$\phi = 0.1$ (B). The simulation results, which are plotted in solid squares (with the dashed line serving as a guide to the eye), suggest that the transition between the phases is of first order. The parameter $\langle N_C \rangle$ steeply increases around $\epsilon_c \approx 0.7k_{\mathrm{B}}T$ from a low value reflecting the dispersed distribution of adhesion bonds in the gas phase where the number of pair interactions is small, to a high value characterizing a big cluster where the bonds are closely packed and experience a large number of pair interactions. Also plotted in Fig. 2.2 are the results of lattice simulations of the WF model for identical values of ϕ and for various values of ϵ (solid circles with solid line serving as a guide to the eye). The agreement between the molecular simulations and the lattice simulations of the WF model is very good. The lattice model predicts a very similar value of $\epsilon_c \approx 0.7k_{\mathrm{B}}T$ (for both simulated concentrations), and gives very similar values of $\langle N_C \rangle$ in the gas phase ($\epsilon < \epsilon_c$).

A slight discrepancy between the molecular and lattice simulation is observed in the condensed phase for $\epsilon > \epsilon_c$, where the WF model appears to give higher values for $\langle N_C \rangle$. This deviation between the results of the lattice and continuum molecular models is anticipated considering the nature of the models. In the former, the sites are organized on a perfect triangular lattice, and the energy assigned to every pair of nearest-neighbor occupied sites is

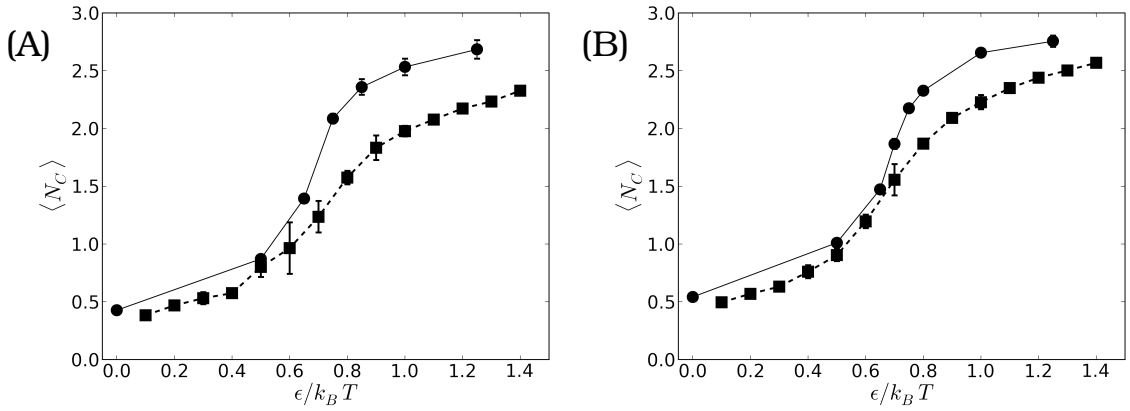

Figure 2.2: The dimensionless (normalized by ϵ) average energy of direct interactions between the adhesion bond, per bond, as function of the pair interaction energy ϵ. Results for $\phi = 0.05$ and $\phi = 0.1$ are shown in (A) and (B), respectively. Solid squares and circles denote the results of the molecular simulations and of the Weil-Farago 2D lattice simulations, respectively. The solid and dashed lines are guides to the eye.

exactly ϵ. In the latter, on the other hand, the bonds within each cluster do not necessarily have a long-range positional order [see, e.g., the snapshot in Fig. 2.1(B)], and ϵ denotes the *depth* of the interaction well. The actual strength of the interaction is expected to be lower than ϵ in the continuum molecular model, which explains why it gives lower values of $\langle N_C \rangle$ than in the lattice simulations.

At even higher values of ϵ, the close agreement between the lattice and the molecular simulations is regained. This occurs due to another phase transition that the clusters undergo, from disordered liquid-like structures into more ordered organizations such as the one displayed in Fig. 2.3(A) for $\phi = 0.2$ and $\epsilon = 3.4 k_{\mathrm{B}} T$. This phase transition can be understood within the framework of the KTHNY theory, which proposes the formation of a two dimensional hexatic phase with a quasi-long range hexagonal (orientational) order [64]. This transition is characterized by the bond orientational order parameter

$$\psi_{6j} = \frac{1}{N_j} \sum_{k=1}^{N_j} e^{i6\theta_{kj}}, \tag{2.1}$$

where the sum runs over the nearest-neighbor bonds k to a given bond j (whose identity is determined by Voronoi tessellation), and θ_{kj} is the angle between the line connecting the pair of bonds j and k and some fixed axis. Averaging over all the bonds within the cluster

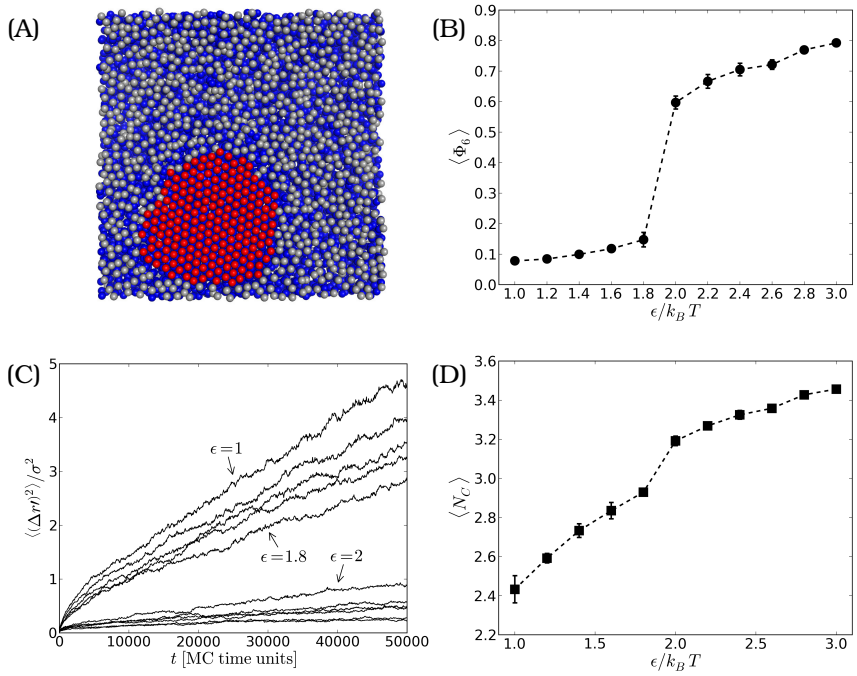

Figure 2.3: The molecular simulation results for a membrane with $\phi = 0.2$ for $\epsilon > \epsilon_c$.(A) Snapshot of an equilibrium configuration with $\epsilon = 3.4k_{\rm B}T$, depicting an adhesion domain organized in the hexatic phase. Color coding as in Fig. 2.1. (B) The mean bond orientational order parameter $\langle \Phi_6 \rangle$ as a function of the pair interaction energy ϵ. The transition into the hexatic phase occurs around $\epsilon_h \approx 1.9k_{\rm B}T$ where a sudden increase in $\langle \Phi_6 \rangle$ is observed. (C) The mean square displacement of the adhesion bonds vs. the simulation time for different values of ϵ. The slope of each curve is a measure for the self diffusion coefficient of the adhesion bonds within the cluster D. The results for $\epsilon/k_{\rm B}T = 1, 1.8, 2$ are marked by arrows. (D) The dimensionless average energy of direct interactions between the adhesion bond (normalized per bond) as function of the pair interaction energy ϵ. A jump in $\langle N_C \rangle$ is observed around ϵ_h.

yields the global orientational order parameter

$$\Phi_6 = \left| \frac{1}{N} \sum_{j=1}^{N} \psi_{6j} \right| . \tag{2.2}$$

Another quantity undergoing rapid variations at the transition is the self-diffusion coefficient of the bonds (relative to the diffusion of their center of mass), defined by

$$\begin{aligned} D &= \lim_{t\to\infty} \frac{1}{4Nt} \sum_{i=1}^{N} \left\langle [(\vec{r}_i(t) - \vec{r}_{\rm cm}(t)) - (\vec{r}_i(t=0) - \vec{r}_{\rm cm}(t=0))]^2 \right\rangle \\ &\equiv \lim_{t\to\infty} \frac{\left\langle (\Delta r\prime)^2 \right\rangle}{4t}, \end{aligned} \tag{2.3}$$

where $\vec{r}_i(t)$ and $\vec{r}_{\rm cm}(t)$ denote, respectively, the position of adhesion bond i and of the center of mass of the cluster at time t (measured in MC time units), and $\langle \cdots \rangle$ denotes statistical average. The transition into the hexatic phase is characterized by (i) an increase in Φ_6, associated with the emergence of orientational order, and (ii) a sharp decrease in D, reflecting a lower mobility of the bonds. In Fig. 2.3(B), we plot our results for $\langle \Phi_6 \rangle$, as a function of ϵ for $\phi = 0.2$. In Fig. 2.3(C) the mean squared displacement of the adhesion bonds (measured in units of σ^2, where σ is the diameter of the beads[1]) is plotted versus the simulation time (measured in MC time units), with the curves, from top to bottom, corresponding to increasingly higher values of ϵ. [Each curve in Fig. 2.3(C) corresponds to a data point in Fig. 2.3(B)]. The curves display a linear increase in $\langle (\Delta r\prime)^2 \rangle$ with t, and the slope of each curve is proportional to D. Both Figs. 2.3(B) and (C) indicate that the transition from disordered-liquid into an ordered-hexatic structure occurs at around $\epsilon = \epsilon_h \approx 1.9 k_{\rm B}T$. Another evidence for the fluid to hexatic transition is also observed in Fig 2.3(D), showing a "jump" in $\langle N_C \rangle$ between $\epsilon = 1.8 k_{\rm B}T$ and $\epsilon = 2.0 k_{\rm B}T$. Note that the values of $\langle N_C \rangle$ in the hexatic phase is *higher* than three, which is the maximum possible value in simulations of the WF model on a triangular lattice. This feature is related to the form of the attractive tail-tail pair potential in the molecular simulations whose cut-off range was set to slightly less that 2.5σ. This implies that, in a closely packed cluster, each adhesion bond weakly interacts with its next- and next-next-nearest neighbors, which explains why $\langle N_C \rangle$ becomes larger than three.

2.3 Adhesion domain formation in stressed and confined membranes

Thus far, we have focused on the aggregation behavior of adhesion bonds in tensionless supported membranes. We now wish to extend our investigations to lipid bilayers subjected to a physical confinement and lateral negative tensions. The former constraint acts to suppress the long wavelength thermal undulations, while the latter amplifies their amplitudes (and, for very large negative values, can even lead to instability). It follows that for systems subjected

[1] In the Cooke-Deserno model, σ is also the range of the head-head repulsive potential [61].

to confinement or negative tension, one should expect that the resulting fluctuation-induced PMF between the adhesion bonds becomes weaker or stronger, respectively. Therefore, such constraints alter the magnitude of the direct short-range attraction required for condensation. In other words, one may presume that physical confinement may hinder the formation of adhesion domains, and that the transition threshold value, ϵ_c, into the condensed state grows with the degree of confinement. Likewise, one can also anticipate that a negative tension would cause a reduction in ϵ_c. It is especially interesting to examine whether ϵ_c can decrease to zero, in which case the adhesion domains will form without an additional short-range potential, i.e., on purely entropic grounds.

In order to address the above issues, we conducted Monte Carlo simulations of a lipid bilayer using the Cooke-Deserno implicit-solvent coarse-grained model [61]. The details of the simulations are similar to those presented in section 2.2. Our simulations for confined membranes included an additional impermeable surface placed above the upper monolayer at $z = z_{\text{conf}}$. Simulations of membranes under constant mechanical surface tension τ were carried out according to the method described in ref. [66]. Similarly to the strategy presented in section 2.2, we followed the aggregation behavior by measuring the average energy of direct pairwise interactions between adhesive beads, normalized per bond and expressed in dimensionless units by dividing it by the potential strength ϵ, to obtain the typical number of contacts per bonds $\langle N_C \rangle$. As will be shown further on, our results suggest that physical confinement might have a very strong impact on ϵ_c, unlike the application of a negative surface tension, which may lead to buckled configurations where we observe the formation of elongated adhesion domains close to the transition point.

2.3.1 Membranes under physical confinement

We first start with our simulation results for non-stressed membranes confined between the supporting underlying surface (on which the adhesive beads reside) and a second impenetrable upper surface. The former is located at $z = 0$, just underneath the tips of the head beads of the lower leaflet, while the latter is placed at $z = z_{\text{conf}} \geq 6\sigma$. The degree of confinement increases when z_{conf} decreases which, in turn, would lead to stronger suppression of the membrane thermal fluctuations and a shift in the transition threshold ϵ_c to larger

values. This trend is demonstrated in Fig. 2.4, showing our simulation results for $z_{\rm conf} = 6\sigma$, 7.5σ, and 9σ in supported membranes with $\phi = 0.1$ (A) and $\phi = 0.2$ (B). For $z_{\rm conf} = 9\sigma$, our results for $\langle N_C \rangle$ (green diamonds) match perfectly with the results obtained for non-confined membranes (black circles). This means that the rate of collisions between the membrane and the upper surface is negligibly small and, therefore, it does not affect the fluctuation spectrum. Lowering the confining surface by a distance equal to the size of a bead and a half to $z_{\rm conf} = 7.5\sigma$ has a more noticeable effect on membrane thermal undulations, which leads to an increase in the condensation transition value from $\epsilon_c \simeq 0.65 k_{\rm B}T$ for non-confined membranes at $\phi = 0.1$ to $\epsilon_c \simeq 0.8 k_{\rm B}T$. As mentioned in section 2.2, ϵ_c is found by the condition $\langle N_C \rangle \simeq 1.5$. For $\phi = 0.2$, the shift is smaller, from $\epsilon_c \simeq 0.6 k_{\rm B}T$ to $\epsilon_c \simeq 0.7 k_{\rm B}T$. When the upper surface is further lowered to $z_{\rm conf} = 6\sigma$, it touches the tips of the head beads in the upper leaflet, as the thickness of the bilayer is equal to the size of six beads. A confining surface located at $z_{\rm conf} = 6\sigma$ completely suppresses thermal undulations, and eliminates the fluctuation-mediated interactions between the adhesion bonds. Under these conditions, the threshold value for aggregation increases to $\epsilon_c \simeq 1.2 k_{\rm B}T$ at $\phi = 0.1$, and $\epsilon_c \simeq 1 k_{\rm B}T$ for $\phi = 0.2$. These values are approximately twice larger than the corresponding values found when no upper plate exists ($\epsilon_c \simeq 0.65 k_{\rm B}T$ and $\epsilon_c \simeq 0.6 k_{\rm B}T$ for $\phi = 0.1$ and $\phi = 0.2$, respectively), which is in accord with the conclusions of refs. [46, 47], that the entropic gain of aggregation compensates for, roughly, half of the loss in mixing entropy of the adhesion bonds.

2.3.2 Membranes under negative surface tension

We next aim to address the implications of applying a negative surface tension. A constant mechanical surface tension introduces an additional energy term to the system Hamiltonian, proportional to the surface area of the membrane. In the Monge gauge, the system Hamiltonian is given by

$$\mathcal{H} = \int \left[\frac{1}{2} \kappa \left(\nabla^2 h \right)^2 + \tau \left(\vec{\nabla} h \right)^2 \right] d^2\mathbf{r}, \tag{2.4}$$

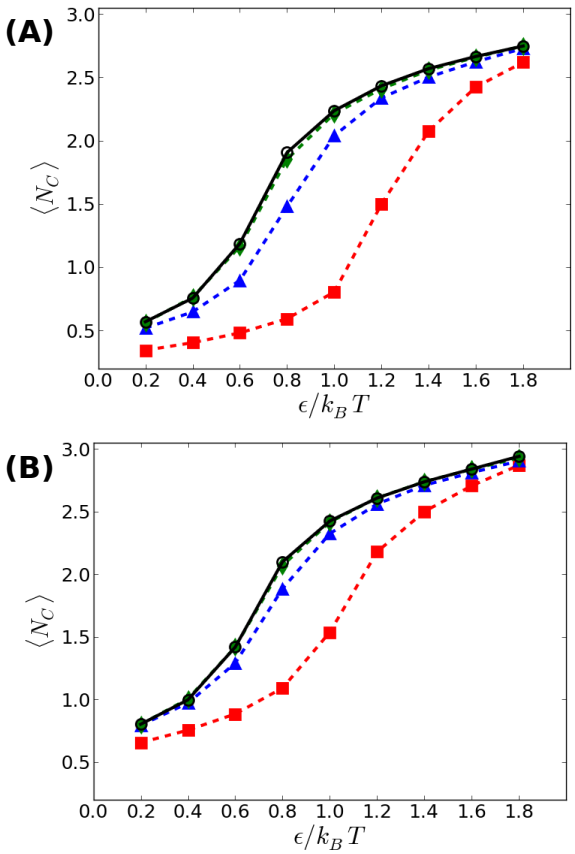

Figure 2.4: The dimensionless energy $\langle N_C \rangle$ in membranes confined by a surface located at $z_{\rm conf} = 9\sigma$ (green diamonds), $z_{\rm conf} = 7.5\sigma$ (blue triangles) and $z_{\rm conf} = 6\sigma$ (red squares), as a function of ϵ, for (A) $\phi = 0.1$, and (B) $\phi = 0.2$. Results for non-confined membranes are denoted by black circles. The lines serve as a guide to the reader's eye. The statistical errors are comparable to the size of the symbols.

where τ denotes the surface tension. The fluctuation spectrum corresponding to eq. (2.4) now reads

$$\langle \left| h_{\mathbf{q}}^2 \right| \rangle = \frac{L^2 k_{\rm B} T}{l^4 \left(\kappa q^4 + \tau q^2 \right)}, \tag{2.5}$$

which can be compared with eq. (1.5) for non-stressed membranes. On length scales larger than the characteristic lengthscale $\xi_\tau \sim \sqrt{\kappa/\tau}$, the imposed surface tension dominates the thermal fluctuations of the membrane, while fluctuation modes with $q \gg 2\pi/\xi_\tau$ remain largely unaffected by it. In general, a negative tension imposed on the membrane leads to a reduction in its projected area, $A_{\rm P}$, and amplifies the long wavelength bending modes. Hence, the fluctuation-induced attraction between the adhesion bonds is expected to be stronger

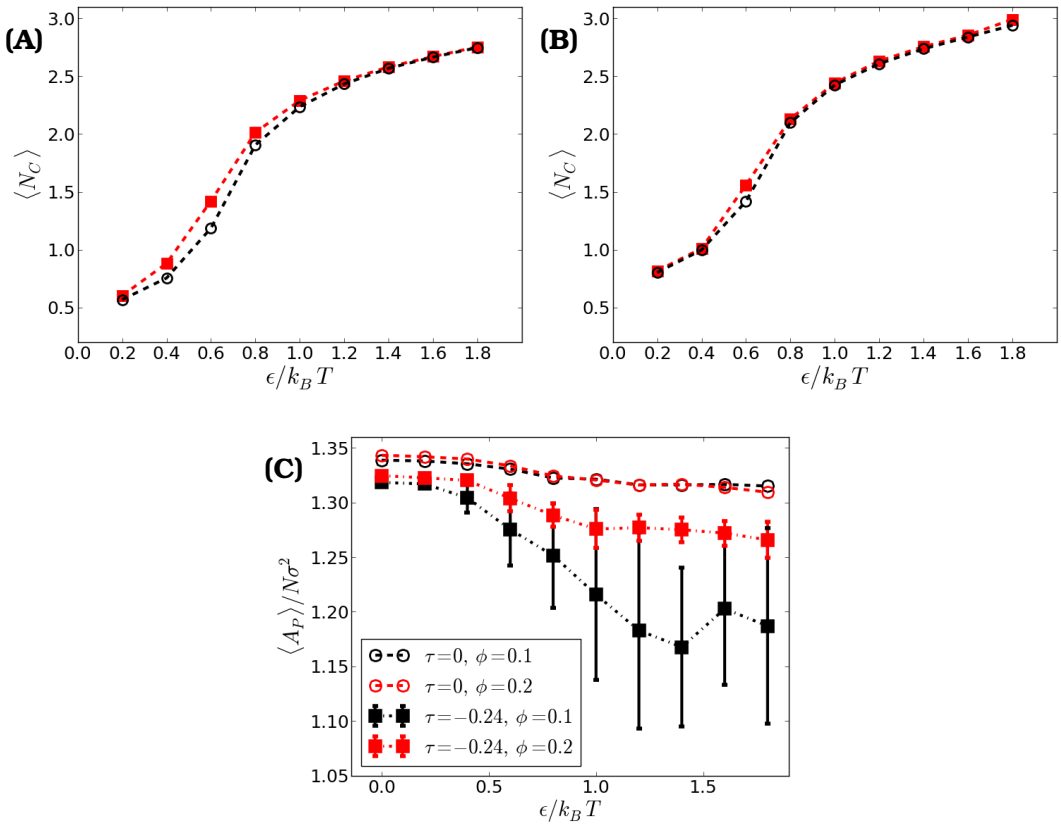

Figure 2.5: The dimensionless energy $\langle N_C \rangle$ in membranes under surface tension $\tau = -0.24 k_{\rm B}T/\sigma^2$, as a function of ϵ for (A) $\phi = 0.1$, and (B) $\phi = 0.2$. The results are plotted in red squares, and are compared with the results for tensionless membranes ($\tau = 0$) that are depicted by black open circles. (C) The mean projected area per lipid as a function of ϵ, for $\phi = 0.1$ (black) and $\phi = 0.2$ (red). Circles denote the results for tensionless membranes, while the results for $\tau = -0.24 k_{\rm B}T/\sigma^2$ are shown in squares. The lines serve as guides to the eye.

which, in turn, implies that the threshold for condensation ϵ_c should become smaller than in tensionless membranes. To test this hypothesis, we simulated the membrane under a negative tension of $\tau = -0.24 k_{\rm B}T/\sigma^2$. We performed two sets of independent MC simulations, one starting from a random distribution of adhesion bonds, and another where initially the adhesion bonds were organized in one large cluster. The system was equillibrated until configurations originating from these two distinct initial conditions achieved similar characteristics. Fig. 2.5 shows our results for $\langle N_C \rangle$ as a function of ϵ for $\phi = 0.1$ (A) and $\phi = 0.2$ (B). Contrary to our expectation to observe a reduction in ϵ_c, the data for $\tau = -0.24 k_{\rm B}T/\sigma^2$ appears almost identical to the results of the tensionless case, with $\epsilon_c \simeq 0.6 k_{\rm B}T$ for both val-

ues of ϕ, and seems to suggest that a negative tension has a minor impact on the aggregation process.

The negative tension, however, does have an impact on the shape of membranes. Freely fluctuating bilayers assume buckled configurations at negative tensions larger (in absolute value) than $\tau_c \simeq -4\pi^2\kappa/A_{\rm P}$ [67, 68] [2]. In this study, non-stressed systems are characterized by $A_{\rm P}/N \simeq 1.33\sigma^2$ [see Fig. 2.5(C)] which, for the bending modulus of the present model membrane $\kappa \simeq 8\,k_{\rm B}T$ [63], gives $\tau_c \simeq -0.24k_{\rm B}T/\sigma^2$. In ref. [69], a similar model membrane consisting of the same number of lipids was simulated and, indeed, for $\tau = \tau_c$ the membrane appeared quite buckled. In supported membranes, however, the emergence of buckled configurations occurs only in membranes with large adhesion domains (i.e., for $\epsilon \gtrsim \epsilon_c$). Fig. 2.6 shows typical equilibrium configuration for $\phi = 0.1$ with $\epsilon = 0$ (A), $0.6k_{\rm B}T$ (B), and $1.0k_{\rm B}T$ (C). Each configuration is shown both in side and bottom views (lower and upper panels, respectively). When the attractive potential is set to $\epsilon = 0$, the distribution of the adhesion bonds is scattered and the membrane remains fairly flat. This indicates that the mixing entropy of the bonds dominates the fluctuation entropy of the bilayer, despite the imposed negative tension [see Fig. 2.6(A)]. For $\epsilon = 1.0k_{\rm B}T$, the short-range pair interactions between the bonds lead to their aggregation. Once the bonds condense, their influence on the thermal behavior of the membrane is greatly weakened, and strong bending undulations appear [see Fig. 2.6(C)]. Close to the condensation transition, at $\epsilon = 0.6k_{\rm B}T$, the system exhibits some interesting features: The amplitude of one of the two longest wavelength bending modes [with wavevector $\vec{q}_{(1,0)} = (2\pi/\sqrt{A_{\rm P}})(1,0)$, or $\vec{q}_{(0,1)} = (2\pi/\sqrt{A_{\rm P}})(0,1)$] grows considerably, and the membrane assumes an anisotropic buckled configuration. The adhesion bonds are concentrated throughout the minimum of the dominating bending mode, forming an elongated domain ("stripe") [see Fig. 2.6(B)]. These observed characteristics represent an intricate balance between the driving forces that govern the thermodynamic behavior of the system. Under negative tension, the system benefits from a reduction in the projected area, leading to a decrease in the Gibbs free energy. The membrane, however, is quite incompressible and, thus, the reduction in $A_{\rm P}$ must be accompanied by an increase in the area stored in

[2] This value for the critical tension for buckling, τ_c, stems from the amplitude divergence of the longest Fourier mode with $q_0 = 2\pi/L$. Looking at eq. (2.5), the amplitude of this mode diverges when $\kappa q_0^4 + \tau q_0^2 \simeq 0$, which is satisfied for a negative tension of $\tau = \tau_c \simeq -\kappa q_0^2 = -4\pi^2\kappa/A_{\rm P}$.

thermal fluctuations whose amplitudes grow. The modes that experience the largest increase in amplitude are the softest ones, corresponding to $\vec{q}_{(1,0)}$ and $\vec{q}_{(0,1)}$ [67] [3]. In our simulations, we seldom observed situations where both these modes were simultaneously excited[4], which can be linked to the mixing entropy of the adhesion bonds. When only one of the long modes is dominant, the contact area between the membrane and the surface, which is available for the presence of the adhesion bonds, is larger than in configurations where both modes are excited.

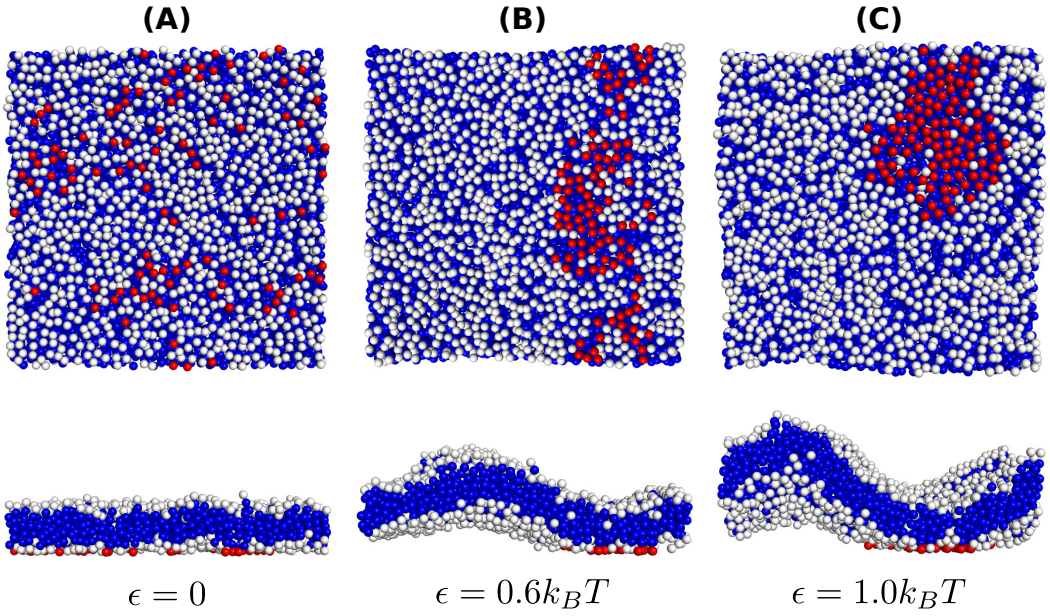

Figure 2.6: Typical equilibrium configurations of membranes under surface tension $\tau = -0.24k_{\rm B}T/\sigma^2$ with density of adhesion bonds $\phi = 0.1$ for (A) $\epsilon = 0$, (B) $\epsilon = 0.6k_{\rm B}T$ and (C) $\epsilon = 1.0k_{\rm B}T$. The figures in the upper and lower rows display bottom and side views of the system, respectively. The head and tail beads are colored in white and blue, respectively, while the adhesive beads are colored in red.

The interplay between the mixing entropy of the adhesion bonds and the contribution of the negative tension to the free energy is further demonstrated in Fig. 2.5(C), depicting the mean projected area $\langle A_{\rm P}\rangle$ (normalized by the number of lipids per monolayer $N_l = 1000$)

[3]Note that in ref. [67], the membrane is simulated in the fixed-area ensemble, $A_{\rm P} = L_xL_y$, with $L_x \neq L_y$ which generates buckled configurations with anisotropic surface tension. Here, we simulate the fixed (isotropic) tension ensemble, where the projected area $A_{\rm P}$ is allowed to fluctuate, but with $L_x = L_y$.

[4]Out of 15 independent realizations of the system corresponding to $\epsilon = 0.6k_{\rm B}T$, in more than half we observed one dominant long Fourier mode. For larger values of ϵ, realizations where both modes were simultaneously excited occurred more frequently.

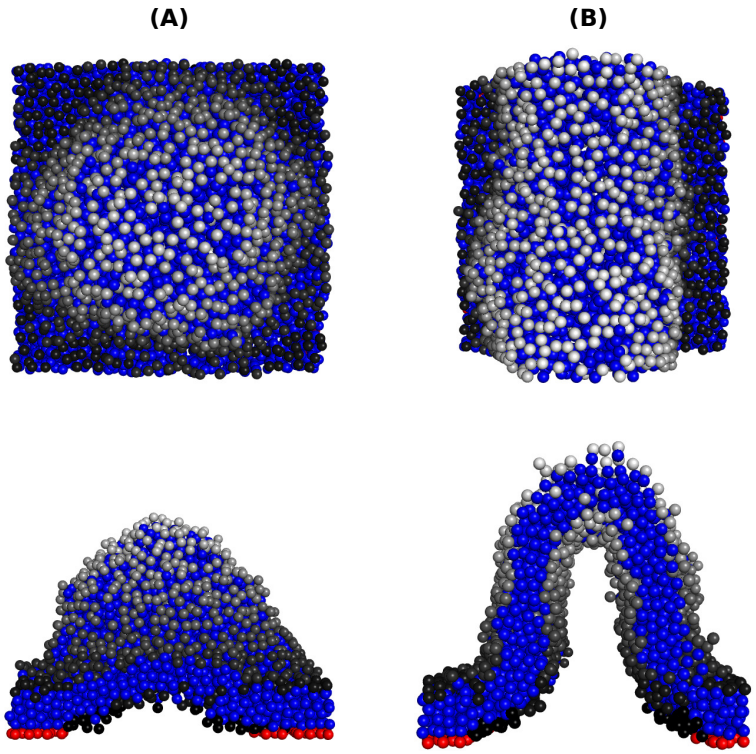

Figure 2.7: Configurations of membranes with $\phi = 0.1$ and $\epsilon = 1.0 k_{\mathrm{B}}T$ under a strong negative tension $\tau = -0.32 k_{\mathrm{B}}T/\sigma^2$, showing a spherical protrusion (A) and a tubular one (B). The upper and lower rows display top and side views of the membrane respectively. The tail and adhesive beads are colored in blue and red, respectively. The head beads are colored in grayscale to reflect their height above the surface, with lighter colors representing a higher bead.

as a function of ϵ for $\tau = -0.24 k_{\mathrm{B}}T/\sigma^2$ (squares) and $\tau = 0$ (circles). In the tensionless case, we observe a very mild decrease in $\langle A_{\mathrm{P}} \rangle$ as ϵ increases, occurring mainly around ϵ_c. For $\tau = -0.24 k_{\mathrm{B}}T/\sigma^2$, $\langle A_{\mathrm{P}} \rangle$ maintains a value close to the tensionless case for $\epsilon < \epsilon_c$, and drops significantly for $\epsilon > \epsilon_c$. In the latter regime, we also observe an increase in the area fluctuations, resulting in larger uncertainties (error bars) in our estimates of $\langle A_{\mathrm{P}} \rangle$. The sharp decrease in $\langle A_{\mathrm{P}} \rangle$ and the concurrent increase in the area fluctuations are anticipated outcomes of a negative surface tension [69]. The fact that they are observed only above the condensation transition is consistent with the picture discussed in the previous paragraph that, below ϵ_c, the effect of the negative tension is largely eliminated by the pressure resulting from the mixing entropy of the adhesion bonds. Note that the sharp decrease in the mean projected area and the increase in the area fluctuations are much more noticeable for $\phi = 0.1$

than for $\phi = 0.2$. This is to be expected because the smaller ϕ, the smaller the restrictions imposed by the adhesion bonds on large thermal undulations, which are directly coupled to the projected area by the highly incompressible character of the membrane.

Applying an even stronger negative tension causes the membrane to lose its mechanical stability. This is demonstrated in Fig. 2.7, showing snapshots in top and side views of membranes with $\phi = 0.1$ and $\epsilon = 1.0 k_{\mathrm{B}}T$ subjected to $\tau = -0.32 k_{\mathrm{B}}T/\sigma^2$. In these snapshots, the head beads are colored in grayscale, with lighter colors indicating beads located higher above the underlying surface. The application of a strong negative tension causes the supported membrane to develop large protrusions with either spherical [Fig. 2.7(A)] or tubular [Fig. 2.7(B)] shapes. The adhesion bonds (which are colored in red, and are only partially visible) are concentrated in the periphery of the protrusion, where the membrane is in contact with the underlying surface. We note that the observed protrusions tend to evolve slowly and, therefore, the snapshots shown in Fig. 2.7 may not represent true equilibrium structures. On the other hand, we also note that very similar equilibrium structures, featuring spherical and tubular protrusions, have been recently observed in an experimental study where supported lipid bilayers were subjected to lateral compression [70].

2.4 Summary

In this chapter, we used solvent-free coarse-grained molecular simulations to study the formation of adhesion domains in supported membranes. We have focused on the Helfrich regime, in which the membrane's thermal undulations are substantial, which results in frequent collisions with the underlying supporting surface. Theses constitute the entropic source of the fluctuation-mediated attractive PMF between the adhesion bonds, which may drive their aggregation into large domains in order to reduce the entropic free energy penalty. Our molecular simulations are found to be in excellent agreement with the recently proposed Weil-Farago (WF) lattice model. Both the molecular and lattice simulations of the WF model show that adhesion domain formation requires an additional direct attraction between the bonds of strength $\epsilon > 0$. In addition, results from the molecular simulations show that the transition into the condensed phase occurs at values of $\epsilon = \epsilon_c$ extremely similar to those predicted by the WF model. Our simulation results for physically confined

membranes reveal that placing the membrane between two impenetrable plates significantly alters the condensation point and requires a stronger direct attraction between the bonds. This stems directly from the fact that the thermal fluctuations of confined membranes are strongly suppressed, which weakens the fluctuation-induced PMF. In the most extreme case, where the membrane is completely flattened between the two plates, the thermal fluctuations are entirely eliminated. This reduces the problem to the phase transition in the standard lattice gas model, and results in a roughly two-fold increase in the value of ϵ_c, which is in accord with the conclusions of the WF model. The implication of the fluctuation-induced shift in ϵ_c is that the fluctuation entropy gained by the condensation of the adhesion bonds compensates for about half of the mixing entropy that is lost in the transition. In other words, the fluctuation-mediated attraction effectively renormalizes the system temperature to about half its value. Thus, while the fluctuation-induced PMF is too weak to promote adhesion domain formation purely on entropic grounds, it greatly facilitates the conditions required for the aggregation of adhesion bonds.

The excellent agreement between the molecular simulations presented here and the WF model lands great credibility to the main idea of the WF model, which is the notion that each adhesion bond suppresses the thermal fluctuations mainly in its immediate vicinity. When studying the system via a lattice model, therefore, one can associate the fluctuation-induced PMF between the bonds with free energies assigned to the empty sites of the lattice. The empty sites represent the fluctuating segments of the supported membrane, and the free energy assigned to each site measures the free energy loss due to the local restrictions imposed on the membrane's thermal undulations. This free energy penalty mainly depends on the distance, $d_{\min}$, between an empty site and the *closest* occupied site (representing an adhesion bond).

We also presented simulations of membranes under negative surface tension which, presumably, fluctuate more strongly than tensionless membranes and, therefore, should exhibit stronger membrane-mediated effects. Surprisingly, we find that the application of a negative tension has a very minor effect on the condensation transition. Nevertheless, once the adhesion bonds are aggregated into a large domain (i.e., for $\epsilon > \epsilon_c$), the negative tension affects the shape of the membrane and causes it to buckle. Below ϵ_c, the adhesion bonds are scattered across the membrane, which prevents the formation of buckled configurations.

Close to ϵ_c, we observed both membrane buckling and the formation of elongated adhesion stripes. Such configurations emerge from a delicate interplay between the mixing entropy of the adhesion bonds, the short-range residual potential, and the applied negative tension. Finally, under a very strong negative tension, we observe tubular and spherical structures protruding out of the membrane's plane, which indicates that the system is at the onset of mechanical instability.

Chapter 3

Formation of semi-dilute adhesion domains in the van der Waals regime

3.1 Introdcution

In this chapter, we focus our attention on the van der Walls regime, in which membranes experience small thermal undulations such that the bending energy dominates the system's free energy. Such situations are frequent in biology as the plasma membrane fluctuations are quite confined due to the presence of the ECM, the underlying cytoskeleton and the glycocalyx coating of the cell. This regime can be studied via the effective Helfrich Hamiltonian given by eq. (1.20), which accounts for the membrane-surroundings interactions via an additional non-specific harmonic confining potential $V\left[h\left(\mathbf{r}\right)\right] = \gamma h^2/2$ that prevents strong membrane fluctuations, and limits the thermal roughness of the membrane to $\langle h^2 \rangle = \Delta^2$.

A single adhesion bond that locally fixes the membrane to $h = h_0$ pulls the membrane away from the minimum of the harmonic potential and leads to an elastic deformation, which relaxes after a typical healing length $\xi_\gamma = (\kappa/\gamma)^{1/4}$ (see Fig. 1.4). In a many-body system with a multiple number of adhesion bonds, this curvature energy induces an effective attractive PMF in order to minimize the elastic deformations. As discussed in section 1.2.2.3, obtaining the curvature-induced PMF requires a full statistical average over the membrane's height degrees of freedom, under the height constraints imposed by the bonds. While an analytical expression for the PMF was previously introduced [see eq. (1.37)], a satisfactory

description of the thermodynamic behavior of the system is still lacking. This is attributed to the highly complicated task of further tracing over the positional degrees of freedom of the adhesion bonds, which is required in order to characterize the condensation transition. Here, we employ a different strategy and derive the phase diagram of the system for a wide range of healing lengths, ξ_γ, and adhesion bonds densities, ϕ. Our investigation relies on a novel mean-field treatment of the system's free energy. We obtain the spinodal and binodal curves and locate the critical temperature of the system, T_c, above which adhesion domains do not form. As shown below, results for different systems exhibit data collapse when $(\Delta/h_0)^2 \sim T/T_c$ is plotted as a function of the rescaled density $\xi_\gamma^2\phi$. Interestingly, we find that the critical point is located at extremely low densities, which is linked to the many-body membrane-mediated PMF. Therefore, close to critically, a phase coexistence is found between two extremely dilute phases, while dense domains form only for $T \ll T_c$, i.e., when each bond deforms the membrane considerably.

3.2 Mean-field theory

The membrane-mediated PMF in the van der Waals regime, Φ_N, as written in eq. (1.37), corresponds to a system with a *given* spatial distribution of N fixed adhesion bonds. The thermodynamics of a system with N mobile bonds is characterized by the free energy F, which depends on the bond density $\phi = aN/A_\mathrm{P}$, where a is a microscopic unit area for which $0 \leq \phi \leq 1$. The free energy F (and, thus, the phase diagram) can be derived from the corresponding partition function $F(\phi) = -k_\mathrm{B}T \ln Z$, where

$$Z = \operatorname*{Tr}_{\{\mathbf{r}_i\}} \left[e^{-\Phi_N\left(\{\mathbf{r}_i\}_{i=1}^N\right)/k_\mathrm{B}T} \right], \tag{3.1}$$

is obtained by integrating out the translational degrees of freedom of the bonds at a given density ϕ. Since the exact calculation of the partition function is out of reach, we invoke a simpler mean-field approach. Within a mean field approximation, the free energy can be written as

$$\frac{aF}{A_\mathrm{P}} = k_\mathrm{B}T \left[\phi \ln \phi + (1-\phi)\ln(1-\phi)\right] + \phi \left\langle \frac{\Phi_N}{N} \right\rangle_\mathrm{MF}, \tag{3.2}$$

where the first term on the r.h.s. accounts for the mixing entropy of the bonds, and the second term represents a mean-field estimation of Φ_N.

We recall that, here, we are interested in the van der Waals regime, which is characterized by small thermal roughness Δ [see eq. (1.23)]. Following previous studies [38, 50], we will also make the assumption that each adhesion bond causes a deformation h_0 significantly larger than Δ. This allows us to drop the second term on the r.h.s. of eq. (1.37) accounting for the entropic contribution of the thermal fluctuations to the PMF in the van der Waals regime. Thus, the curvature-mediated PMF can be expressed just by the first term representing the elastic energy of the ground state

$$\Phi_N\left(\{\mathbf{r}\}_{i=1}^N\right) \simeq \frac{k_\mathrm{B}T}{2}\left(\frac{h_0}{\Delta}\right)^2 \sum_{i,j=1}^{N}\left(\mathrm{M}^{-1}\right)_{ij}, \tag{3.3}$$

with the coupling matrix M, whose entries are given in eq. (1.36). The elastic energy (3.3) can be estimated by considering a lattice of adhesion bonds with spacing $r \sim \sqrt{a}\phi^{-0.5}$, which gives an energy landscape that depends on the ratio r/ξ_γ. This approach yields good analytical expressions for the elastic energy only in the limits $r/\xi_\gamma \gg 1$ and $r/\xi_\gamma \ll 1$ [38]; however, it fails to capture the correct thermodynamic behavior at the intermediate regime $r/\xi_\gamma \sim 1$ where the lattice distribution does not necessarily represent the energy of a typical random distribution of adhesion bonds. Here, we take a different approach and derive an empirical expression for the dependency of the elastic energy on the bonds' density. We computationally obtain this expression by (i) generating membranes with random, rather than ordered, distributions of adhesion bonds, (ii) finding the membrane profile that minimizes the Helfrich elastic energy of each realization, and (iii) describing the computational data for the elastic energy by a fitting function, which applies to the entire range of densities.

3.2.1 Energy calculations

The ground state Helfrich energy corresponding to a random distribution of adhesion bonds is given by eq. (3.3) and can, in principle, be computed by inverting the coupling matrix M (1.36). In practice, this involves a computationally expensive process and, thus, we adopt a different strategy based on a direct minimization of the Helfrich Hamiltonian. This is done

by considering a triangular lattice with lattice spacing l. Each site, i, represents a small membrane segment of area $a = \sqrt{3}l^2/2$, and is characterized by a local height variable h_i. On the lattice, N sites are randomly chosen for the locations of the adhesion bonds, at which we set $h_i = h_0$. The discrete analogue of the Helfrich Hamiltonian (1.20) is

$$\mathcal{H}_{\text{lattice}} = \frac{a}{2}\sum_i \left[\kappa\left(\nabla_i^2 h_i\right)^2 + \gamma h_i^2\right] = \frac{a\kappa}{2}\sum_i \left[\left(\nabla_i^2 h_i\right)^2 + \left(\frac{h_i}{\xi_\gamma^2}\right)^2\right], \tag{3.4}$$

where the discrete Laplacian at site i is given by $\nabla_i^2 = \left[\frac{2}{3}\sum_{j=1}^{6} h_j - 4h_i\right]/l^2$, with the sum $j = 1\ldots 6$ running over the six nearest neighbors of site i. Starting with $h_i = h_0$ at all sites, we simulate Langevin dynamics [72] without the noise term (i.e., at zero temperature), which quickly brings the system to the ground state profile. We measure all lengths in units of the lattice spacing $l = 1$ and the energy scale is set to $k_{\text{B}}T = 1$. The density of bonds is given by $\phi = N/N_s$, where N_s is the number of lattice sites. Most of the calculations were performed on a triangular lattice of 104×120 sites (with periodic boundary conditions) that has an aspect ratio close to 1. We calculate the elastic energy of numerous random realizations at various densities $\phi \leq 0.1$, and for several values of ξ_γ varying from $\xi_\gamma = 5$ to $\xi_\gamma = 10$. These values for the correlation length are chosen such that: (i) ξ_γ is sufficiently larger than the lattice spacing $l = 1$, which reduces the numerical errors associated with the discrete nature of eq. (3.4) to less than a few percents, and (ii) ξ_γ is much smaller than the system linear size, to avoid finite size effects.

From eq. (3.3) and the form of the elements of the coupling matrix M [see eq (1.36)], we infer that for a given set of model parameters ($\kappa,\ h_0,\ \xi_\gamma,\ \phi$), the average elastic energy has the form

$$\left\langle \frac{\Phi_N}{N} \right\rangle_{\text{MF}} = \frac{k_{\text{B}}T}{2}\left(\frac{h_0}{\Delta}\right)^2 f(x) = 4\kappa\left(\frac{h_0}{\xi_\gamma}\right)^2 f(x), \tag{3.5}$$

where $f(x)$ is a scaling function of the renormalized density $x = \xi_\gamma^2\phi$. Note that the values of κ and h_0 can be fixed arbitrarily since the energy scales like κh_0^2 [see eq. (3.5)], and this scaling behavior is automatically satisfied by the Hamiltonian (3.4) which is linear in κ and quadratic in $h_i \propto h_0$. The low-density ($x \to 0$) asymptotic limit of $f(x)$ is found by considering a system with a single bond, which gives the energy per bond in dilute systems

where the typical spacing between the bonds is much larger than the correlation length ξ_γ. From eq. (3.3) for $N = 1$, we read that in this limit $f(x) \to 1$. In the high density limit, i.e., when the spacing between bonds is much smaller than ξ_γ, the membrane assumes a nearly flat configuration at height h_0. Setting $h_i = h_0$ in eq. (3.4) and normalizing the energy by the number of bonds, we obtain the following asymptotic expression $\Phi_N/N \to a\kappa h_0^2/2\xi_\gamma^4\phi$. Using eq. (1.23) and $a = \sqrt{3}/2$, this yields the decaying form $f(x) = \sqrt{3}/(16x)$ for $x \gg 1$. Taking these considerations into account, we propose the following expression for the scaling function

$$f_1(x) = \frac{1 + B_1 x}{1 + B_2 x + \frac{16}{\sqrt{3}} B_1 x^2} \,. \tag{3.6}$$

This form ensures the correct asymptotic behavior at low and high densities, and involves two fitting parameters, B_1 and B_2, to be determined by comparison with the numerical data over the entire range of densities.

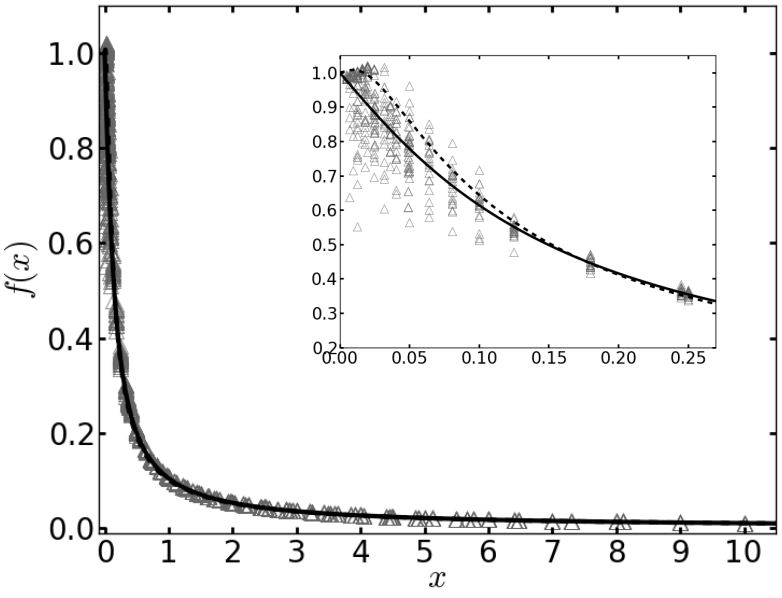

Figure 3.1: The scaling function for the elastic energy $f(x)$ [see eq. (3.5)] as a function of the scaled density x. The numerical results are presented by triangles. The solid and dashed curves depict, respectively, the fitting functions $f_1(x)$ [eq. (3.6)] and $f_2(x)$ [eq. (3.7)] to the data. The inset shows an enlarged view of the data and the fitting functions for $x \ll 1$.

In Fig. 3.1 we plot the computational results (triangles) for the elastic energy per bond, normalized by the energy of a single isolated bond $E_1 = 4\kappa(h_0/\xi_\gamma)^2$ [see eq. (1.27)], which defines $f(x)$ in eq. (3.5). The data, which is plotted against the scaled density $x = \xi_\gamma^2\phi$, exhibits an excellent data collapse over the entire range $x \leq 10$. The solid curve represents the fitting of the data to the form $f_1(x)$ given by eq. (3.6), with the parameters $B_1 \simeq 5.08$ and $B_2 \simeq 9.87$ that give the best fit. The scatter of the computational data is due to the randomness of the simulated configurations. As expected, the scatter is larger for small values $x \ll 1$, where the interaction between the closer pairs of adhesion bonds dominates the energy of the configuration. In fact, for some configurations in this regime, we find $f(x)$ to be slightly larger than unity. This feature is to be expected, and follows from the non-monotonicity of the Kelvin function defining the elements of the coupling matrix M [see eq. (1.36)]. For $x \ll 1$, the PMF between the bonds can be approximated by a sum of pair potentials, as was assumed in ref. [45] (see also discussion in Appendix A). By setting $N = 2$ in eqs. (1.36) and (1.37), it is easy to confirm that the pair PMF is slightly repulsive at large bond separations. We, therefore, conclude that the scaling function $f(x)$ should be non-monotonic; it first increases for very small values of x before dropping to zero at larger values. Furthermore, from the fact that the Kelvin function converges exponentially to zero for large arguments, one can also conclude that the derivative of the scaling function satisfies $df/dx = 0$ at $x = 0$. These features of $f(x)$ in the $x \to 0$ limit are not accounted for by the scaling form $f_1(x)$ proposed by eq. (3.6). Therefore, we also consider the three fitting parameter scaling function

$$f_2(x) = \frac{1 + C_1 x + C_2 x^2}{1 + C_1 x + C_3 x^2 + \frac{16}{\sqrt{3}} C_2 x^3}, \tag{3.7}$$

which, in contrast to $f_1(x)$, correctly captures the behavior of $f(x)$ near $x = 0$. The fit of the scaling function $f_2(x)$ to the computational data is also plotted in Fig. 3.1 (dashed line) with $C_1 \simeq 74.8$, $C_2 \simeq 2174$ and $C_3 \simeq 1836$ that produce the best fit. The difference between $f_1(x)$ and $f_2(x)$ is visible only for $x \simeq 0$, as seen in the inset in Fig. 3.1. Interestingly, even though $f_2(x)$ is better suited to represent the scaling function close to the origin than $f_1(x)$, the latter seems to provide a better fit to the numerical data. In any case, we expect these two functions to yield similar binodal and spinodal curves, except for $x \simeq 0$. This will turn

out to be in the vicinity of the critical point, which is where the validity of the mean-field picture is questionable anyhow.

3.2.2 Phase diagram

Plugging eq. (3.5) into eq. (3.2), the mean-field free energy, F, of a system with adhesion bond concentration ϕ and correlation length ξ_γ reads

$$\frac{aF}{A_\mathrm{p} k_\mathrm{B} T} \simeq \phi \ln \phi + (1-\phi)\ln(1-\phi) + \frac{1}{2\xi_\gamma^2}\left(\frac{h_0}{\Delta}\right)^2 g(x), \tag{3.8}$$

where $g(x) = x f(x)$. With this expression for F, we analytically obtain the spinodal curve enclosing the region of thermodynamic instability by solving $\partial^2 F/\partial\phi^2 = 0$, which yields

$$\left(\frac{\Delta}{h_0}\right)^2 = \frac{x\left(x-\xi_\gamma^2\right)}{2\xi_\gamma^2}\frac{\partial^2 g}{\partial x^2}. \tag{3.9}$$

The binodal curve, which defines the thermodynamic coexistence line, is obtained numerically using a common tangent construction for F. Figs. 3.2(A) and (B) show the phase diagrams calculated using the scaling functions $f_1(x)$ and $f_2(x)$, respectively. In each of these figures, we plot the spinodal curve for $\xi_\gamma = 5$ (solid line) and $\xi_\gamma = 10$ (dotted line), which turn out to be practically indistinguishable. The binodal curves for $\xi = 5$ and $\xi_\gamma = 10$ are given by squares and circles, respectively. As for the spinodal lines, the binodal curves for different values of ξ_γ also overlap each other. Comparing the phase diagrams presented in Figs. 3.2(A) [for $f(x) = f_1(x)$] and (B) [for $f(x) = f_2(x)$], we conclude that the phase diagrams appear to be similar, expect for $x \lesssim 0.6$. This is to be expected because only in this regime, the scaling functions are essentially different (see inset in Fig. 3.1). Fig. 3.2(C) presents an enlargement of the low density regime, showing the binodal [squares for $f_1(x)$, and circles for $f_2(x)$] and spinodal [solid line for $f_1(x)$, and dotted line for $f_2(x)$] curves, for $\xi_\gamma = 10$. Note that the critical point is located at low densities, and the two scaling functions place it at somewhat different values.

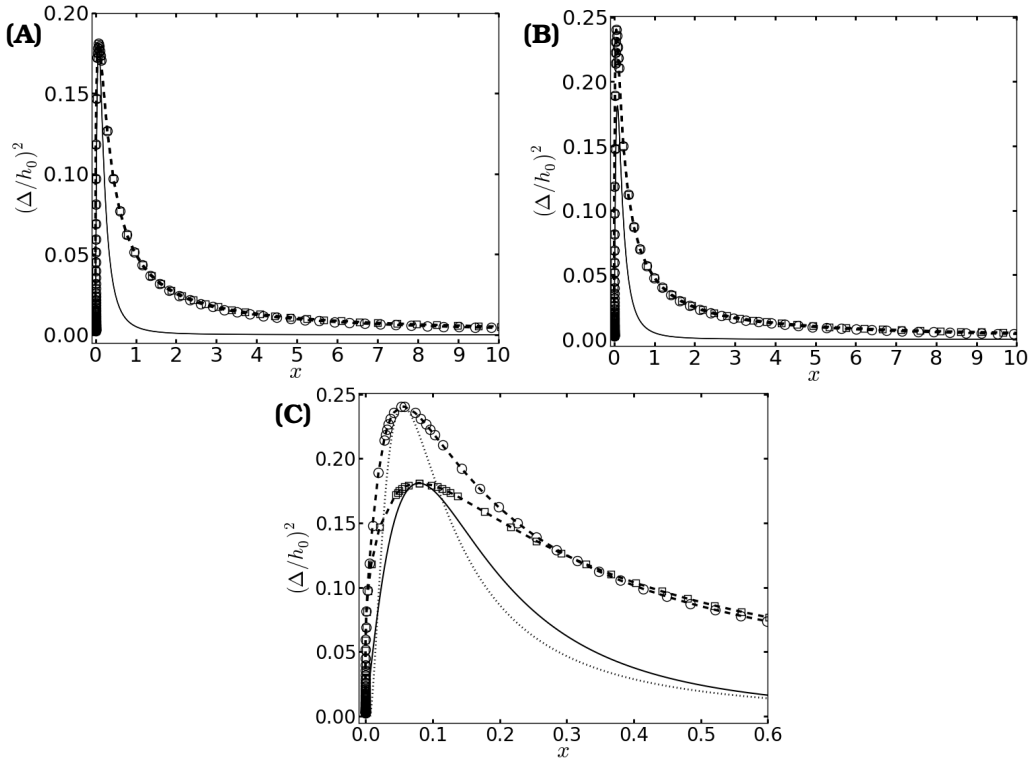

Figure 3.2: (A) The phase diagram corresponding to the free energy eq. (3.8) with $f(x) = f_1(x)$ given by eq. (3.6). The binodal curve is represented by the symbols (with dashed lines serving as guides to the eye), where squares and circles represent data for $\xi_\gamma = 5$ and $\xi_\gamma = 10$, respectively. The two binodal curves nearly overlap each other. The spinodal curves, which are presented by the solid (for $\xi = 5$) and dotted (for $\xi_\gamma = 10$) lines, are also indistinguishable. (B) Same as (A), but for $f(x) = f_2(x)$ in eq. (3.8). (C) A zoom on the vicinity of the critical point, where the differences between the scaling functions $f_1(x)$ and $f_2(x)$ are visible. The phase diagrams are calculated for $\xi_\gamma = 10$. Binodal curves are plotted by squares for $f_1(x)$ and circles for $f_2(x)$. The spinodal lines are presented by the solid and dotted lines for $f_1(x)$ and $f_2(x)$, respectively.

3.3 Semi-dilute domains

Looking at the phase diagram depicted Fig. 3.2, the one feature that stands out is that the critical point is found at very low densities. The precise value of the critical scaled density x_c is, of course, unknown since it depends on the form of the scaling function $f(x)$ [see Fig. 3.2(C)], and because the mean-field picture is not adequate in the vicinity of the critical point. Nevertheless, it is fair to conclude from the data in Fig. 3.2 that $x_c < 0.1$, which implies that $\phi_c = x_c/\xi_\gamma^2 \ll 10^{-2}$ (unless the correlation length is microscopically small, i.e., $\xi_\gamma \sim 1$). The critical temperature T_c can be related to the elastic deformation energy due to

a single bond $E_1/k_{\rm B}T = 0.5\,(h_0/\Delta)^2$. From Fig. 3.2 we read that the critical temperature satisfies $E_1/k_{\rm B}T_c \simeq 2-3$. Another noticeable feature in Fig. 3.2 is the fact that the spinodal and binodal curves of membranes with different values of ξ_γ overlap each other when plotted against the scaled density x. This does *not* a priori follow from the data collapse exhibited in Fig. 3.1, because of the mixing entropy contribution to the free energy. The latter depends on the density ϕ rather than the scaled density x. At low densities, however, we can use the approximation $(1-\phi)\ln(1-\phi) \simeq -\phi$ in eq. (3.2), and then it can be easily shown that the spinodal line [r.h.s. of eq. (3.9)] becomes only a function of x. Thus, the observation in Fig. 3.2 that the phase diagram depends on the scaled density is related to the fact that our investigation focuses on membrane with low densities of bonds.

The fact that the critical point is located at very low densities means that, slightly below T_c, we expect phase coexistence between two low-density phases. From Fig. 3.2 we also notice that for $x \gtrsim 1$, phase separation occurs only when the temperature drops significantly to roughly $T \lesssim 0.2\,T_c$. This implies that low density systems with large ξ_γ will not phase separate unless the bonds considerably deform the membrane ($h_0 \gg \Delta$). In the two phase region of such a system, the scaled density of the condensed phase satisfies $x \gtrsim 1$ which, depending on the value of ξ_γ, could mean that the density ϕ is quite low. We term low-density ($\phi \ll 1$) regions with scaled density $x \sim 1$ as *semi-dilute*, and conclude that the elasticity-mediated interactions may indeed lead to the formation of such semi-dilute domains.

The "weakness" of the elasticity-mediated effect and its inability to induce formation of dense adhesion domains, can be understood by looking at the variation of the total elastic deformation energy [second term on the r.h.s. of eq. (3.8)] with the density of the bonds ϕ. The elastic energy E, normalized per unit area, is plotted in Fig. 3.3 for membranes with $(h_0/\Delta)^2 = 20$ (corresponding to $T \sim 0.2\,T_c$), and $\xi_\gamma = 10$. Also shown in Fig. 3.3 is the free energy of mixing $-TS$ (S denotes the mixing entropy), per unit area, given by the first term on the r.h.s. of eq. (3.8). Both contributions to the free energy are given in units of the thermal energy $k_{\rm B}T$. We observe that total elastic deformation energy increases with ϕ but, somewhat surprisingly, saturates at extremely low densities. The dashed-dotted vertical line in Fig. 3.3 at $\phi = 0.01$ corresponds to $x = \xi_\gamma^2\phi = 1$, and one can read from the data that the elastic energy of the membrane barely increases for $x \gtrsim 0.5$. The interpretation of this finding is that one needs a semi-dilute distribution of about one bond per area ξ_γ^2 to cause

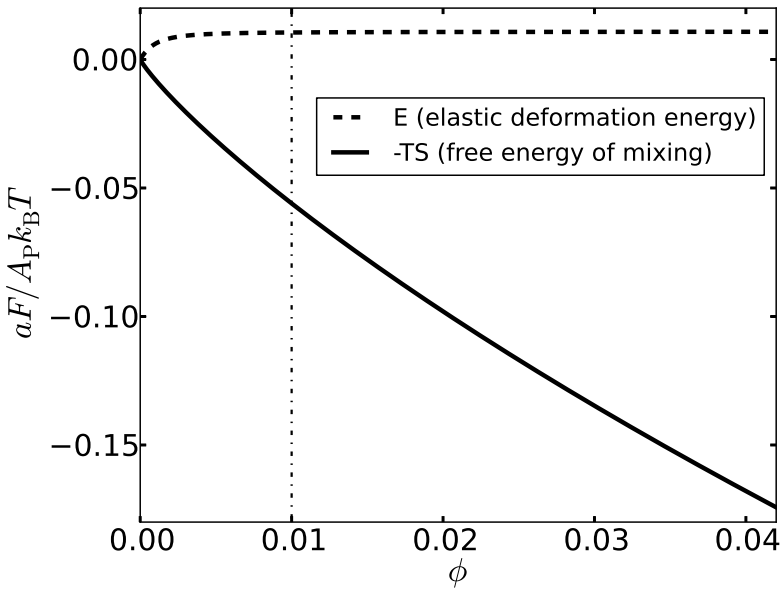

Figure 3.3: The free energy, normalized per lattice site and given in $k_{\rm B}T$ units, as a function of ϕ for $\xi_\gamma = 10$ and $(h_0/\Delta)^2 = 20$. The dashed line is the elastic deformation energy, while the solid line represents the free energy of mixing.

the membrane to adopt nearly flat configurations with $h \sim h_0$. Above the scaled density $x \sim 0.5$, the membrane elastic energy becomes thermodynamically irrelevant, leaving us with only the mixing entropy term which always favors uniform distributions. This explains why phase separation into regions with distinct concentrations of bonds is possible only at densities below $\phi \sim 0.5\xi_\gamma^{-2}$. To state the last conclusion somewhat differently – the elasticity-mediated PMF induces an attraction between the bonds only if their separation is *larger* than ξ_γ. This is an interesting collective (many-body) effect, exhibiting an "opposite" trend compared to the pair PMF, which is attractive at separations smaller than ξ_γ and is screened off at larger distances [see first term on the r.h.s. of eq. (1.33)]. The pair PMF may play an attractive role only between two relatively isolated bonds in inhomogeneous distributions, but such configurations fall outside the framework of the mean-field picture presented in this work.

To put our findings in a biological context, we look at the example of the immunological synapse (IS), which forms at the contact area between the T-cell lymphocyte and a target cell. We analyze the thermodynamic forces driving this process in detail in the following chapter 4. Here, we wish to demonstrate that the elasticity-mediated PMF is likely to play an

important role in IS formation. In this specific example, the cell-cell adhesion is mediated via binding between T-cell receptors (TCR) and MHC-peptide (pMHC) complexes, and between integrin LFA1 and its ligand ICAM1 [73]. These two types of adhesion bonds form a unique structure, in which TCR-pMHC bonds are clustered in its center, while the LFA1-ICAM1 bonds aggregate in the periphery of synapse. It is believed that the central domain, i.e., the TCR-pMHC rich area, plays a pivotal role in regulating T-cell activation [74]. Typically, the bond density within the synapse is around 100 bonds per μm^2, and the bond lengths are 14 nm and 41 nm for TCR-pMHC and LFA1-ICAM1 bonds, respectively [75, 76]. We recall that in the model presented here, h_0 represents the local membrane deformation imposed by a bond relative to the resting height of the membrane. Thus, if we consider the resting separation between the two membranes in the IS to be dictated by the longer bonds, we can estimate the deformation to simply be the difference between the two bond lengths, $h_0 \simeq 27$ nm. Taking the membrane bending rigidity to be $\kappa \simeq 15\ k_{\rm B}T$ and the harmonic potential strength as $\gamma \simeq 6 \cdot 10^5 k_{\rm B}T\ \mu{\rm m}^{-4}$ [77], we arrive to the values $x \simeq 0.5$ and $(\Delta/h_0)^2 \simeq 0.057$ for the coordinates of this point in the phase diagram displayed in Fig. 3.2. Remarkably, the point lies in the two-phase region of the phase diagram, close to the binodal line. This raises the possibility that the TCR-pMHC rich domain may be the semi-dilute phase coexisting with a dilute phase of vanishingly small density. Thus, we speculate that the elasticity-mediated interactions may play an important role in the condensation of the TCR-pMHC signaling domain. They provide attraction which enables the TCR-pMHC bonds to spontaneously aggregate into domains with density comparable to that existing in the IS central zone.

3.4 Summary

In this chapter we analyzed the formation of adhesion domains in the van der Waals regime. In this regime, the thermal fluctuations of the membrane are small and, therefore, the system free energy is dominated by the energy, which is determined by the elastic bending energy and the harmonic confining potential. We have presented a novel mean-field approach to study the condensation transition of the system. Our approach is based on an empirical expression for the average elastic deformation energy of a membrane as a function of the density of

adhesion bonds, which was obtained numerically for random distributions of adhesion bonds. We found that the phase diagrams of dilute systems with different values of densities ϕ and healing lengths ξ_γ are practically identical when the inverse deformation energy $(\Delta/h_0)^2 \sim T/T_c$ is plotted against the rescaled density $x = \xi_\gamma^2 \phi$. Our results show that the phase coexistence regime is largely concentrated in a region where $0 < x \lesssim 1$, and that the critical point is located at very small of x. Therefore, the curvature-mediated interactions may cause the system to phase separate into an extremely dilute phase with $x \simeq 0$ and a semi-dilute phase $x \simeq 1$. Highly condensed domains with $x \gg 1$ can only be formed if the membrane is considerably deformed, but in such cases one can no longer use the Monge representation to study the system. Thus, we conclude that the curvature-induced interactions are too weak to promote formation of tightly packed domains, but can lead to semi-dilute adhesion domains where the typical separation between the adhesion bonds is set by the healing length ξ_γ.

Interestingly, we find that the mature immunological synapse (IS) between a T cell and an antigen-presenting cell is characterized by an adhesion domain of TCR-pMHC bonds with densities of roughly $x \simeq 1$. For the system parameters of the IS, we find that our mean-field model for domain formation driven by membrane curvature is indeed able to generate domains with comparable densities to those found in the IS. This finding is in line with several recent studies suggesting that passive thermodynamic processes can describe the short-time condensation of adhesion clusters of the IS, without evoking any active processes in the cytoskeleton (see, e.g., [78], and refs. therein). Forces stemming from cytoskeletal activity may be essential during the later stages of IS pattern formation and stabilization [79, 80]. In the following chapter, we take a closer look at the manner by which active and thermodynamic (passive) mechanisms govern the process of IS formation.

Chapter 4

Passive and active mechanisms in the formation of the immunological synapse

4.1 Introduction

The adaptive immune system heavily relies upon the ability of T cells to properly interact with antigen-presenting cells (APCs). The contact area between the two cells is established by specific receptor-ligand bonds that crosslink the plasma membranes of the T cell and the APC. The key players in this cellular recognition process are the two T cell membrane proteins T cell receptor (TCR) and lymphocyte function-associated antigen 1 (LFA1) that respectively bind to peptide displaying major histocompatibility complex (pMHC) and intercellular adhesion molecule 1 (ICAM1) embedded in the APC's plasma membrane [2, 81]. During T cell activation, the TCR-pMHC and the LFA1-ICAM1 receptor-ligand bonds are redistributed and form a unique geometric pattern of concentric supra-molecular activation centers (SMACs) within approximately 15-30 minutes of initial contact [73,82]. In this special arrangement, which is commonly referred to as the immunological synapse (IS), TCR-pMHC bonds are concentrated into a central SMAC (cSMAC), while the LFA1-ICAM1 adhesion bonds form a surrounding ring termed the peripheral SMAC (pSMAC) [74, 83]. This molecular redistribution is thought to play an important role in signal regulation [84], T cell

proliferation [85], and focalized secretion of lytic granules and cytokines [86].

Extensive research effort has been devoted to understanding the mechanisms governing the formation of the special architecture of the IS. Mounting evidence from experimental studies point to the actin cytoskeleton as a vital element in controlling the centripetal motion of TCR-pMHC and LFA1-ICAM1 bonds towards their final locations [87]. In the early stages of IS formation, the T cell's actin meshwork reorganizes into actin-free and actin-rich zones in the center and periphery of the contact area, respectively. Later on in the process, the actin-depleted area constitutes the location of the cSMAC of the IS, while the pSMAC is located at the peripheral actin-rich zone [88]. Moreover, actin polymerization occurring at the periphery of the contact area results in centripetal actin retrograde flow that is crucial for protein translocation [89, 90]. It has been hypothesized that actin retrograde flow produces viscous forces on the intracellular part of TCRs, which lead to their centripetal motion [91–94]. Furthermore, directed transport by dynein motor proteins along the cytoskeletal microtubules has been identified as another adenosine triphosphate (ATP)-driven process contributing to protein localization in the IS [95, 96]. These experimental evidences have led to the notion that IS formation is governed by active cellular processes related to the cytoskeleton activity.

Interestingly, several theoretical studies have suggested that passive (non-active) mechanisms may also be involved in the formation process of the IS [78, 97, 98]. Membrane-mediated attraction emerges as one of these mechanisms, as demonstrated by our calculations in the previous chapter, and by other theoretical studies also considering the binding kinetics of the adhesion bonds [99]. It has been argued that membrane-mediated interactions between adhesion bonds in the IS may result in patterns that are not only extremely similar to those observed experimentally, but also form on biologically relevant timescales [78,97,98].

In chapter 3, we have analyzed the curvature-induced interactions between adhesion bonds and demonstrated that TCR-pMHC bonds can phase separate from LFA1-ICAM1 bonds and form domains with similar densities to those in the IS [100]. However, conventional phase separation theories are insufficient to explain the bullseye pattern of the IS, i.e., the aggregation of TCR-pMHC bonds at the central contact area and the accumulation of LFA1-ICAM1 bonds at the periphery. This very particular structure seems to be directly linked to the activity of the actin cytoskeleton, especially to directed transport of

TCR-pMHC by dynein motors along microtubules [96], and the actin retrograde flow which induces a centripetal force on the TCR-pMHC bonds [79, 101]. It may also be related to the depletion of actin from the center of the contact area, which occurs at the very beginning of the IS formation process. The cytoskeleton is also expected to have a direct influence on the membrane-mediated interactions between the TCR-pMHC bonds. This follows from the attachment of the T cell's membrane to the actin cytoskeleton by various molecules, such as proteins from the ezrin-mesoin-radixin (ERM) family [102], phosphatidylinositol 4,5- bisphosphate (PIP2) [103, 104] and coronin 1 [105]. This coupling between the membrane and the cytoskeleton directly impacts the shape of the membrane and, thus, may modify the membrane-mediated PMF. Here, we extend the analysis of chapter 3 on the membrane elasticity-induced formation of TCR-pMHC domains, by including the aforementioned cytoskeleton-related effects, and studying the interplay between the passive and active mechanisms.

In order to follow the process of IS formation, we develop and simulate a simple lattice model that constitutes a discrete representation of the contact region between the T cell and the APC. A schematic picture depicting the contact area and its lattice representation is shown in Figs. 4.1(A) and (B), respectively. The lattice sites can be: (i) empty, or singly occupied by either (ii) a mobile point representing a TCR-pMHC bond, or by (iii) an immobile point representing an attachment protein between the membrane and the cytoskeleton. The latter are absent from the actin-depleted central region of the contact area. In this coarse-grained physical framework, the cell membranes are implicitly accounted for by nearest-neighbor interactions that represent the PMF originating from the membrane deformation energy. The cell cytoskeleton is not modeled explicitly in our coarse-grained simulations, but is implicitly introduced via an effective potential that generates the active cytoskeleton forces. Moreover, since we focus on the aggregation dynamics of TCR-pMHC bonds, we do not study the very rapid remodeling process of the actin cytoskeleton (which is completed within less than a minute from the initial contact between the T cell and the APC [88]), but consider a system where a central actin-depleted region has already been formed. Below, we elaborate on the specifics of the model and simulations.

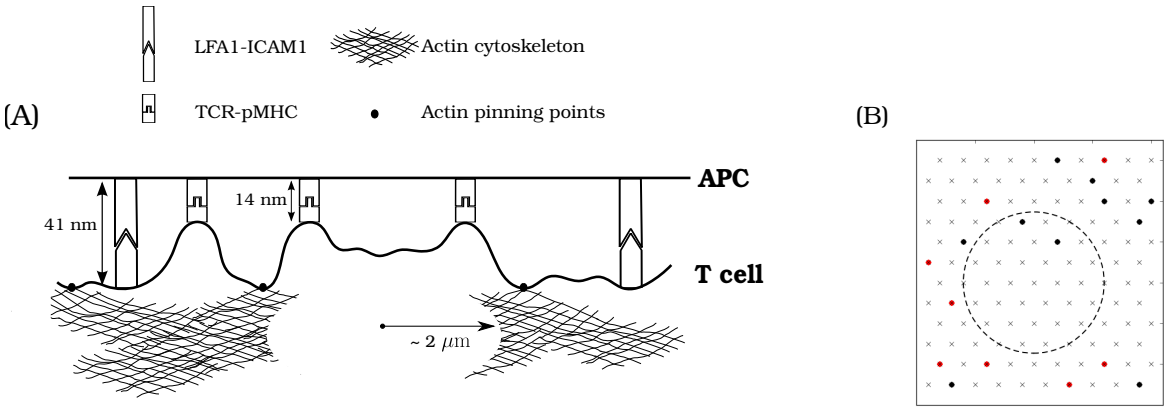

Figure 4.1: (A) Schematics of the contact area between the membranes of the T cell and the APC. The two membranes are connected by two types of adhesion proteins: LFA1-ICAM1 and TCR-pMHC with bond lengths of 41 nm and 14 nm, respectively. The T cell's membrane is attached to the cytoskeleton by a set of actin pinning proteins. A central region in the contact region of diameter $\simeq 4\ \mu$m is devoid of actin filaments. (B) Schematics of the lattice representation of the contact area shown in (A). The lattice sites can be either empty (in which case they are marked by the "x" symbols), or occupied by a single TCR-pMHC bond (black circles) or by a single actin pinning point (red circles). The latter are immobile and are excluded form the actin-depleted central region of the system, represented by the dashed circle.

4.2 Model and simulations

4.2.1 Nearest-neighbor approximation

The membrane-mediated interactions between TCR-pMHC bonds can be studied within the van der Waals regime. We focus on dilute systems, where the many-body PMF is well-approximated by the sum of pairwise interactions that depend only on the distance r between the adhesion bonds (see section 1.2.2.3). From eq. (1.33), the pairwise curvature-induced attraction between a pair of TCR-pMHC is given by

$$\frac{\Phi_{\rm att}(r)}{k_{\rm B}T} = \frac{\Phi_2(r) - \Phi_2(r\to\infty)}{k_{\rm B}T} = \left(\frac{h_0}{\Delta}\right)^2 \frac{\frac{4}{\pi}\mathrm{kei}\left(\frac{r}{\xi_\gamma}\right)}{1-\frac{4}{\pi}\mathrm{kei}\left(\frac{r}{\xi_\gamma}\right)}, \tag{4.1}$$

where we have shifted the PMF such that it vanishes for large separations ($r\to\infty$). For T cells, the values of the healing length and the thermal roughness are roughly given by $\xi_\gamma \simeq 100\,$nm and $\Delta \simeq 8\,$nm [65], respectively, while the value of the deformation caused by a

TCR-pMHC bond is set by the mismatch in bond length with respect to the LFA1-ICAM1 bonds, $h_0 = 41 - 14 = 27\,\mathrm{nm}$ [75, 76]. The pair PMF, $\Phi_{\mathrm{att}}/k_{\mathrm{B}}T$ (expressed in units of the thermal energy), is depicted by the solid line in Fig. 4.2 as a function of the normalized pair distance r/ξ_γ, for the aforementioned values of the systems parameters ξ_γ, Δ and h_0. In addition to the membrane-mediated interactions between TCR-pMHC bonds, we also need to calculate the pair PMF between the TCR-pMHC bonds and proteins that pin the T cell membrane to the actin cytoskeleton. These interactions are obviously repulsive due to the large differences in the height of the membrane at the locations of these two proteins ($h = 0$ at the pinning sites compared to $h = h_0 = 27\,\mathrm{nm}$ at the sites of the TCR-pMHC bonds). The repulsive pair PMF can be derived from the partition function

$$Z_B = \int \mathcal{D}\left[h(\mathbf{r})\right] e^{-\beta\mathcal{H}} \delta\left(h(0) - h_0\right) \delta\left(h(\mathbf{r})\right), \tag{4.2}$$

which differs from the partition function (1.32) by one height constraint. The resulting repulsive pair PMF is given by

$$\frac{\Phi_{\mathrm{rep}}(r)}{k_{\mathrm{B}}T} = \frac{1}{2}\left(\frac{h_0}{\Delta}\right)^2 \frac{\left(\frac{4}{\pi}\right)^2 \mathrm{kei}^2\left(\frac{r}{\xi_\gamma}\right)}{1 - \left(\frac{4}{\pi}\right)^2 \mathrm{kei}^2\left(\frac{r}{\xi_\gamma}\right)} \tag{4.3}$$

and is depicted by the dashed line in Fig. 4.2 for similar values of system parameters. From Fig. 4.2 it is clear that Φ_{rep} is a purely repulsive potential of range $r \simeq \xi_\gamma$ that quickly decays to zero at larger separations.

At separations smaller than ξ_γ, one has to take into account direct excluded volume (hard core) interactions between the adhesion proteins. Since these are missing in the calculation of the partition functions, a purely repulsive potential diverging for $r \to 0$ must be added to Φ_{att}. The full pair potential between TCR-pMHC bonds is, thus, reminiscent of a Lennard-Jones potential, i.e., repulsive at very short distances and attractive at an intermediate finite range. Conversely, from Fig. 4.2 we see that for $r < \xi_\gamma$, Φ_{rep} sharply increases similarly to an excluded volume potential. We thus conclude that the membrane curvature itself serves as a source of repulsion between TCR-pMHC bonds and actin pinning proteins, which renders the addition of explicit excluded volume (hard core) interactions unnecessary

in this case.

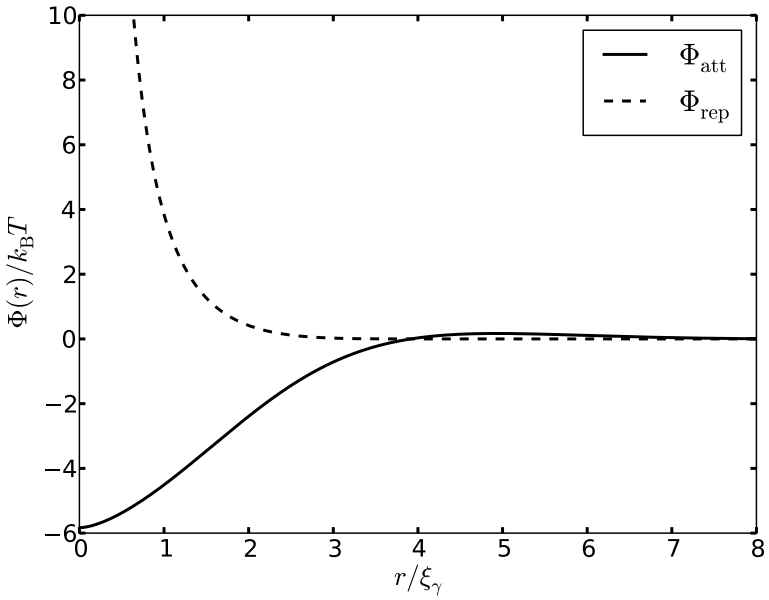

Figure 4.2: Curvature-induced interactions: the solid line depicts the curvature-induced attraction between two TCR-pMHC bonds, while the dashed line stands for the curvature-induced repulsion between a TCR-pMHC bond and a membrane-cytoskeleton pinning point.

4.2.2 Lattice-gas model

Domain formation under the influence of short-range pairwise attractive interactions can be conveniently studied within the framework of the classical discrete lattice-gas (Ising) model with a nearest-neighbor attraction of strength ϵ (see also our discussion on the WF model in section 1.2.1.3). In this framework, each lattice site can be occupied by at most one lattice point, in order to account for the short-range excluded volume repulsion. Here, we study the IS formation process by considering a triangular lattice with lattice spacing $\xi_\gamma = 100\,\mathrm{nm}$, which is comparable to the range of the membrane-mediated interactions between the TCR-pMHC bonds, and also to the typical spcaing between them in the central domain of the IS. This sets the spatial resolution of our model, and allows us to ignore direct (e.g., van der Waals and diploar [28]) and lipid-mediated [109] interactions between the various proteins in the system since, typically, the range of these interactions does not extend beyond $\lesssim 10$ nm. The linear size of the system is roughly $L = 10$ μm (we simulate a lattice of 99×114

sites with an aspect ratio close to unity), which is representative of the dimensions of the contact area. The model includes two types of lattice points representing the TCR-pMHC bonds (type A) and the membrane-cytoskeleton pinning proteins (type B). The former are mobile, while the latter are located at fixed lattice sites. Both A-A and A-B interactions are purely repulsive at short separations (see section 4.2.1), and this feature is accounted for by prohibiting multiple occupancy of a lattice site. At a distance ξ_γ, the A-A interactions are attractive [see eq. (4.1) and Fig. 4.2], and this is represented in the model via a nearest-neighbor interaction energy of strength $\epsilon = \Phi_{\rm att}(r = \xi_\gamma) = -4.5\ k_{\rm B}T$. We do not consider next-nearest-neighbor interactions, despite of the fact that the $\Phi_{\rm att}$ does not fully decay at $r = \xi$. The reason for this decision is the many-body nature of the membrane-mediated PMF, which becomes important at the onset of the formation of adhesion clusters. In high density domains, each adhesion bond interacts with the proximal bonds in the first surrounding shell, whose very presence screens the interactions with the slightly more distant bonds in the next shells [46]. The model does not include explicit representation of the LFA1-ICAM1 bonds. The effect of these bonds is incorporated in the statistical-mechanical calculations of the PMFs through the parameter $h_0 = 27\,\text{nm}$ [see eqs. (4.1) and (4.3)], which is the bond length mismatch between LFA1-ICAM1 and TCR-pMHC bonds[1].

The densities of the TCR-pMHC bonds (type A lattice points) and the membrane-cytoskeleton pinning proteins (type B) greatly vary between different experimental works (if reported at all). We therefore set their values in the simulations based on the following considerations: Type A points aggregate to form the cSMAC, which is a circular domain of radius $\sim 2\ \mu$m that almost fills (at the end of the process) the actin-depleted central region. The latter includes about 1200 lattice sites, and the number of type A points is set to a slightly smaller value $N_A = 1000$. We note that since the lattice spacing is set to $\xi_\gamma = 100$ nm, the density of the TCR-pMHC bonds in a cluster is $\simeq 80$ bonds/μm^2, which is indeed above the threshold density required for full T cell activation [73, 74]. A reasonable estimate for the spacing, $l_{\rm P}$, between membrane-cytoskeleton pinning proteins is a distance of a few hundred nm [110]. In what follows, we show results for systems where the average

[1]More accurately, the effect of the LFA1-ICAM1 bonds is represented by the uniform harmonic potential in Hamiltonian (1.20). The utility of this approach was demonstrated in chapter 3, where we employed a more fine-grained lattice model with a microscopic spacing of 5 nm and an explicit representation of the membrane.

spacing between type B points is set to $l_{\rm P} = 300\,{\rm nm}$. To avoid further complication of our model, we neglect the binding/unbinding kinetics of the membrane-cytoskeleton linkers and assume that the number of type B points is fixed. Nevertheless, we note here that results of simulations with $l_{\rm P} = 500$ nm (i.e., with a fewer number of type B points) exhibit negligible differences. The type B points can be found everywhere on the lattice, except for the central actin-depleted region. They are randomly distributed to account for local variations in $l_{\rm P}$, but we do not allow two type B points to occupy nearest-neighbor lattice sites in order to ensure a fairly uniform distribution and avoid type B clusters.

4.2.3 Monte Carlo simulations

We perform Monte Carlo (MC) simulations to study the evolution of the lattice model. While MC simulations are designed for statistical ensemble sampling at equilibrium, they can be also used to effectively generate Brownian dynamics in lattice models. The simulations consist of move attempts of a randomly chosen type A point to a nearest lattice site, which is accepted according to the standard Metropolis criterion [62]. During a single MC time unit, $\tau_{\rm MC}$, each type A point experiences (on average) one move attempt. Mapping the MC time unit to real time, t, can be achieved by considering the two-dimensional diffusion relation $\langle r^2 \rangle = 4Dt$, where $\langle r^2 \rangle$ denotes the mean square displacement and D is the diffusion coefficient. For the MC simulations, each point moves a distance of the lattice spacing $\xi_\gamma = 100\,{\rm nm}$ and, therefore, $\tau_{\rm MC} = \xi_\gamma^2/4D$. This can be compared to typical values for the diffusion coefficient of T cell membrane proteins $D \simeq 0.1\ \mu{\rm m}^2/{\rm sec}$ [111], which yields $\tau_{\rm MC} \simeq 25$ msec.

4.2.4 Active cytoskeleton forces

Active cytoskeleton processes are not modeled explicitly in our simulations, but are instead represented by the effective forces that they induce on the TCR-pMHC bonds. Two active processes are considered, namely (i) actin retrograde flow, and (ii) dynein minus-end directed transport toward the microtubule organizing center (MTOC) that is translocated towards the central actin-free area [88]. These may be viewed as complementary mechanisms since they produce the same net effect of transport toward the center, while operating at different

regions of the system. Explicitly, dynein-driven transport governs the dynamics at the central actin-depleted area, while actin-retrograde flow is believed to predominate at the periphery of the system.

Experimental studies reveal that the velocity of the actin retrograde flow towards the center of the contact area achieves a maximal value of $v_{\max} \simeq 0.1$ μm/sec at the periphery of the contact area. As the flow proceeds toward the center of the contact area, it decreases to approximately $0.5v_{\max}$, and finally vanishes at the edge of the central actin-depleted region [89, 112]. The flow generates a centripetal force on the TCR-pMHC bonds with magnitude proportional to the flow velocity. Inside the actin-depleted region, the centripetal motion of the TCR-pMHC bonds continues, but is now driven by the activity of dynein motors. This has been concluded by experiments showing that in the absence of dynein motor activity, the TCR-pMHC bonds do not penetrate into the actin-depleted region, but instead accumulate around it [96]. These experiments also suggest that the centripetal velocity of TCR-pMHC bonds transported by both actin retrograde flow and dynein motors is roughly twice larger than the velocity in the absence of motor activity, which suggests that the effective centripetal force induced by both mechanisms is of the same order of magnitude. Taking these various considerations into account, the combined active cytoskeleton forces are introduced to the model via the following effective potential that depends on the distance r from the center of the system

$$\Phi_{\text{active}}(r) = \begin{cases} f_0\, r & r \leq R_{\text{P}} \\ 2f_0\,(r - R_{\text{P}}) + f_0 R_{\text{P}} & r > R_{\text{P}}, \end{cases} \tag{4.4}$$

where R_{P} is the outer radius of the pSMAC, which is the region where the flow of actin becomes weaker [112]. This effective potential generates a centripetal force of magnitude f_0 for $r \leq R_{\text{P}}$, and $2f_0$ for $r > R_{\text{P}}$. The former region includes the actin-depleted region ($0 < r < R_{\text{C}}$), where the force is associated with dynein transport, and the pSMAC ($R_{\text{C}} < r < R_{\text{P}}$), where the force originates from actin retrograde flow. The latter region corresponds to the periphery of the contact area, where actin retrograde flow is stronger and produces an effective force which is twice larger. A schematic depicting the forces associated with the potential Φ_{active} at different regions of the contact area is shown in Fig. 4.3. Based

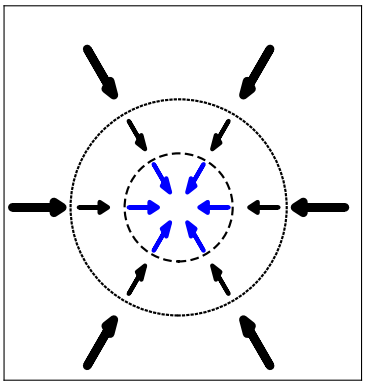

Figure 4.3: Effective active cytoskeleton forces acting on the TCR-pMHC bonds in different regions of the T cell-APC's contact area. The inner dashed circle marks the edge of the central actin-depleted region with radius $R_{\rm C} = 2\mu$m, while the outer dotted circle marks the edge of the pSMAC, and has a radius $R_{\rm P} = 4\mu$m. The black and blue arrows represent effective centripetal forces arising from the actin retrograde flow and directed transport by dynein motors, respectively. For $r < R_{\rm P}$, the magnitude of the active centripetal force is set to $f_0 = 0.1\,$pN (small arrows), while for $r > R_{\rm P}$ the force is set to a twice larger value of $2f_0 = 0.2\,$pN, and is indicated by large arrows.

on confocal images, we set $R_{\rm C} = 2$ μm and $R_{\rm P} = 4$ μm [91]. In order to determine the value of f_0, we use the observation that the actin retrograde flow causes a small peripheral microcluster (a few hundred nanometers in size) to move toward the cell's center at a velocity of $v_c \simeq 20\,$nm/sec [113]. We, thus, performed short MC simulations for a single microcluster composed of 10 TCR-pMHC bonds, which is initially located at the outer region of the system. We measured the velocity of the centripetal movement of the microcluster as a function of f_0, and found that it attains the value of v_c for $f_0 = 0.1\,$pN. Comparable forces have been measured in experiments of optically trapped microbeads coupled to actin retrograde flow of similar velocity [114].

4.3 Results

The spatio-temporal evolution of the system has been analyzed from 10 independent MC runs starting with different random distributions of both type A and B points. Typical snapshots from different stages of the process are shown in Fig. 4.4, with the type A and B points presented by black and red dots, respectively. At $t = 0$, the type A points are

randomly distributed outside of the inner actin-depleted regime (Fig. 4.4a). Within less than one minute, the type A points coalesce and form small peripheral microclusters consisting of $\lesssim 20$ points (Fig. 4.4b), which begin to move centripetally. Several type A points have already reached the center system at this stage. The peripheral microclusters are believed to play a vital role in initiating and sustaining TCR signaling [106, 115]. As time proceeds, the clusters further coarsen, which decreases their mobility and slows down their centripetal motion (Figs. 4.4c-e). The increase in the size of the clusters also causes them to be more affected by the presence of the type B points that act as repelling obstacles. This further restrains the centripetal movement of the microclusters, which have to "navigate" their way through the "curvature corrals" that the type B points form. We also observe in Figs. 4.4c-e the gradual increase in the size of the central domain, which is the destination where the microclusters accumulate. After 45 minutes (Fig. 4.4f), almost all type A points reside in the central domain. The dynamics of the MC simulations, as depicted in Figs. 4.4a-e, closely resembles epifluorescence and total internal reflection fluorescence (TIRF) microscopy images of the IS formation process. Specifically, the microscopy images show the generation of similar microclusters, their drift to the center of the contact area, and their accumulation at the center of the contact area [94, 116]. The simulations exhibit a very good agreement with the experimental observations not only with regard to spatial evolution of the system, but also with respect to the time scales of the different stages of the process. Fig. 4.4g depicts the percentage of type A points located in the central domain at the actin-depleted area. About 90% of the lattice points have been accumulated at the center after roughly 40 minutes, which agrees very well with the times reported in the literature for cSMAC formation.

Figs. 4.5a-c show snapshots from simulations in which dynein activity is turned off. This is done by modifying the effective potential (4.4) such that $\Phi_{\text{active}}(r < R_{\text{C}}) = f_0 R_{\text{C}} = Constant$, and thus, the associated force vanishes at the actin-depleted area where the dynein motors operate. For this model system, we observe formation of peripheral microclusters that move centripetally, but do not enter the actin-depleted area. Instead of forming a central quasi-circular domain, the type A points now accumulate in a ring-shaped domain at the edge of the actin-depleted region. Interestingly, very similar ring-like structures have been observed in experiments where dynein activity was inhibited by dynein heavy chain

ablation [96]. From the agreement with the experimental results we conclude that cSMAC formation requires that centripetal forces act on the TCR-pMHC bonds in the actin-depleted area, and that the origin of these forces is the action of the dynein motors.

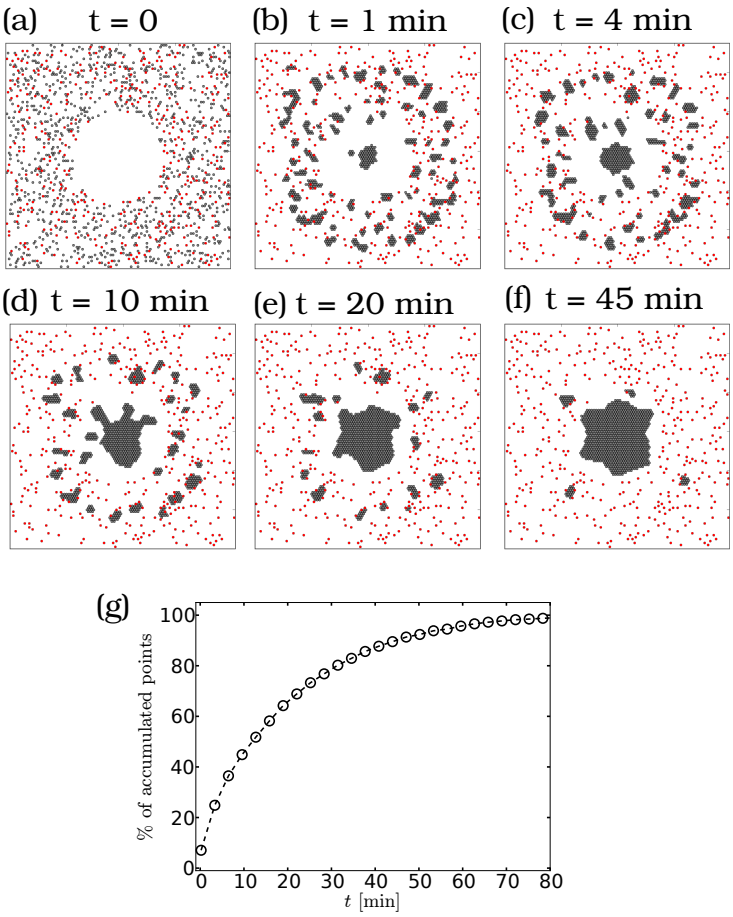

Figure 4.4: Simulation snapshots depicting the aggregation process of the TCR-pMHC bonds (type A, black dots) at different times: (a) The random initial distribution, (b-d) early stage formation, coarsening, and centripetal drift of microclusters, and (e,f) late stage accumulation of microclusters and cSMAC formation. The red dots represent the cytoskeleton pinning proteins (type B). (g) The percentage of type A bonds located at the central actin-depleted area as a function of time.

The results displayed in Figs. 4.4 and 4.5 appears to be in agreement with the widely-held view that the active cytoskeleton forces due to actin retrograde flow and the dynein motors determine the final destination of the TCR-pMHC bonds (i.e., the center of the contact area when dynein activity is enabled, and the inner edge of the actin-rich zone when it is disabled). The results also demonstrate that while a central domain located inside the actin-depleted area constitutes the equilibrium state of the system from a pure ther-

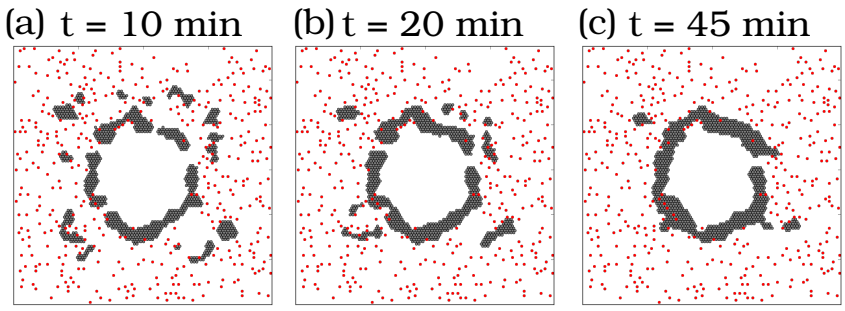

Figure 4.5: Simulation snapshots depicting the evolution of the system in the absence of dynein forces at the center. Color coding as in Fig. 4.4.

modynamic perspective, membrane-mediated interactions do not contribute significantly to the centripetal accumulation of the TCR microclusters over the biologically relevant time scales. This is demonstrated in Fig. 4.6a-d showing snapshots from simulations where Φ_{active} is completely turned off, leaving the system to evolve only under the influence of the passive membrane-mediated interactions. Neither centripetal motion nor central accumulation of TCR-pMHC bonds are observed in this set of simulations. However, the data seems to indicate that the membrane-mediated interactions play an important role in facilitating the formation and coarsening of peripheral TCR microclusters, which are known to be essential for an adequate T cell immune response. The importance of the passive interactions in inducing the formation of the TCR microclusters is also illustrated in Fig. 4.7, showing snapshots from yet another set of simulations. Here, the nearest-neighbor membrane-mediated attraction between the type A points is muted by setting $\epsilon = 0$, while the effective centripetal potential Φ_{active} (4.4) is retained. The simulations reveal that, in this case, the type A points do not form microclusters but instead move individually and quickly accumulate at the center of the system. Since the mobility of a single point is higher than that of a cluster, it is expected that the aggregation process is completed in a shorter time than required in the presence of membrane-mediated interactions. Our computational results show that, indeed, all type A points arrive at the central area in less than 6 seconds (see Fig. 4.7g). We note here that the rate of the accumulation process depicted in Fig. 4.7 may be exaggerated, since it implies that individual (non-clustered) TCR-pMHC move centrally at a velocity which is about 5 times larger than the velocity of the actin retrograde flow. This problematic dynamic feature is an artifact of the lattice MC dynamics that we employ. Since the focus of interest

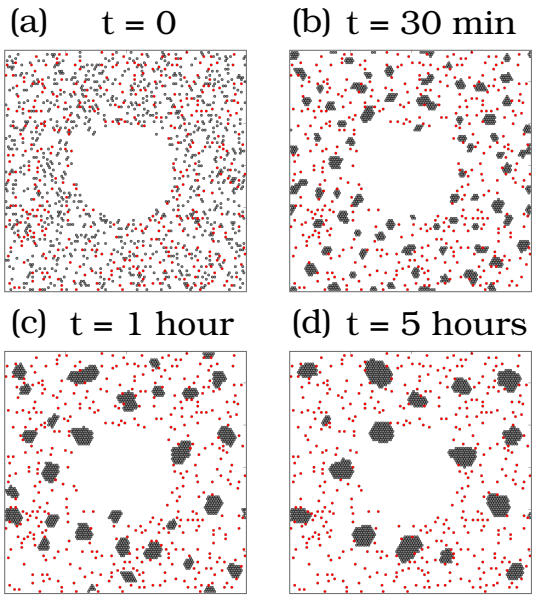

Figure 4.6: Simulation snapshots depicting the aggregation process in the absence of active cytoskeleton forces. Color coding as in Fig. 4.4. The type A points form microclusters that, on time scales of hours, barely grow and do not exhibit a drift toward the central area.

is the evolution of the system over durations of minutes and hours, the actin retrograde flow force has been calibrated to produce correctly the centripetal velocity of small clusters on these temporal scales (see detailed discussion in section 4.2.4). The consequence of this choice is that the velocity of the individual TCR-pMHC bonds turns out to be too high. A reasonable estimation for the centripetal velocity of individual bonds at the periphery of the system is $20 < v < 100$ nm/sec, i.e., higher than the velocity of a single small microcluster but lower than the actin retrograde flow velocity. The accumulation time of bonds moving at such speeds is 0.5-2 minutes, which is still more than an order of magnitude smaller than the IS formation time. The comparison between the results of Fig. 4.7 from simulations that miss the membrane-mediated attraction and Fig. 4.4 highlights two important aspects of membrane elasticity: First, it facilitates early microcluster formation that play a vital role in T cell activation. Second, it leads to coarsening dynamics that results in a decrease in the mobility of the clusters and, thereby, regulates the duration of the aggregation process.

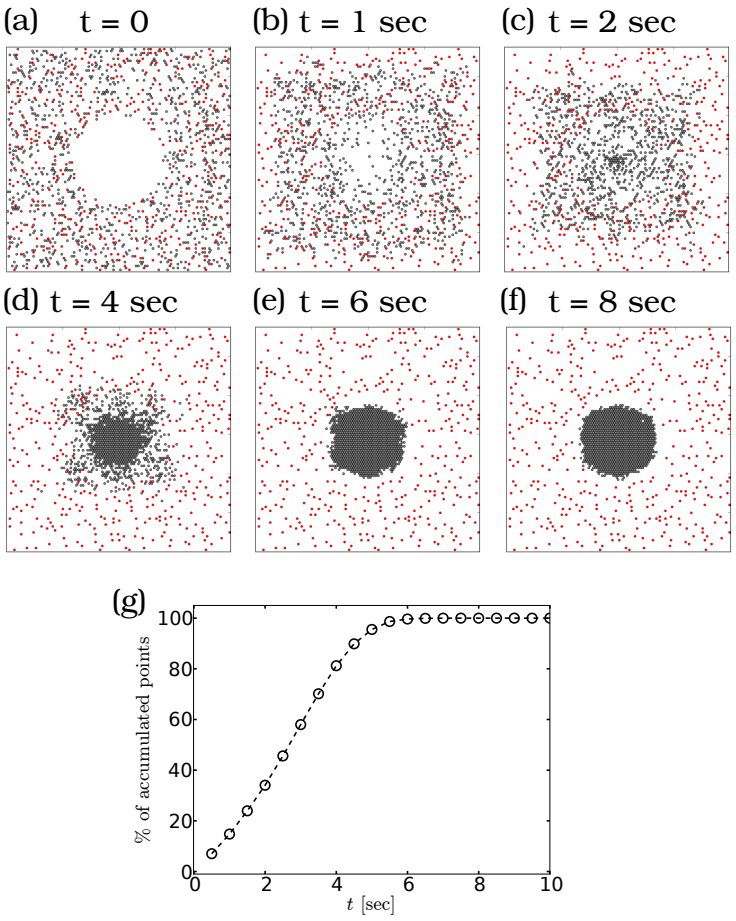

Figure 4.7: Simulation snapshots depicting the aggregation process in the absence of membrane-mediated attraction. (a-f) The type A points do not form microclusters, and accumulate at the central area within a few seconds. Color coding as in Fig. 4.4. (g) The percentage of type A bonds located at the central actin-depleted area as a function of time.

4.4 Summary

The formation of the immunological synapse (IS) is a complex biological process involving multiple molecular components, including several adhesion proteins, motor proteins, the actin cytoskeleton, and the membranes of both the T cell and the antigen-presenting cell. Adhesion between the two cell membranes is established by two types of receptor-ligand bonds, namely, TCR-pMHC and LFA1-ICAM1. At the onset of the process, the T cell's cytoskeleton remodels and an actin-depleted region is formed at the center of the contact area between the cells. Within several tens of minutes, the adhesion bonds segregate such that the TCR-pMHC bonds aggregate into a quasi-circular domain located at the actin-depleted region. The macroscopic time evolution of such a complex system can be only

addressed through coarse-grained models employing simplified molecular representation and focusing on the most dominant biophysical mechanisms. In this chapter, we present a minimal computational lattice model aiming to study the dynamics of the TCR-pMHC bonds (represented as lattice points). The model takes into account several forces that emerge in the literature as key factors in TCR-pMHC localization. One is a passive thermodynamic force associated with the membrane curvature energy, which induces attraction between the TCR-pMHC bonds, and provides repulsion between the TCR-pMHC bonds and the proteins connecting the actin cytoskeleton to the membrane. The others are centripetal forces exerted on the TCR-pMHC bonds due to the actin retrograde flow and directed transport by dynein motors along microtubules, which constitute active (non-equilibrium) forces, since they originate from processes consuming ATP chemical energy. Only in simulations where all the driving forces are present, the signature features of the IS formation process are observed. These include microclusters formation and coarsening dynamics, their transport to the central actin-depleted area, and their aggregation into a single quasi-circular domain (the cSMAC). Moreover, the simulated system evolves at the experimentally observed rates; microclusters are formed early in the process within roughly a minute from the beginning of the process, and the final bullseye structure is formed within 15-30 minutes.

Our coarse-grained simulations provide a clear and intuitive picture for the respective roles played by active and passive forces and into the intricate interplay between them that regulates the spatio-temporal pattern formation of the IS. Membrane-mediated attraction facilitates the formation of TCR-pMHC microclusters at the periphery of the contact area. These peripheral microclusters, which initiate biological cues necessary for T cell activation, are rapidly formed and continue to grow by coarsening dynamics over a period of approximately 10 minutes. The TCR-pMHC microclusters are corralled by the membrane-cytoskeleton binding proteins of the T cell, with which they have repulsive membrane-mediated interactions. As the microclusters grow in size, the corralling effect becomes more significant and their diffusivity decreases. This inhibits their accumulation in a central quasi-circular domain, despite the fact that this configuration constitutes the equilibrium state of the system. What speeds up the dynamics of the microclusters and directs their movement toward the center of the contact area is a centripetal active force induced by actin retrograde flow at the periphery of the synapse. This observation corroborates the

largely consensual view about the importance of actin remodeling and retrograde flow for the centripetal translocation of TCR-pMHC bonds at the IS. It is, however, important to emphasize that in simulations without membrane-mediated attraction, a central domain forms very rapidly without exhibiting intermediate microclusters. This observation highlights the, rather overlooked, important role played by the membrane-mediated interactions in regulating the rate of the IS formation process. This novel conclusion drawn from our model and simulations has not been addressed experimentally thus far. A possible setup by which it can be tested is a model system consisting of all the molecular ingredients of the system, except for the LFA1-ICAM1 bonds. This would shut down the membrane-mediated interactions whose origin is the mismatch in bond length between the TCR-pMHC and the LFA1-ICAM1 bonds.

At the central actin-depleted region, a centripetal force (of magnitude similar to the actin retrograde flow induced force) is effectively generated by dynein motors that walk toward the minus-end of the microtubules. An interesting observation from our simulations is the formation of a ring-shaped domain at the edge of the actin-depleted region in simulations where this force is turned off. This result is in line with a recent study, in which similar structures were observed when dynein activity was genetically impaired, but actin retrograde flow was maintained. The inability of the system to produce a central circular domain in the absence of dynein activity highlights the role played by these motors at the final stage of the process, where they enable the TCR microclusters to enter the actin-depleted region. Furthermore, the agreement between our simulation results and the experimental data supports the notion presented here of considering two different concentric regions for the active forces, namely a central area dominated by the dynein motors, and a more distant one where the actin retrograde flow is the main origin of the centripetal movement of TCR microclusters.

Chapter 5

Conclusion

Cellular adhesion is mediated through specific receptor-ligand bonds and constitutes a vital feature of biological systems. The formation of macroscopic adhesion domains that attach the plasma membrane to the extracellular matrix and/or other neighboring cell membranes not only provides mechanical stability to the cell, but is also involved in promoting important biological cues and in regulating inter-cellular communication. Gaining a thorough understanding of the biophysical principles driving the aggregation process not only provides insights into the biological mechanisms of life, but is also important for the development of biosensing applications and the design of drug delivery systems that rely on efficient adhesion between the carrier and the target plasma membrane.

This thesis aimed to develop a better theoretical understanding of membrane-mediated mechanisms for protein clustering. Membrane thermal fluctuations and elastic curvature energy effectively induce attractive forces between adhesion bonds. These forces originate from the decrease in the system's free energy upon aggregation, which enhances the thermal fluctuations (and, therefore, the configurational entropy) of the membrane, and reduces its bending energy. These two thermodynamic mechanisms have been studied in two distinct regimes of the elasticity theory for lipid bilayers. In the Helfrich regime, where the membrane undulations are strong, the thermal fluctuations induce a long-range potential of mean force (PMF) between adhesion bonds. In contrast, in the van der Waals regime, where thermal fluctuations are small, the membrane curvature deformations induce a finite-range PMF.

The most challenging aspect of the analysis of adhesion domains formation is the

many-body nature of the membrane-mediated PMF. In this work, we used an arsenal of theoretical methods, including computer simulations, statistical-mechanical calculations, and novel mean-field theories to study the condensation transition of adhesion bonds, and to elucidate the role played by membrane-mediated interactions in this process. We analyzed the aggregation behavior in both the Helfrich and van der Waals regimes of strong and weak thermal fluctuations, respectively. The former is discussed in chapter 2, where we present results of computer simulations of a coarse-grained solvent-free model for supported lipid bilayers. The results for non-constrained membranes were found to be in excellent agreement with the recently proposed Weil-Farago (WF) lattice model. The WF model is based on the notion that the local suppression of membrane thermal undulations is mainly determined by the distance from the nearest adhesion point and can, therefore, be determined from the Voronoi diagram corresponding to a given distribution of adhesion points. Our molecular simulations results are in line with the conclusion emerging from lattice simulations of the WF model, that thermal fluctuations alone are insufficient to promote cluster formation, yet they have a considerable impact on the condensation transition. We arrive at this conclusion by comparing simulations of supported membranes with those of non-fluctuating flat membranes subjected to a strong physical confinement. In the latter case, the fluctuation-induced interactions vanish; condensation may be induced by residual direct interactions (if sufficiently strong), and the system can be described by the standard nearest-neighbor lattice-gas (Ising) model for gas-liquid phase transitions. In the case of non-confined membranes, our simulations demonstrate that the system remains in the Ising universality class. However, the membrane-mediated interactions effectively reduce the thermodynamic temperature by a factor of 2-3; i.e., they compensate for roughly half of the mixing entropy lost upon condensation. This picture is consistent with the idea that in a distribution of adhesion bonds, the long-range attractive PMF arising from the membrane-thermal fluctuations is self-screened. We also performed simulations of membranes subjected to negative surface tension that presumably enhances the thermal roughness of the membrane. We found that the negative tension had no effect on the gas phase, where the scattered adhesion bonds strongly suppress the thermal undulations. The influence of the negative tension is seen in the condensed phase, where the membranes exhibit buckling instabilities and elongated adhesion domains (stripes) are formed in the non-buckled portion of the system.

In chapter 3, we examine the condensation transition in the van der Waals regime. As opposed to the entropic attraction between adhesion bonds in the Helfrich regime, the curvature-induced pair PMF in the van der Waals regime decays over a characteristic correlation length of $\xi_\gamma \simeq 50 - 100\,\mathrm{nm}$. This feature of the pair PMF implies that the condensation transition is expected to be of the lattice-gas (Ising) universality class. Our investigation of the curvature-mediated many-body PMF and the condensation transition are based on a novel mean-field approach involving numerical evaluation of the membrane's elastic energy for random distributions of adhesion bonds on a triangular lattice. We found that the elastic deformation energy per adhesion bond in systems with different healing lengths ξ_γ and bond densities ϕ exhibits data collapse when plotted against the scaled density $x = \xi_\gamma^2 \phi$. This enabled us to obtain an empirical expression for the system energy, which is then used in a mean-field expression for the system's free energy. From the mean-field free energy, we obtain the phase diagram of the system and identify the two-phase coexistence region. The most important aspects of the phase diagram are the observations that: (i) the critical point x_c lies in regions where x attains extremely small values, and (ii) the binodal/spinodal curves sharply decline with the deformation length, h_0, imposed by a single bond for $x_c < x \lesssim 1$. The parameter h_0 serves in the problem as a temperature variable. When assigning parameter values to the model that are characteristic of biological membranes, we show that biological adhesion domains may, in some cases, be associated with the two-phase region of the phase diagram. Specifically, the adhesion domains constitute a semi-dilute phase coexisting with an extremely dilute phase that is essentially empty of bonds. The densities in the semi-dilute domains are such that the adhesion bonds are typically separated by a distance ξ_γ from each other. The formation of highly packed condensed domains requires much stronger deformations (h_0), that are often (but not always) unrealistically large. This can be understood from the observation that for an adhesion bond density of $\phi \simeq \xi_\gamma^{-2}$, the membrane is relatively flat and, therefore, the curvature-mediated attraction effectively saturates at these densities.

In chapter 4, we take a closer look at a specific biological example of an adhesion domains, which is the immunological synapse (IS) that forms upon contact between T cells and antigen-presenting cells. This specialized cellular junction is established by two types of receptor-ligand complexes namely, TCR-pMHC and LFA1-ICAM1 adhesion bonds, which

form a unique concentric pattern where the TCR-pMHC bonds are clustered in the center of the contact area, while the LFA1-ICAM1 bonds accumulate at the periphery. This segregation process can be partially attributed to the marked mismatch in bond lengths between the two types of adhesion bonds, which results in substantial membrane deformations leading to curvature-induced interactions. For the system parameters characterizing the IS, our mean-field theory (developed in chapter 3) predicts the formation of a semi-dilute TCR-pMHC domain with a bond density of $\phi \simeq \xi_\gamma^{-2} \sim 100\,\mu\mathrm{m}^2$ that is comparable with their densities in the IS. Nevertheless, domain formation purely driven by a *spontaneous* phase separation mechanism cannot account for the concentric geometric pattern characteristic of the IS. Indeed, *active* cytoskeleton processes stemming form actin polymerization/depolymerization events and dynein motor activity are thought to be indispensable for this special molecular arrangement. The peripheral actin retrograde flow and the more centrally located directed transport of TCRs by dyneins generate additional centripetal forces, which are believed to be responsible for the broken symmetry in the system. In order to investigate these issues, we developed an implicit-membrane 2D lattice model for TCR-pMHC aggregation in the IS. In this model, the elasticity-induced many-body PMF in the van der Waals regime is approximated by nearest-neighbor pair interactions. This approximation holds for semi-dilute systems like the IS. The active cytoskeleton forces are modeled by an effective centripetal potential. The spatio-temporal evolution of the system is studied using Monte Carlo simulations, and the relationship between the Monte Carlo and the physical time units is established from the diffusion coefficient of TCR proteins. The simulated aggregation process exhibits a very good agreement with numerous experimental observations, and correctly captures the signature features of IS formation. The process begins with the nucleation of small peripheral TCR-pMHC microclusters. Over time, the microclusters grow by coarsening dynamics, and exhibit centripetal motion towards the center of the system. Apart from the agreement on the stages and the spatial evolution of the system, the simulations also show that the central domain is formed within $\sim$30 min, which is indeed the experimentally observed timescale for IS formation.

Consistent with previous findings, our lattice simulations point to the great importance of active cytoskeleton forces, which drive the TCR-pMHC centripetally and allow their aggregation to be completed over biologically relevant timescales. Our results also highlight

the rather overlooked importance of membrane-mediated interactions in T cell activation. The central accumulation of TCR-pMHC in simulations lacking these interactions occurs too rapidly and does not exhibit the formation of peripheral microclusters, which are only observed in systems where the curvature-induced attraction is enabled. The formation of microclusters decreases the mobility of TCR-pMHC bonds and slows down their centripetal movement. This provides T cells with an appropriate time window to allow biological signaling via peripheral TCR microclusters, which is vital for a proper immune response. Thus, our lattice model and Monte Carlo simulations shed light on the respective roles of passive and active mechanisms in IS formation, and the delicate interplay between them that regulates the spatio-temporal evolution of the process.

The present work provides a comprehensive biophysical basis for the understanding of adhesion domain formation driven under the influence of membrane-mediated interactions. The concepts and methods developed here can be applied to the study of other biological systems exhibiting membrane adhesion clusters. In the example of the IS, we focused on the formation of semi-dilute adhesion domains; however, it is important to note that our mean-field treatment suggests that densely packed clusters can, in principle, also form in membranes subjected to strong deformations. One should keep in mind that our analysis is based on a linear theory, where the membrane is represented in the Monge gauge using the small gradient approximation. This approximation may not hold in the case of strongly deformed membranes, which calls for further theoretical studies. Such investigations are especially interesting in light of recent evidence suggesting that curvature-mediated mechanisms may be responsible for integrin clustering in cancerous cells [117]. Strong membrane deformations caused by large glycoproteins, which are commonly overexpressed in malignant cells and can extend up to 200 nm away from the membrane's surface [118, 119], were found to facilitate integrin clustering, unlike short (3 nm long) glycoproteins. The formation of focal adhesion domains in tumor cells enhances metastatic capabilities and promotes cellular growth and survival, which points to an interesting mechanical role of the glycocalyx in cellular signaling. Interestingly, our mean-field phase diagram predicts that for a membrane deformation of $h_0 \gtrsim 100$ nm (which is much larger than the typical thermal roughness), the condensed phase is characterized by a scaled density of $x \gtrsim 10$, corresponding roughly to densities of the order of $\gtrsim 1000$ bonds per μm^2, which are comparable to the typical integrin

density in focal adhesion [120]. We hope that the present work will stimulate further biophysical research that will deepen our understating of nature's ability to exploit the physical properties of membranes to execute biological functions.

Appendix A

With the Helfrich Hamiltonian in the van der Waals regime (1.20), the membrane's height-height correlations in the absence of adhesion bonds are given by

$$\langle h(\mathbf{r})h(\mathbf{r\prime})\rangle = \left(\frac{l}{L}\right)^4 \sum_{\mathbf{q}} \langle |h_{\mathbf{q}}^2| \rangle e^{-i\mathbf{q}\cdot(\mathbf{r}-\mathbf{r\prime})} \approx -\frac{4}{\pi}\Delta^2 \mathrm{kei}\left(\frac{|\mathbf{r}-\mathbf{r\prime}|}{\xi_\gamma}\right), \tag{A.1}$$

For very small distances ($\mathbf{r} \to \mathbf{r\prime}$), eq. (A.1) reduces to the thermal roughness Δ^2 given by eq. (1.23). Let us now look at a collection of N height variables at different positions $\{\mathbf{r}_i\}_{i=1}^N$ creating the vector $\mathbf{h} = [h(\mathbf{r}_1), \ldots, h(\mathbf{r}_N)]^{\mathrm{T}}$. The vector $\mathbf{h}$ is $N-$variate Gaussian distributed, with a probability density function

$$p(\mathbf{h}) = \frac{1}{(2\pi)^{N/2}\sqrt{\det \mathrm{C}}} \exp\left(-\frac{1}{2}\mathbf{h}^{\mathrm{T}}\mathrm{C}^{-1}\mathbf{h}\right), \tag{A.2}$$

where $\mathrm{C}_{ij} = \langle h(\mathbf{r}_i)h(\mathbf{r}_j)\rangle$ is the covariance matrix of $\mathbf{h}$ according to eq. (A.1). To describe a membrane locally fixed by N points at $\{\mathbf{r}_i\}_{i=1}^N$ to a height h_0, one could calculate the probability density $p\left(\mathbf{h} = h_0\left[1, \ldots, 1\right]^{\mathrm{T}} = \mathbf{h}_0\right)$ that a *free* membrane attains such a configuration,

$$\begin{aligned} p(\mathbf{h} = \mathbf{h}_0) &= \frac{1}{(2\pi)^{N/2}\sqrt{\det \mathrm{C}}} \exp\left(-\frac{h_0^2}{2}\sum_{i,j=1}^{N} \mathrm{C}_{ij}^{-1}\right) \\ &= \frac{1}{(2\pi\Delta^2)^{N/2}\sqrt{\det \mathrm{M}}} \exp\left\{-\frac{1}{2}\left(\frac{h_0}{\Delta}\right)^2 \sum_{i,j=1}^{N} \mathrm{M}_{ij}^{-1}\right\}, \end{aligned} \tag{A.3}$$

where we have introduced the matrix M that satisfies $\mathrm{C} = \Delta^2\mathrm{M}$. Eq. (A.3) exactly equals the ratio between the partition functions of the attached and the unbound membranes Z_N/Z_0, which is reconciled with eq. (1.35) for Z_N. For dilute distributions of attachments points,

where the typical distance between them $|\mathbf{r} - \mathbf{r\prime}| \gg \xi_\gamma$, the matrix M can be approximated by

$$\mathrm{M}_{ij} \approx 1 + \eta_{ij}, \tag{A.4}$$

with $\eta_{ii} = 0$ and $\eta_{i \neq j} = -\frac{4}{\pi}\mathrm{kei}\left(|\mathbf{r}_i - \mathbf{r}_j| / \xi_\gamma\right) \ll 1$. The inverse matrix M^{-1} can be approximated by $\mathrm{M}^{-1}_{ij} \approx 1 - \eta_{ij}$, and the partition function Z_N reads

$$Z_N \approx \exp\left\{-\frac{1}{2}\left(\frac{h_0}{\Delta}\right)^2 \left(N - \sum_{i \neq j} \eta_{ij}\right)\right\}. \tag{A.5}$$

This form of the partition function Z_N is isomorphic to that of a lattice-gas model in the canonical ensemble, with short-range interactions of range $\sim \xi_\gamma$. Thus in the dilute limit, the many-body nature of the membrane-mediated PMF between the adhesion bonds is eliminated and, instead, the PMF can be described as a simple sum of pairwise interactions. If the lattice spacing of the discrete model is set to $\geq \xi_\gamma$, the interactions can be limited to nearest-neighbor sites.

Bibliography

[1] G. M. Cooper, *The Cell* (Sinauer Associates, Massachusetts, 2000).

[2] B. Alberts, D. Bray, J. Lewis, M. Raff, K. Roberts, and J. D. Watson, *Molecular Biology of the Cell* (Garland, New York, 1994).

[3] G. L. Nicolson, The Fluid-Mosaic Model of Membrane Structure: Still relevant to understanding the structure, function and dynamics of biological membranes after more than 40 years. *Biochim. Biophys. Acta* **1838**, 1451 (2014).

[4] A. Kusumi, Y. Sako and M. Yamamoto, Confined lateral diffusion of membrane receptors as studied by single particle tracking (nanovid microscopy). Effects of calcium-induced differentiation in cultured epithelial cells. *Biophys. J.* **65**, 2021 (1993).

[5] A. J. Ridley *et al.*, Cell migration: integrating signals from front to back. *Science* **302**, 1704 (2003).

[6] J. M. Halbleib and W. J. Nelson, Cadherins in development: cell adhesion, sorting, and tissue morphogenesis. *Genes Dev.* **20**, 3199 (2006).

[7] S. J. Singer, Intercellular communication and cell-cell adhesion. *Science* **255**, 1671 (1992).

[8] T. A. Springer, Adhesion receptors of the immune system. *Nature* **346**, 425 (1990).

[9] N. M. Kumar and N. B. Gilula, The gap junction communication channel. *Cell* **3**, 381 (1996).

[10] M. A. Schwartz, Integrins and extracellular matrix in mechanotransduction. *Cold Spring Harb. Perspect. Biol.* **2**, a005066 (2010).

[11] K. Burridge and M. Chrzanowska-Wodnicka, Focal adhesions, contractility, and signaling. *Annu. Rev. Cell Dev. Biol.* **12**, 463 (1996).

[12] K. Burridge et al., Focal adhesions: transmembrane junctions between the extracellular matrix and the cytoskeleton. *Annu. Rev. Cell Dev. Biol.* **4**, 487 (1988).

[13] M. A. Wozniak, K. Modzelewska, L. Kwong and P. J. Keely, Focal adhesion regulation of cell behavior. *Biochim. Biophys. Acta* **1692**, 103 (2004).

[14] F. G. Giancotti and E. Ruoslahti, Integrin signaling. *Science* **285**, 1028 (1999).

[15] A. S. Yap, W. M. Brieher and B. M. Gumbiner, Molecular and functional analysis of cadherin-based adherens junctions. *Annu. Rev. Cell Dev. Biol.* **13**, 119 (1997).

[16] B. M. Gumbiner, Regulation of cadherin-mediated adhesion in morphogenesis. *Nat. Rev. Mol. Cell Biol.* **6**, 622 (2005).

[17] J. T. Groves, L. K. Mahal and C. R. Bertozzi, Control of cell adhesion and growth with micropatterned supported lipid membranes. *Langmuir* **17**, 5129 (2001).

[18] M. Tanaka and E. Sackmann, Polymer-supported membranes as models of the cell surface. *Nature* **437**, 656 (2005).

[19] A. S. Smith and U. Seifert, Vesicles as a model for controlled (de-) adhesion of cells: a thermodynamic approach. *Soft Matter* **3**, 275 (2007).

[20] A. S. Smith and E. Sackmann, Progress in mimetic studies of cell adhesion and the mechanosensing. *Chem. Phys. Chem.* **10**, 66 (2009).

[21] A. Kloboucek, A. Behrisch, J. Faix and E. Sackmannn, Adhesion-induced receptor segregation and adhesion plaque formation: a model membrane study. *Biophys. J.* **77**, 2311 (1999).

[22] A. S. Smith, B. G. Lorz, U. Seifert and E. Sackmann, Antagonist-induced deadhesion of specifically adhered vesicles. *Biophys. J.* **90**, 1064 (2006).

[23] M. Tanaka and E. Sackmann, Supported membranes as biofunctional interfaces and smart biosensor platforms. *Phys. Stat. Sol. (a)* **203**, 3452 (2006).

[24] W. Helfrich, Elastic properties of lipid bilayers: theory and possible experiments. *Z. Naturforsch. C.* **28**, 693 (1973).

[25] J. F. Faucon, M. D. Mitov, P. Méléard, I. Bivas and P. Bothorel, Bending elasticity and thermal fluctuations of lipid membranes. Theoretical and experimental requirements. *J. Phys. France* **50**, 2389 (1989).

[26] G. Khelashvili, B. Kollmitzer, P. Heftberger, G. Pabst and D. Harries, Calculating the bending modulus for multicomponent lipid membranes in different thermodynamic phases. *J. Chem. Theory Comput.* **9**, 3866 (2013).

[27] N. Mohandas and E. Evans, Mechanical properties of the red cell embrane in relation to Molecular structure and genetic defects. *Annu. Rev. Biophys. Biomol. Struct.* **23**, 787 (1994).

[28] J. N. Israelachvili, *Intermolecular and Surface Forces* (Academic Press, San Diego, 1992).

[29] B. Geiger, J. P. Spatz and A. D. Bershadsky, Environmental sensing through focal adhesions. *Nat. Rev. Mol. Cell Biol.* **10**, 21 (2009).

[30] R. Bruinsma and P. Pincus, Protein aggregation in membranes. *Curr. Opin. Solid St. M.* **1**, 401 (1996).

[31] O. Farago, in *Advances in Planar Lipid Bilayers and Liposomes*, **14** Chap. 5, pp. 129-155, edited by. A. Iglič (Elsevier 2011).

[32] B. Różycki, R. Lipowsky, and T. R. Weikl, Segregation of receptorligand complexes in cell adhesion zones: phase diagrams and the role of thermal membrane roughness. *New J. Phys.* **12**, 095003 (2010).

[33] M. Goulian, R. Bruinsma and P.A. Pincus, Long-range forces in heterogeneous fluid membranes. *Europhys. Lett.* **22**, 145 (1993).

[34] T. R. Weikl, M. M. Kozlov and W. Helfrich, Interaction of conical membrane inclusions: Effect of lateral tension. *Phys. Rev. E* **57**, 6988 (1998).

[35] P. G. Dommersnes, J. B. Fournier and P. Galatola, Long-range elastic forces between membrane inclusions in spherical vesicles. *Europhys. Lett.* **42**, 233 (1998).

[36] M. Kardar and R. Golestanian, The "friction" of vacuum, and other fluctuation-induced forces. *Rev. Mod. Phys.* **71**, 1233 (1999).

[37] R. Golestanian, M. Goulian and M. Kardar, Fluctuation-induced interactions between rods on a membrane. *Phys. Rev. E* **54**, 6725 (1996).

[38] R. Bruinsma, M. Goulian and P. Pincus, Self-assembly of membrane junctions. *Biophys. J.* **67**, 746 (1994).

[39] J. O. Rädler, T. J. Feder, H. H. Strey and E. Sackmann, Fluctuation analysis of tension-controlled undulation and solid substrates. *Phys. Rev. E* **51**, 4526 (1995).

[40] O. Farago, Membrane fluctuations near a plane rigid surface. *Phys. Rev. E* **78**, 051919 (2008).

[41] W. Helfrich, Steric interaction of fluid membranes in multilayer systems. *Z. Naturforsch. A* **33a**, 305 (1978).

[42] O. Farago, Fluctuation-induced attraction between adhesion sites of supported membranes. *Phys. Rev. E* **81**, 050902(R) (2010).

[43] R. Lipowsky, Adhesion of membranes via anchored stickers. *Phys. Rev. Lett.* **77**, 1652 (1996).

[44] T. R. Weikl and R. Lipowsky, Adhesion-induced phase behavior of multicomponent membranes. *Phys. Rev. E* **64**, 011903 (2001).

[45] T. Speck and R. L. C. Vink, Random pinning limits the size of membrane adhesion domains. *Phys. Rev. E* **86**, 031923 (2012).

[46] N. Weil and O. Farago, Entropy-driven aggregation of adhesion sites of supported membranes. *Eur. Phys. J. E* **33**, 81 (2010).

[47] H. Noguchi, Entropy-driven aggregation in multilamellar membranes. *Europhys. Lett.* **102**, 68001 (2013).

[48] M. Abramowitz and I. A. Stegun, *Handbook of Mathematical Functions: with formulas, graphs, and mathematical tables* (Dover, New York, 1972).

[49] T. Bihr, U. Seifert and A. S. Smith, Multiscale approaches to protein-mediated interactions between membranesrelating microscopic and macroscopic dynamics in radially growing adhesions. *New J. Phys.* **18**, 083016 (2015).

[50] T. Speck, E. Reister and U. Seifert, Specific adhesion of membranes: Mapping to an effective bond lattice gas. *Phys. Rev. E* **82**, 021923 (2010).

[51] D. Schmidt, T. Bihr, U. Seifert and A.S. Smith, Coexistence of dilute and densely packed domains of ligand-receptor bonds in membrane adhesion. *Europhys. Lett.* **99**, 38003 (2012).

[52] F. L. H. Brown, Elastic modeling of biomembranes and lipid bilayers. *Ann Rev. Phys. Chem.* **59**, 685 (2008).

[53] E. Lindahl and O. Edholm, Mesoscopic undulations and thickness fluctuations in lipid bilayers from molecular dynamics simulations. *Biophys. J.* **79**, 426 (2000).

[54] Z. A. Levine *et al.*, Determination of biomembrane bending moduli in fully atomistic simulations. *J. Am. Chem. Soc.* **136**, 13582 (2014).

[55] F. Schmid, D. Düchs, O. Lenz and B. West, A generic model for lipid monolayers, bilayers, and membranes. *Comp. Phys. Comm.* **177**, 168 (2007).

[56] S. J. Marrink, A. H. de Vries and A. E. Mark, Coarse grained model for semiquantitative lipid simulations. *J. Phys. Chem. B* **108**, 750 (2004).

[57] S. J. Marrink, H. J. Risselada, S. Yefimov, D. P. Tieleman and A. H. de Vries, The MARTINI force field: coarse grained model for biomolecular simulations. *J. Phys. Chem. B* **111**, 7812 (2007).

[58] M. Venturoli, B. Smit, and M. M. Sperotto, Simulation studies of protein-induced bilayer deformations, and lipid-induced protein tilting, on a mesoscopic model for lipid bilayers with embedded proteins. *Biophys. J.* **88**, 1778 (2005).

[59] O. Farago, "Water-free" computer model for fluid bilayer membranes. *J. Chem. Phys.* **119**, 596 (2003).

[60] J. M. Drouffe, A. C. Maggs and S. Leibler, Computer simulations of self-assembled membranes. *Science* **254**, 1353 (1991).

[61] I. R. Cooke and M. Deserno, Solvent-free model for self-assembling fluid bilayer membranes: stabilization of the fluid phase based on broad attractive tail potentials. *J. Chem. Phys.* **123**, 224710 (2005). M. Deserno, Mesoscopic membrane physics: concepts, simulations, and selected applications. *Macromol. Rapid Commun.* **30**, 752 (2009).

[62] Metropolis N., Rosenbluth A. W. , Rosenbluth M. N., Teller A. H. and Teller E. Equation of state calculations by fast computing machines. *J. Chem. Phys.* **21**, 1087 (1953).

[63] O. Farago, Mode excitation Monte Carlo simulations of mesoscopically large membranes. *J. Chem. Phys.* **128**, 184105 (2008).

[64] B. I. Halperin and D. R. Nelson, Theory of two-dimensional melting. *Phys. Rev. Lett.* **41**, 121 (1978).

[65] N. Dharan and O. Farago, Coarse-grained molecular simulations of membrane adhesion domains. *J. Chem. Phys.* **141**, 024903 (2014).

[66] O. Farago and N. Grønbech-Jensen, Computational and analytical modeling of cationic lipid-DNA complexes. *Biophys. J.* **92**, 3228 (2007).

[67] H. Noguchi, Anisotropic surface tension of buckled fluid membranes. *Phys. Rev. E* **83**, 061919 (2011).

[68] W. K. den Otter, Area compressibility and buckling of amphiphilic bilayers in molecular dynamics simulations. *J. Chem. Phys.* **123**, 214906 (2005).

[69] Y. Y. Avital and O. Farago, Small membranes under negative surface tension. *J. Chem. Phys.* **142**, 124902 (2015).

[70] M. Staykova, M. Arroyo, M. Rahimi, and H. A. Stone, Confined bilayers passively regulate shape and stress. *Phys. Rev. Lett.* **110**, 028101 (2013).

[71] O. Farago, Fluctuation-induced attraction between adhesion sites of supported membranes. *Phys. Rev. E* **81**, 050902R (2010).

[72] N. Grønbech-Jensen and O. Farago, A simple and effective Verlet-type algorithm for simulating Langevin dynamics. *Mol. Phys.* **111**, 983 (2013).

[73] A. Grakoui *et al.*, The immunological synapse: a molecular machine controlling T cell activation. *Science* **285**, 221 (1999).

[74] S. K. Bromley *et al.*, The immunological synapse. *Annu. Rev. Immunol.* **19**, 375 (2001).

[75] D. Coombs, M. Dembo, C. Wofsy and B. Goldstein, Equilibrium thermodynamics of cell-cell adhesion mediated by multiple ligand-receptor pairs. *Biophys. J.* **86**, 1408 (2004).

[76] S. J. E. Lee, Y. Hori, J. T. Groves, M. L. Dustin and A. K. Chakraborty, Correlation of a dynamic model for immunological synapse formation with effector functions: two pathways to synapse formation. *Trends Immunol* **23**, 492 (2002).

[77] A. K. Chattopadhyay and N. J. Burroughs, Close contact fluctuations: the seeding of signalling domains in the immunological synapse. *Europhys. Lett.* **77**, 48003 (2007).

[78] A. Carlson and L. Mahadevan, Elastohydrodynamics and kinetics of protein patterning in the immunological synapse. *PLoS Comput. Biol.* **11**, e1004481 (2015).

[79] N. J. Burroughs and C. Wülfing, Differential segregation in a cell-cell contact interface: the dynamics of the immunological synapse. *Biophys. J.* **83**, 1784 (2002).

[80] T. R. Weikl, M. Asfaw, H. Krobath, B. Różycki and R. Lipowsky, Adhesion of membranes via receptorligand complexes: Domain formation, binding cooperativity, and active processes. *Soft Matter* **5**, 3213 (2009).

[81] J. B. Huppa and M. M. Davis, T-cell-antigen recognition and the immunological synapse. *Nat. Rev. Immunol.* **3**, 973 (2003).

[82] K. G. Johnson, S. K. Bromley, M. L. Dustin and M. L. Thomas, A supramolecular basis for CD45 tyrosine phosphatase regulation in sustained T cell activation. *Proc. Natl. Acad. Sci. U. S. A.* **97**, 10138 (2000).

[83] C. R. F. Monks, B. A. Freiberg, H. Kupfer, N. Sciaky and A. Kupfer, Three-dimensional segregation of supramolecular activation clusters in T cells. *Nature* **395**, 82 (1998).

[84] K. D. Mossman, G. Campi, J. T. Groves and M. L. Dustin, Altered TCR signaling from geometrically repatterne. *Science* **310**, 1191 (2005).

[85] J. Storim, E. B. Bröcker and P. Friedl, A dynamic immunological synapse mediates homeostatic TCR-dependent and -independent signaling. *Eur. J. Immunol.* **40**, 2741 (2010).

[86] G. M. Griffiths, A. Tsun and J. C .Stinchcombe, The immunological synapse: a focal point for endocytosis and exocytosis. *J. Cell Biol.* **189**, 399 (2010).

[87] M. L. Dustin and J. A. Cooper, The immunological synapse and the actin cytoskeleton: molecular hardware for T cell signaling. *Nat. Immunol.* **1**, 23 (2000).

[88] A. T. Ritter et al., Actin depletion initiates events leading to granule secretion at the immunological synapse. *Immunity* **42**, 864 (2015).

[89] J. Yi, X. S. Wu, T. Crites and J. A. Hammer III, Actin retrograde flow and actomyosin II arc contraction drive receptor cluster dynamics at the immunological synapse in Jurkat T cells. *Mol. Biol. Cell* **23**, 834 (2012).

[90] A. Babich et al., F-actin polymerization and retrograde flow drive sustained PLCγ1 signaling during T cell activation. *J. Cell Biol.* **197**, 775 (2012).

[91] Y. Kaizuka, A. D. Douglass, R. Varma, M. L. Dustin and R. D. Vale, Mechanisms for segregating T cell receptor and adhesion molecules during immunological synapse formation in Jurkat T cells. *Proc. Natl. Acad. Sci. U. S. A.* **104**, 20296 (2007).

[92] C. H. Yu, H. J. Wu, Y. Kaizuka Y. R. D. Vale and J. T. Groves, Altered actin centripetal retrograde flow in physically restricted immunological synapses. *PLoS ONE* **5**, e11878 (2010).

[93] I. Tskvitaria-Fuller, A L. Rozelle, H. L. Yin and C. Wülfing, Regulation of sustained actin dynamics by the TCR and costimulation as a mechanism of receptor localization. *J. Immunol.* **171**, 2287 (2003).

[94] N. C. Hartman, J. A. Nye and J. T. Groves, Cluster size regulates protein sorting in the immunological synapse. *Proc. Natl. Acad. Sci. U. S. A.* **106**, 12729 (2009).

[95] T. Schnyder et al., B cell receptor-mediated antigen gathering requires ubiquitin ligase Cbl and adaptors Grb2 and Dok-3 to recruit dynein to the signaling microcluster. *Immunity* **34**, 905 (2011).

[96] A. Hashimoto-Tane et al., Dynein-driven transport of T cell receptor microclusters regulates immune synapse formation and T cell activation. *Immunity* **34**, 919 (2011).

[97] S. Y. Qi, J. T. Groves and A. K. Chakraborty, Synaptic pattern formation during cellular recognition. *Proc. Natl. Acad. Sci. U. S. A.* **98**, 6548 (2001).

[98] M. T. Figge and M. Meyer-Hermann, Modeling receptor-ligand binding kinetics in immunological synapse formation. *Eur. Phys. J. D* **51**, 153 (2009).

[99] H. Krobath, B. Różycki, R. Lipowsky and T. R. Weikl, Binding cooperativity of membrane adhesion receptors. *Soft Matter* **5**, 3354 (2009).

[100] N. Dharan and O. Farago, Formation of semi-dilute adhesion domains driven by weak elasticity-mediated interactions. *Soft Matter* **12**, 6649 (2016).

[101] T. R. Weikl and R. Lipowsky, Pattern formation during T-cell adhesion. *Biophys. J.* **87**, 3665 (2004).

[102] A. S. Shaw, FERMing up the synapse. *Immunity* **15**, 683 (2001).

[103] C. M. Johnson and W. Rodgers, Spatial segregation of phosphatidylinositol 4,5-bisphosphate (PIP_2) signaling in immune cell functions. *Immunol. Endocr. Metab. Agents Med. Chem.* **8**, 349 (2008).

[104] Y. Sun, R. D. Dandekar, Y. S. Mao, H. L. Yin and C. Wülfing, Phosphatidylinositol (4,5) bisphosphate controls T cell activation by regulating T cell rigidity and organization. *PLoS ONE* **6**, e27227 (2011).

[105] J. Gatfield, I. Albrecht, B. Zanolari, M. O. Steinmet and J. Pieters, Association of the leukocyte plasma membrane with the actin cytoskeleton through coiled coil-mediated trimeric coronin 1 molecules. *Mol. Biol. Cell* **16**, 2786 (2005).

[106] R. Varma, G. Campi, T Yokosuka, T. Saito and M. L. Dustin, T cell receptor-proximal signals are sustained in peripheral microclusters and terminated in the central supramolecular activation cluster. *Immunity* **25**, 117 (2006).

[107] E. Molnár, S. Deswal, W. W. A. Schamel, Pre-clustered TCR complexes. *FEBS Lett.* **584**, 4832 (2010).

[108] D. M. Davis and M. L. Dustin, What is the importance of the immunological synapse? *Trends Immunol.* **25**, 323 (2004).

[109] J. Gómez-Llobregat, J. Buceta and R. Reigada, Interplay of cytoskeletal activity and lipid phase stability in dynamic protein recruitment and clustering. *Sci. Rep.* **3**, 2608 (2013).

[110] A. Kusumi et al., Dynamic organizing principles of the plasma membrane that regulate signal transduction: commemorating the fortieth anniversary of Singer and Nicolson's fluid-mosaic model. *Annu Rev Cell Dev Biol* **28**, 215 (2012).

[111] B. Favier, N. J. Burroughs, L. Wedderburn and S. Valitutti, TCR dynamics on the surface of living T cells. *Int. Immunol.* **13**, 1525 (2001).

[112] S. Kumari, S. Curado, V. Mayya and M. L. Dustin, T cell antigen receptor activation and actin cytoskeleton remodeling. *Biochim. Biophys. Acta* **1838**, 546 (2014).

[113] A. L. DeMond, K. D. Mossman, T. Starr, M. L. Dustin and J. T. Groves, T cell receptor microcluster transport through molecular mazes reveals mechanism of translocation. *Biophys. J.* **94**, 3286 (2008).

[114] C. O. Mejean et al., Elastic coupling of nascent apCAM adhesions to flowing actin networks. *PLoS One* **8**, e73389 (2013).

[115] G. Campi, R. Varma, M. L. Dustin, Actin and agonist MHC-peptide complex-dependent T cell receptor microclusters as scaffolds for signaling. *J. Exp. Med* **202**, 1031 (2005).

[116] T. Yokosuka et al., Newly generated T cell receptor microclusters initiate and sustain T cell activation by recruitment of Zap70 and SLP-76. *Nat. Immunol* **6**, 1253 (2005).

[117] Paszek M. J. et al., The cancer glycocalyx mechanically primes integrin-mediated growth and survival. *Nature* **511**, 319 (2014).

[118] D. W. Kufe, Mucins in cancer: function, prognosis and therapy. *Nat. Rev. Cancer* **9**, 874 (2009).

[119] H. Vink and B. R. Duling, Identification of distinct luminal domains for macromolecules, erythrocytes, and leukocytes within mammalian capillaries. *Circ. Res.* **79**, 581 (1996).

[120] P. W. Wiseman et al., Spatial mapping of integrin interactions and dynamics during cell migration by image correlation microscopy. *J. Cell Sci.* **117**, 5521 (2004).

תקציר

ממברנות ביולוגיות מהוות חוצץ טבעי בין תוכן התא וסביבתו החיצונית, ומאפשרות מעבר דו-כיווני מבוקר של יונים, מולקולות ואותות כימיים שונים. הממברנות עשויות משכבה כפולה של מולוקלות שומן בפאזה נוזלית, ומכילות סוגים שונים של חלבונים בעלי תפקידים מגוונים. חלבוני אדהזיה הינם משפחה יחודית של חלבוני ממברנה, שיוצרים קשרים ספציפיים עם המטריקס החוץ תאי ו/או חלבונים אחרים בממברנות של תאים שכנים. במקרים רבים, קשרי האדהזיה הללו מתגבשים ליצירת צמתי אדהזיה המכילים מאות עד אלפי קשרי אדהזיה. צבירי אדהזיה אלו נחוצים לבקרה של תהליכים ביולוגיים חשובים כגון, נדידת תאים, תקשורת בין תאית, היווצרות רקמות והפעלת התגובה החיסונית. אחד המנגנונים המניעים את התעבותם של קשרי אדהזיה לכדי צבירים גדולים נובע מאינטרקציות אפקטיביות בינהם המושרות על ידי הממברנה. מקור האינטקרציות האפקטיביות האלה טמון בתנודות התרמיות של הממברנה והמעוותים האלסטיים שהיא חווה. הרווח האנטרופי המתקבל מהגדלת הפלקטואציות התרמיות כאשר קשרי האדהזיה מתקבצים, כמו גם הקטנת האנרגיה האלסטית המלווה בתהליך זה, מהווים מנגון תרמודינמי ליצירת צבירי אדהזיה. בעבודת המחקר הנוכחית, אנו משתמשים בחישובים מכנו-סטיסטיים, סימולציות מחשב מולקולריות ותאוריות שדה ממוצע חדשניות על מנת לחקור את האינטרקציות האפקטיביות בין קשרי אדהזיה המושרות על ידי הממברנה, לקבל הבנה עמוקה יותר לגבי תפקידם בתהליך היווצרות צמתי אדהזיה, ולאפיין את מעבר הפאזה להתעבות.

בכדי לחקור את המנגנון האנטרופי למשיכה בין קשרי אדהזיה, אנו מבצעים סימולציות מחשב של מודל מופשט לממברנות המצומדות למשטח בעזרת אתרי אדהזיה. תוצאות הסימולציות מראות כי הפלקטואציות התרמיות לבדן אינן חזקות דיו בכדי לגרום ליצירת צבירי אדהזיה, אך יש להן השפעה חזקה על התעבות המערכת. מסקנה זו נובעת מסימולציות של ממברנות שטוחות שאינן מסוגלות להתנודד כלל, על ידי הגבלתם בין שני משטחים. מצב זה מדכא את הפלקטואציות התרמיות ולכן מכבה את האינטרקציות המושרות על ידי תנודות הממברנה. אנו מוצאים כי התעבות קשרי האדהזיה בממברנות ללא אילוצים מתרחשת בטמפרטורה קריטית הקטנה פי 2-3 מזו של ממברנות שאינן חוות פלקטואציות, בהתאמה מעולה עם מסקנות ממודלים תיאורטיים קודמים. בניגוד לסימולציות המגבילות את תנודות הממברנה, סימולציות של ממברנות תחת מתח פנים שלילי, המגביר את תנודתיותן, מראות כי מתח הפנים השלילי כמעט שאינו משפיע על מעבר הפאזה. אולם, מתחת הטמפרטורה הקריטית מתח הפנים השלילי עלול להתבטא באי יציבות מכנית והופעתם של צבירי אדהזיה בעלי גיאומטריות מאורכות.

על מנת לחקור את המכניזם האנרגטי להתעבות קשרי אדהזיה, בו האינטרקציות המושרות על ידי האלסטיות של הממברנה יוצרות משיכה קצרת טווח על פני מרחק קורלציה אופייני של 50-100 ננומטרים, אנו מציגים תאוריית שדה ממוצע המבוססת על חישובים נומריים של אנרגית הממברנה כפונקציה של ריכוז קשרי אדהזיה. גישת השדה הממוצע מאפשרת גזירה של דיאגרמת הפאזות של המערכת מתוך ביטוי אמפירי לאנרגיה החופשית של המערכת. דיאגרמת הפאזות מראה כי בסמוך לנקודה הקריטית המעוותים הטיפוסיים של ממברנות עקב קשרי האדהזיה גורמים להפרדת פאזות במערכת, וליצירת פאזה דלילה למחיצה בה ריכוז קשרי האדהזיה הוא כ $100\mu m^{-2}$~. ריכוזים דומים נמצאים בסינפסה האימונולוגית, שבה קשרי TCR-pMHC מתקבצים במרכז הממשק בין תאי T לתאים מציגי אנטיגנים, בעוד שקשרי אדהזיה מסוג LFA1-ICAM1 מתגבשים סביבם. עבור הפרמטרים הביולוגיים של הסינפסה האימונולוגית, דיאגרמת הפאזות חוזה יצירת צבירים דלילים למחצה עם ריכוזים דומים לאלו הנמדדים בסינפסה.

על אף כי האנליזה שאנו מבצעים מדגישה את חשיבות אלסטיות הממברנה ליצירת הסינפסה האימונולוגית, התקבצותם של קשרי TCR-pMHC לכדי צביר במרכז הצומת הבין-תאי, דורשת מנגון שובר

סימטריה המכוון את התגבשותם של קשרים אלו למרכז המערכת. מנגנון שכזה מיוצר על ידי תהליכים אקטיביים של שלד התא הנובעים מזרימה רטרוגרדית של אקטין ופעילות חלבוני מנוע מסוג דינאין, המפעילים כוחות צנטריפטליים על קשרי ה TCR-pMHC. על מנת לחקור את תפקידן של תהליכים פאסיביים מול אקטיביים בהיווצרות הסינפסה האימונולוגית, אנו מציגים מודל שריג פשוט עם ייצוג בלתי מפורש של הממברנה, בו האינטרקציות המושרות על ידי אלסטיות הממברנה והתהליכים האקטיביים של שלד התא מיוצגים בעזרת פוטנציאלים פשוטים. תוצאות הסימולציות של מודל השריג מראות התאמה טובה מאוד עם הסממנים הבולטים המאפיינים את תהליך היווצרות הסינפסה. הסימולציות מראות כי תחילה נוצרים מיקרו-צבירים קטנים בפריפריה של המערכת, הגדלים עם הזמן, נעים לכיוון מרכז המערכת ומתגבשים ליצירת הצבר המרכזי בסינפסה. בנוסף, סקאלת הזמן להיווצרות הצביר המרכזי היא של כ 30 דקות, הדומה לזמן האופייני של היווצרות הסינפסה. התוצאות שופכות אור על הבקרה ההדדית בין תהליכים פאסיביים ואקטיביים בהיווצרות הסינפסה האימונולוגית, ומצביעות על תקפידה הקריטי של אלסטיות הממברנה בתהליך זה. אלסטיות הממברנה מעודדת יצירת מיקרו-צבירים בפריפריית המערכת, הנחוצים להפעלת אותות ביולוגיים לשפעולם של תאי ה- T. בנוסף, היא מאפשרת לאותות אלה לפעול לפרקי זמן של כמה עשרות בודדות של דקות לפני הגעתם של המיקרו-צבירים למרכז הסינפסה, שמדכא את יצירת האותות הללו.

מילות מפתח: אלסטיות של ממברנות, תנודות תרמיות, צמתי תאים, צבירי אדהזיה, מודל גז-שריג, מודלים מופשטים, סימולציות מונטה קרלו, מעברי פאזה, תיאוריית שדה ממוצע, סינפסה אימונולוגית, כוחות אקטיביים ופסיביים.

הצהרת תלמיד המחקר עם הגשת עבודת הדוקטור לשיפוט

אני החתום מטה מצהיר/ה בזאת: (אנא סמן):

___✓___ חיברתי את חיבורי בעצמי, להוציא עזרת ההדרכה שקיבלתי מאת מנחה/ים.

___✓___ החומר המדעי הנכלל בעבודה זו הינו פרי מחקרי מתקופת היותי תלמיד/ת מחקר.

_____ בעבודה נכלל חומר מחקרי שהוא פרי שיתוף עם אחרים, למעט עזרה טכנית הנהוגה בעבודה ניסיונית. לפי כך מצורפת בזאת הצהרה על תרומתי ותרומת שותפי למחקר, שאושרה על ידם ומוגשת בהסכמתם.

תאריך: 24 ביולי, 2017 שם התלמיד/ה: נדיב דהרן חתימה Nadiv Dharan

העבודה נעשתה בהדרכת פרופ׳ עודד פרגו
במחלקה להנדסה ביורפואית
בפקולטה להנדסה

התגבשות של אתרי אדהזיה בממברנות ביולוגיות וביו-מימטיות

מחקר לשם מילוי חלקי של הדרישות לקבלת תואר "דוקטור לפילוסופיה"

מאת

נדיב דהרן

הוגש לסינאט אוניברסיטת בן גוריון בנגב

אישור המנחה _____

אישור דיקן בית הספר ללימודי מחקר מתקדמים ע"ש קרייטמן _____

א' באב, תשע"ז **24 ביולי, 2017**

באר שבע

התגבשות של אתרי אדהזיה בממברנות ביולוגיות וביו-מימטיות

מחקר לשם מילוי חלקי של הדרישות לקבלת תואר "דוקטור לפילוסופיה"

מאת

נדיב דהרן

הוגש לסינאט אוניברסיטת בן גוריון בנגב

א' באב, תשע"ז **24 ביולי, 2017**

באר שבע